Topics in gravitational-wave physics

Thesis by

Geoffrey Lovelace

In Partial Fulfillment of the Requirements
for the Degree of
Doctor of Philosophy

California Institute of Technology
Pasadena, California

2007
(Defended May 14, 2007)

Acknowledgements

First, I would like to thank Kip Thorne, my advisor, for suggesting some of the problems investigated in this thesis, for many helpful discussions regarding both my research and other topics in relativity, for his assistance with some of the prose in Chapter 4, for helping me to improve my technical writing and presentations, and for introducing me to physics with his book *Black Holes and Time Warps: Einstein's Outrageous Legacy.* Without his advice, guidance, and encouragement, this work would not have been possible.

I would also like to thank Harald Pfeiffer for his advice and encouragement, for his patience in teaching me arcane details of the Caltech-Cornell numerical-relativity code, and for many productive discussions. I am also grateful to Lee Lindblom for his advice and encouragement, for many helpful discussions, and for suggesting the project described in Chapter 6. Mark Scheel and Larry Kidder have my thanks for helpful discussions and technical assistance with the Caltech-Cornell numerical-relativity code.

I would like to thank Duncan Brown, Hua Fang, and Chao Li, for collaborating with me and for many useful discussions. Rob Owen has my thanks for many useful discussions regarding my research and for introducing me to some formal, mathematical aspects of relativity.

Sterl Phinney and Kenneth Libbrecht have my thanks for serving on my thesis committee.

I would also like to thank Juri Agresti for helpful discussions as well as for providing the data that will be published in J. Agresti and R. DeSalvo (2007, currently in preparation), for the comparison in Sec. 2.4.2. I am grateful to Greg Cook for helpful discussions, including the initial suggestion to add radial motion to quasi-circular initial data (Chapter 5). I would also like to acknowledge Ilya Mandel for useful discussions as well as for suggesting the comparison to Peters' calculation [P. C. Peters, Phys. Rev. **136**, B1224 – B1232 (1964)], which was helpful in the investigation reported in Chapter 5.

I am grateful to Mike Boyle, Jeandrew Brink, Yanbei Chen, Michael Cohen, Steve Drasco, Jonathan Gair, Keith Matthews, Yasushi Mino, Niall O'Murchadha, Yi Pan, Sherry Suyu, Etienne Racine, and everyone who attended Kip and Lee's group meetings, for helpful discussions.

JoAnn Boyd, Jennifer Formichelli, and Shirley Hampton have my thanks for help with administrative matters.

The research presented in this thesis was supported in part by NASA grants NAG5-12834, NAG5-10707, NNG04GK98G, NNG05GG52G, NNG05GG51G; by NSF grants PNY-0099568, PHY-0601459, PHY-0244906, DMS-0553302, PHY-0312072, PHY-0354631; by the Sherman Fairchild Foundation, and by the Brinson Foundation.

Some of the simulations discussed in Chapters 5 and 6 were produced with LIGO Laboratory computing facilities. LIGO was constructed by the California Institute of Technology and Massachusetts Institute of Technology with funding from the National Science Foundation and operates under cooperative agreement PHY-0107417.

Mathematica and Maple for Mac OS X were used to verify some of the equations in this thesis. Some of the figures were prepared using Grace 5. Some of the simulations in this thesis were run on the Shared Heterogeneous Cluster at Caltech. Some of the simulations described in this thesis were run on a Mac Pro workstation. The LaTeX style file used in this thesis was developed by Daniel M. Zimmerman.

Finally, I would like to thank my parents, Robert and Diane, my brother Jason, and my sister-in-law Margaret for their encouragement and support, without which this work would not have been possible.

Abstract

Together with ongoing experimental efforts to detect gravitational waves, several fronts of theoretical research are presently being pursued, including second-generation detector design, data analysis, and numerical-relativity simulations of sources. This thesis presents a study in each of these topics: i) The noise in the most sensitive frequency bands in second-generation ground-based gravitational-wave interferometers is dominated by the thermal noise of the test masses. One way to reduce test-mass thermal noise is to modify shape of the laser beam so that it better averages over the thermal fluctuations. When edge effects are neglected, the test-mass thermal noise is related to the beam shape by simple scaling laws. This thesis presents a rigorous derivation of these laws, along with estimates of the errors made by neglecting edge effects. ii) An important class of gravitational-wave sources for space-based gravitational-wave interferometers is extreme-mass-ratio inspirals (EMRIs). These are binaries in which an object of a few solar masses spirals into a (typically million-solar-mass) supermassive black hole (or, if any exist, other type of massive body). Ryan (1995) proved that, under certain simplifying assumptions, the spacetime geometry is redundantly encoded in EMRI waves. One of Ryan's assumptions was negligible tidal coupling. After first finding that only the time-varying part of the induced tide is unambiguously defined when the central body is a black hole, this thesis extends Ryan's theorem by showing that both the spacetime geometry and details of the tidal coupling are encoded in EMRI waves. iii) Merging black holes with comparable masses are important sources of gravitational waves for ground-based detectors. The gravitational waves near the time of merger can only be predicted by numerically solving the Einstein equations. Initial data in numerical simulations must contain the desired physical content but also satisfy the Einstein constraint equations. But conventional binary-black-hole initial data has physical flaws: a nonzero orbital eccentricity and an initial, unphysical pulse of spurious gravitational radiation. Using the Caltech-Cornell pseudospectral code, this thesis develops and implements methods to reduce both of these effects.

Contents

List of Figures

List of Tables

Chapter 1

Introduction

The direct measurement of gravitational waves promises to give us an unprecedented tool for observing the universe. Gravitational waves can be used to directly probe systems in which gravity is very strong and (consequently) the spacetime geometry is strongly warped. These systems include both the calm (e.g., a steller-mass object spiraling into a supermassive black hole) and the most violent (e.g., two black holes colliding, releasing a significant fraction of their mass as gravitational waves). Some systems (like colliding black holes) emit tremendous amounts of energy as gravitational waves without any electromagnetic signature.

Over the past three decades, a great experimental effort has worked toward the goal of using gravitational waves to probe experimentally such strongly-gravitating systems. Ground-based detectors including LIGO [1], VIRGO [2], GEO600 [3, 4], and TAMA300 [5], are presently searching for high-frequency ($\sim 10 - 10^4$ Hz) gravitational-wave signals; in particular, LIGO is nearing the completion of a year-long science run at its design sensitivity [6]. A planned upgrade of LIGO ("advanced LIGO"), for which funding will begin in 2008 [7], will increase the event rate by a factor of 10^3. In the next decade, the Laser Interferometer Space Antenna (LISA) [8] will detect low-frequency ($\sim 10^{-4} - 0.1$ Hz) gravitational waves.

In parallel with the experimental program, theoretical investigations are being pursued on several fronts, including i) maximizing the sensitivity of next-generation gravitational wave detectors, ii) recovering the physical information that is encoded in astrophysical gravitational-wave signals, and iii) using numerical relativity to simulate highly nonlinear sources, such as the gravitational-waveforms emitted by colliding black holes. In this thesis, I describe investigations in each of these three topics:

- **Reducing test-mass thermal noise in advanced gravitational-wave detectors.** In advanced LIGO's most sensitive frequency band ($\sim 40 - 200$ Hz), the sensitivity is limited primarily by *test-mass thermal noise* (e.g., Fig. 2 of [9]). The test-mass thermal noise is manifested by random fluctuations of the shape of the mirror face. One way to reduce this noise is by changing the laser-beam shape so that it better averages over these fluctuations. In Sec. 1.1 and in Chapter 2, I discuss and derive simple scaling laws that determine how the test-mass thermal noise depends on the beam shape when edge effects are neglected.

- **Probing tidal coupling using gravitational waves.** A primary objective of LISA is to probe, with high accuracy, supermassive black holes (and, should any exist, other kinds of massive central bodies) using gravitational waves from smaller inspiraling objects (such as neutron stars and small-mass black holes). [Such gravitational-wave sources are called "extreme-mass-ratio inspirals" (EMRIs).] Specifically, LISA will measure i) the central body's spacetime geometry (metric), ii) the details of the small object's orbit, and iii) the tidal coupling between the small object and the central body. Recovering this information in practice is one of LISA's data-analysis challenges; this goal was motivated in part by Ryan [10], who proved, under several simplifying assumptions, that the full details of the central body's spacetime geometry are encoded in the EMRI waves. One of Ryan's assumptions was that *tidal coupling* is negligible; in this thesis, I consider how to lift this restriction. First, in Sec. 1.2.2 and Chapter 3 I consider how to describe tidal coupling when the central object is a black hole. Then, in Sec. 1.2.3 and Chapter 4 I extend Ryan's analysis to include tidal coupling.

- **Reducing eccentricity and junk radiation in binary-black-hole simulations.** Gravitational-wave detectors such as LIGO and LISA need accurate predictions of the gravitational waves they are likely to see. These predicted waveforms will serve as templates in the LIGO and LISA data analyses. One of the most important sources of gravitational waves for LIGO is the inspiral, merger, and ringdown of two binary black holes of comparable mass. The gravitational waves before and after the merger can be computed using perturbative methods; however, near the time of the merger, the spacetime is so strongly and dynamically warped that the waveforms can only be predicted by numerically solving the Einstein equations. Numerical simulations of binary black holes begin with the choice of initial data. In this thesis, I will discuss how, with improved choices for the initial data, binary-black-hole simulations can be made more physically realistic in two ways. In Sec. 1.3.2 and Chapter 5 I describe how to reduce the *orbital eccentricity.* Then, in Sec. 1.3.3 and Chapter 6 I describe how to reduce the amount of *junk radiation* (i.e., spurious gravitational waves) present at early times in binary-black-hole simulations.

The remainder of this introductory chapter summarizes the investigations listed above. Further details are given in subsequent chapters.

1.1 Reducing thermal noise in advanced gravitational-wave interferometers

A gravitational-wave interferometer such as advanced LIGO measures two perpendicular arms' difference in length. At each end of each arm is a test mass (i.e., a mirror). If mirrors 1 and 2 are in one arm, and mirrors 3 and 4 are in the other, then the interferometer measures

$$h \equiv [(q_1 - q_2) - (q_3 - q_4)]/L, \tag{1.1}$$

where $q_{1,2,3,4}$ are the positions of the four test masses and L is the length of each arm. Ideally, $h = 0$ in the absence of a gravitational wave. When a wave passes through the detector, the lengths of the two arms change, giving a nonzero $h(t)$ as a function of time t.

The actual measurement of h includes both the gravitational-wave signal and noise. Reducing the noise power (i.e, the spectral density, defined below) by a factor of n^2 is equivalent to increasing the maximum range of the interferometer by a factor of n. The total volume of space seen by the interferometer (and thus the event rate of the detector) then increases by a factor of n^3.

For frequencies $f \sim 40 - 200$ Hz (where advanced LIGO is most sensitive), the noise is dominated by thermal fluctuations in the test-mass substrates and coatings. There are two types of these fluctuations: *Brownian* (in which thermally excited normal modes are coupled via imperfections in the substrate and coating), and *thermoelastic* (in which random heat flow causes temperature fluctuations, producing random thermal expansion and contraction). To maximize the event rate in the $f \sim 40 - 200$ Hz band, one must minimize each type of thermal noise.

These thermal fluctuations in substrate and coating lead to fluctuations $Z(t; r, \varphi)$ in the position of each point (r, φ) on the coating face. The laser beam averages over these fluctuations. The average is weighted by the shape p of the laser beam's power distribution. If the beam is axisymmetric, so $p = p(r)$, then the laser beam measures

$$q(t) \equiv \int drr \int d\varphi Z(t; r, \varphi) p(r), \tag{1.2}$$

where $p(r)$ is normalized so $2\pi \int drrp^2(r) = 1$.

The wider and flatter the beam shape $p(r)$, the better the beam averages over the fluctuating mirror surface and the lower the resulting thermal noise. However, the light power must be small enough near the mirror edges that no more than $\sim$ 10ppm is lost to diffraction per bounce. To balance these two requirements, mesa beams [11, 12, 13] have been proposed as an alternative to gaussian beams. For the same diffraction losses, the mesa beams are flatter and thus better average over the mirror fluctuations. Other beam shapes are also being explored [14].

Because changes to the laser beam shape can significantly affect the detector's sensitivity, it is important to understand deeply the relationship between the beam shape and the thermal noise. To that end, O'Shaughnessy, Vyatchanin, and Vinet [13, 15, 16, 17] have proposed (with varying degrees of rigor, and sometimes with unnecessary assumptions) simple scaling laws relating the beam shape to the thermal noise when the beam is small compared to the mirror ("negligible edge effects"). The scaling laws are

$$\frac{S_{1,n}}{S_{2,n}} = \frac{\int_0^\infty \mathrm{d}k k^n \left[\tilde{p}_1(k)\right]^2}{\int_0^\infty \mathrm{d}k k^n \left[\tilde{p}_2(k)\right]^2} \tag{1.3}$$

where $n = 1$ for coating Brownian and coating thermoelastic noise, $n = 0$ for substrate Brownian noise, and $n = 2$ for substrate thermoelastic noise. Here $\tilde{p}(k)$ is the Hankel transform of the beam shape $p(r)$, or equivalently its two-dimensional Fourier transform

$$\begin{aligned} \tilde{p}(k) &= \int_0^\infty \mathrm{d}r r J_0(kr) p(r), \\ p(r) &= \int_0^\infty \mathrm{d}k k J_0(kr) \tilde{p}(k), \end{aligned} \tag{1.4}$$

where $J_0(x)$ is the 0^{th} Bessel function of the first kind. If the noise S_2 for beam shape 2 is known, then it is easy to use Eq. (1.3) to compute the noise S_1 if the beam shape were changed to $p_1(r)$ while holding everything else constant, provided that edge effects can be neglected.

In Chapter 2, I present a rigorous derivation of these scaling laws and critique the prior derivations. My derivation is based on a variant of the fluctuation-dissipation theorem [18] that relates the fluctuations (characterized by the spectral density) to the dissipated power W_{diss} if a sinusoidal pressure, with the same distribution $p(r)$ as the laser beam's intensity distribution, were applied to the mirror. The fluctuation-dissipation theorem is

$$S_q(f) = \frac{2k_B T}{\pi^2 f^2} \frac{W_{\text{diss}}(f)}{F^2}. \tag{1.5}$$

Here f is the frequency, F is the amplitude of the imagined applied pressure, and W_{diss} is proportional to F^2, so that S_q is independent of F. Each of the four types of thermal noise leads to a dissipated power and a corresponding thermal noise.

Also in Chapter 2, using recent results by Agresti [19, 20] that include edge effects for the specific case of mesa beams, I estimate the scaling laws' errors due to neglecting edge effects.

I have submitted Chapter 2 to Classical and Quantum Gravity; I am the sole author.

1.2 Probing tidal coupling with gravitational waves

1.2.1 Background

One of the scientific goals of the LISA mission is to use EMRI gravitational waves to measure the tidal response of the massive central black hole (or, perhaps, other massive body). Finn and Thorne [21] have shown that tidal coupling can influence the phase of the inspiral gravitational waves by as much as a few percent. LISA will be able to measure the EMRI-wave phase to an accuracy of a fraction of a cycle out of $\sim 10^4 - 10^5$ cycles; this motivates the possibility of using the EMRI waves that LISA detects to probe tidal coupling with high precision.

In order to use EMRI waves to probe massive central bodies in this way, there must be an algorithm to recover the physical parameters of the EMRI—including the central body's spacetime geometry, the details of the small object's orbit, and the tidal coupling—from the emitted waves. In practice, this may be quite difficult.

As a first step toward demonstrating the feasibility of recovering EMRI parameters from the waves, Fintan Ryan [10] proved that *in principle* the central body's spacetime geometry (i.e., its multipole moments) can be extracted from the EMRI waves, provided that the following assumptions hold:

1. The massive central body's exterior is a vacuum, stationary, axisymmetric, reflection-symmetric, and asymptotically flat (SARSAF) solution of Einstein's equations.
2. The small object travels on a nearly circular, nearly equatorial orbit, with fundamental frequencies Ω_ρ, Ω_z, and Ω_ϕ. (The primary component of the waves has frequency $f = \Omega_\phi/\pi$; Ω_ρ and Ω_z show up in the orbit's precession and in the waves' precessional sidebands.)
3. Tidal coupling is negligible.

Additionally, Ryan proved that the multipole moments are encoded redundantly both in the "precession frequencies" Ω_ρ and Ω_z and in the waves' phase evolution

$$\Delta N(f) \equiv \frac{f^2}{df/dt}. \tag{1.6}$$

(Here $f = \Omega_\phi/\pi$.)

Several studies have sought to generalize Ryan's theorem to more realistic situations by lifting some of these restrictions. Assumption 1 has been extended to electrovacuum spacetimes by Sotiriou and Apostolatos [22]. Assumption 2 of nearly circular, nearly equatorial orbits is relaxed in a paper by Li [23]. In this thesis, I consider how to define tidal coupling when the central body may be a black hole (Chapter 3); then, I relax Assumption 3 by generalizing Ryan's theorem to include tidal coupling (Chapter 4).

1.2.2 Defining tidal coupling

In Chapter 3, I consider how best to *define* tidal coupling when the central body may a black hole. Black-hole tidal coupling has previously been defined in terms of the flux of gravitational waves down the hole (e.g., [24]) and in terms of the perturbation of the horizon's intrinsic metric (e.g. [25, 26]). Both definitions depend on the central body being a black hole.

Thorne [27] has argued that, in defining tidal coupling, one should allow for the possibility that the central body is some other kind of object [such as a boson star (e.g. [28, 29]), soliton star (e.g. [30]), or naked singularity]. Specifically, Thorne proposed that for all types of central bodies, the tides be defined by analogy with Newtonian tides:

When a Newtonian fluid planet is perturbed by a small, orbiting moon, a quadrupole moment is induced on the central body. The induced quadrupole moment $\mathscr{I}_{ij}$ is manifested both in the change of the planet's shape and in the induced tidal field acting back on the moon to change its orbit. This induced quadrupole moment can be characterized by two scalars:

1. *Polarizability.* The induced quadrupole moment $\mathscr{I}_{ij}$ is proportional to the moon's tidal field $\mathscr{E}_{ij}$:

   $$\mathscr{I}_{ij} = PL^5\mathscr{E}_{ij}. \tag{1.7}$$

   Here L is the characteristic size of the central body and P is a number of order unity called the body's *polarizability.* The polarizability characterizes the strength of the tidal perturbation that the central body exerts back on the moon.

2. *Phase shift.* Because of viscous dissipation as the fluid planet's shape changes in its own rest frame, there is a torque back on the moon, so that energy and angular momentum are transferred between the moon and the central body. In the case of a stationary moon outside a slowly rotating planet, the lag angle is (Eqs. (3.8) and (3.12) of [26])

   $$\delta = \frac{19}{2}\frac{\Omega\nu}{gL}, \tag{1.8}$$

   where g is the acceleration of gravity, Ω is the angular velocity of the planet, and ν is the fluid's kinematic viscosity.

In Chapter 3, in collaboration with Hua Fang, I investigate Thorne's proposal for the case of a central black hole. When a small object orbits a nonrotating black hole, we find that the only gauge-invariant portion of the induced quadrupole moment (defined in terms of the induced tidal field acting back on the moon) is

$$\mathscr{I}^{\text{ind}}_{ij} = \frac{32}{45}M^6\frac{d}{dt}\mathcal{E}^{\text{ext}}_{ij}. \tag{1.9}$$

where M is the black hole's mass and $\mathcal{E}^{\text{ext}}_{ij}$ is the moon's perturbing tidal field. This induced quadrupole moment is proportional not to the perturbing tidal field but to its time derivative. The part proportional to $\mathcal{E}_{ij}^{\text{ext}}$ itself turns out to be ambiguous; in the particular coordinates that Fang and I used in deriving Eq. (1.9), it vanishes. The unambiguous part (1.9), proportional to $\frac{d}{dt}\mathcal{E}_{ij}^{\text{ext}}$, produces a torque back on the moon that changes its orbital energy by an amount equal and opposite to the rate that energy flows into the black hole:

$$\frac{dE_{\text{moon}}}{dt} = -\frac{dE_H}{dt} - \frac{32}{5}M^4\mu^2\Omega^6, \tag{1.10}$$

Here μ and Ω are the mass and orbital angular velocity of the moon, respectively. This agrees with the result previously derived (using the "waves down the hole" picture) by Poisson [31].

Our analysis shows that the lag angle δ and polarizability P of the black hole, as defined in terms of the induced quadrupole moment, are ambiguous. However, there is an *unambiguous* lag angle (i.e., "phase shift") defined in terms of the orientation of the horizon's tidal bulge (relative to the moon's angular location). Hartle [26] has computed this tidal phase shift on the horizon when a stationary moon orbits a spinning hole. In terms of the hole's mass M, horizon angular velocity Ω_H, and moon radius $b \gg M$, he finds (after a sign error in his analysis is corrected):

$$\delta = -\frac{8}{3}M\Omega_H - 4\frac{M^2\Omega_H}{b}. \tag{1.11}$$

The phase shift is negative, meaning that the tidal bulge *leads*, rather than lags, the perturbing tidal field. Hartle attributes this difference to the teleological nature of the horizon [26]: a fluid planet's evolution is computed from initial conditions, while the horizon evolves backward from a final condition (giving a phase lead, not a phase lag).

When a nonspinning hole (with mass M) is orbited by a stationary moon (with angular velocity Ω, at a radius $b \gg M$), the situation considered in Chapter 3, Fang and I find the analog of Hartle's phase shift:

$$\delta = -\frac{8}{3}M\Omega - \Omega[b + 2M\log(b/2M - 1)]. \tag{1.12}$$

The phase shift is still a phase lead, but the second term is different from Hartle's.

The terms depending on b in Eqs. (1.11) and (1.12) are consequences of the way Hartle defines the angle between the bulge on the horizon and the moon.

In Chapter 3, Hua Fang and I each performed all of the calculations independently of each other, except for the generalization of Hartle's phase shift (which was solely my work); we jointly wrote the prose. We have published Chapter 3 in Physical Review D.

1.2.3 Extending Ryan's theorem to include tidal coupling

In Chapter 3, Fang and I find that only the time-dependent part of the induced quadrupole moment is unambiguous. Motivated by this result, in Chapter 4, (in collaboration with Chao Li) I define tidal coupling by $dE_{\rm body}/dt$, the energy absorption of the central body. (Because the orbit is nearly circular, the corresponding angular-momentum absorption is simply $dL_{\rm body}/dt = \Omega_{\rm orbit} dE_{\rm body}/dt$, where $\Omega_{\rm orbit}$ is the small object's orbital angular velocity.)

Using this definition, we extend Ryan's analysis to include tidal coupling. In our analysis, we retain Ryan's other two assumptions [passage preceding Eq. (1.6)]. The inclusion of tidal coupling breaks the redundancy in his theorem.

In Ryan's analysis, as in the analysis of Chapter 4, the small mass is presumed to be sufficiently distant that the adiabatic approximation is valid [10]. That is to say, the moon inspirals on a time scale much greater than an orbital period. The frequencies $\Omega_\phi = \pi f$, Ω_ρ, and Ω_z slowly evolve as the orbit loses energy and angular momentum to gravitational waves and the particle spirals inward. On the time scale of an orbit, the particle essentially follows a single geodesic (when the tiny, conservative self-force is neglected, as it can be in the limit $\mu/M \to 0$).

In Ryan's original theorem, the spacetime geometry can be recovered independently from either of the precession frequencies Ω_ρ and Ω_z. Since these frequencies are related only to the geodesic motion of the small mass, and not to its slow, secular evolution, the precession frequencies are *independent of tidal coupling*. Therefore, the spacetime geometry, via its multipole moments, can be recovered from $\Omega_\rho(f)$ and $\Omega_z(f)$ using Ryan's argument without modification. Additionally, with knowledge of the spacetime geometry in hand, we show that the orbital parameters can, in principle, be deduced from the amplitudes of the waves' precession-induced modulations.

The tidal coupling information is then contained in the waves' phase evolution $\Delta N(f) \equiv \frac{f^2}{df/dt}$. The total energy loss of the orbit is related to ΔN by

$$\dot{E}_{\rm total} = -\dot{E}_{\rm orbit} = -\frac{dE_{\rm orbit}}{df}\frac{df}{dt} = -f^2 \frac{dE_{\rm orbit}}{df}\frac{1}{\Delta N}. \tag{1.13}$$

Here $\frac{dE_{\rm orbit}}{df}$ depends only on the geodesic motion (not on tidal coupling), ΔN is the measured phase evolution, and dots represent time derivatives. In the absence of any influence of the central body, the phase evolution would have a different value $\Delta N_{\rm NBI}$ (obtainable in principle, as Ryan showed [10], from the spacetime geometry). Here "NBI" means "no body influence." Therefore,

$$\dot{E}_{\rm total,NBI} = -f^2 \frac{dE_{\rm orbit}}{df}\frac{1}{\Delta N_{\rm NBI}} \tag{1.14}$$

is also observable. The difference

$$\dot{E}_{\mathrm{total,BI}} = \dot{E}_{\mathrm{total}} - \dot{E}_{\mathrm{total,NBI}} = \dot{E}_{\mathrm{body}} + \dot{E}_{\infty\mathrm{BI}}, \tag{1.15}$$

is the influence of the body on the rate of energy loss from the orbit. By energy conservation it consists of two parts: $\dot{E}_{\mathrm{body}}$ is the energy absorption of the central body, and $\dot{E}_{\infty\mathrm{BI}}$ is a small influence in the rate of energy flux to infinity due to the details of the central body's influence. Both quantities are very small; contrary to a conjecture by Thorne, we see no way in general to deduce the central body's absorption by itself. However, in the case that the central body is very compact, we argue that it is likely that $\dot{E}_{\infty\mathrm{BI}}/\dot{E}_{\mathrm{body}} \sim O(v^5)$, where v is the (small) velocity of the orbiting particle. The relative smallness of $\dot{E}_{\infty\mathrm{BI}}$ comes from the difficulty gravitational waves have in penetrating the "effective potential" of the compact central body's metric. Perturbations being absorbed by the central body must cross the potential once, while perturbations carrying $\dot{E}_{\infty\mathrm{BI}}$ must cross the potential twice (once to come in contact with the central body, and a second time to escape back to infinity).

Chao Li and I performed all of the calculations in Chapter 4 independently, except for the Appendix, which is primarily Chao's work. The text of this chapter is largely mine, but with significant contributions from Li and from Thorne. Li and I have submitted it to Physical Review D.

1.3 Improving binary-black-hole initial data

1.3.1 Background

In numerical simulations of binary black holes, one divides the four-dimensional spacetime (with metric $g_{\mu\nu}$) into a series of three-dimensional spatial slices (with spatial metric g_{ij}). The spacetime and spatial metrics are related by

$$ds^2 = g_{\mu\nu}dx^\mu dx^\nu = -\alpha^2 dt^2 + g_{ij}(dx^i + \beta^i dt)(dx^j + \beta^j dt). \tag{1.16}$$

Here the lapse α and the shift β^i specify how the coordinates change from slice to slice.

Choosing initial data amounts to choosing the metric g_{ij} and the extrinsic curvature K_{ij} of the initial spatial slice. The extrinsic curvature is essentially the derivative of g_{ij} normal to the spatial slice; it is related to the coordinate time derivative of the metric $\partial_t g_{ij}$ by

$$\partial_t g_{ij} = -2\alpha K_{ij} + 2\nabla_{(i}\beta_{j)}, \tag{1.17}$$

where ∇ is the covariant derivative in the slice.

The tensors g_{ij} and K_{ij} must be chosen in accord with the desired physical content of the simulation (here, a spacetime with two inspiraling black holes). However, g_{ij} and K_{ij} cannot be chosen freely; together, they must ensure that the (vacuum) Einstein constraint equations are satisfied:

$$\begin{aligned} G_{00} &= 0, \\ G_{0j} &= 0. \end{aligned} \tag{1.18}$$

(This requirement is analogous to the restriction that, when solving Maxwell's equations in vacuum, the electric and magnetic field are initially divergence free.) The remaining Einstein equations, $G_{ij} = 0$, determine the solution on subsequent slices, given constraint-satisfying initial data, and if the constraints (1.18) are satisfied perfectly in the initial data, then the evolution equations $G_{ij} = 0$ will preserve them.

Several methods (e.g. [32, 33]) for generating constraint-satisfying initial data are known. However, the constraint-satisfying initial data that they generate can have undesirable, unphysical properties all too easily. In this thesis, I reduce two such effects for equal-mass, nonspinning black hole binaries: orbital eccentricity and junk radiation.

1.3.2 Reducing eccentricity in binary-black-hole simulations

As two black holes in a binary orbit each other, they spiral together and emit gravitational waves. During the inspiral, the holes' orbits tend to circularize (faster than the holes inspiral) due to the emission of gravitational waves [34]. (Qualitatively, this circularization happens because, on an eccentric orbit, the holes radiate more power when they are closer together and less when they are farther apart.)

To construct black holes on nearly circular orbits, my colleagues and I use *quasicircular* initial data (e.g. [32]). In quasicircular data, the separation of the holes is initially constant in time; however, this condition does not lead to noneccentric orbits. This is because quasicircular data ignore the inspiraling motion of the holes.

If the initial data are constructed in coordinates that move with the black holes ("comoving coordinates"), then the motion of the holes is captured by the asymptotic behavior of the coordinates. In the asymptotically flat region, $g_{ij} = \delta_{ij}$ and $\alpha = 1$, and the spacetime metric is then

$$ds^2 = g_{\mu\nu}dx^\mu dx^\nu = -dt^2 + \delta_{ij}(dx^i + \beta^i dt)(dx^j + \beta^j dt). \tag{1.19}$$

If the black holes are at rest, the comoving coordinates are asymptotically inertial, which implies that $\beta^i(r \to \infty) = 0$ in Eq. (1.19).

On the other hand, if the black holes are moving, the comoving coordinates have nonvanishing shift. Quasicircular data in particular require that the comoving coordinates be asymptotically a pure rotation:

$$\beta^i(r \to \infty) = (\mathbf{\Omega} \times \mathbf{r})^i. \tag{1.20}$$

This is a "pure rotation" in the sense that the gradient of the shift $\nabla_i \beta_j$ is purely antisymmetric.

Physically, the holes should also be slowly spiraling together. By requiring that the holes' inward velocity be initially zero, quasicircular data ensure that the holes are initially at a turning point of an eccentric orbit. To construct a non-eccentric orbit, the comoving coordinates must asymptotically contract as well as rotate:

$$\beta^i(r \to \infty) = (\mathbf{\Omega} \times \mathbf{r})^i + \frac{v_r}{r} r^i. \tag{1.21}$$

where $v_r < 0$. The second term is a "pure expansion" in the sense that its gradient is a pure trace.

The appropriate choices for Ω and v_r, at the modest hole separations $s \simeq 2r \sim 15M$ (with M the total mass of the binary), are found by the following iterative scheme:

1. Start with the quasicircular guess for Ω and with $v_r = 0$. Solve for the initial data and evolve it.

2. Plot ds/dt, the rate of change of the proper distance between the holes' apparent horizons, as a function of time t. Find the best fit of ds/dt having the form

   $$\frac{ds}{dt} = A_0 + A_1 t + B \sin(\omega t + \varphi). \tag{1.22}$$

3. If the binaries were Newtonian point particles, the following changes to Ω and v_r would remove the eccentricity:

   $$\Omega^N = \Omega - \frac{B\omega}{2s(t=0)\Omega} \cos\varphi, \tag{1.23}$$

   $$v_r^N = v_r - \frac{B}{2} \sin\varphi. \tag{1.24}$$

   Here the superscript "N" stands for "Newtonian."

4. In the relativistic case, these changes will *not* remove the eccentricity completely. Instead, use Ω^N and v_r^N as an initial guess, and go back to step 1.

Each iteration will reduce the orbital eccentricity.

In Chapter 5 I describe this argument and implement it using the Caltech and Cornell pseudospectral code [35, 36, 37]. In this work, I collaborated with Harald Pfeiffer, Duncan Brown, Lawrence Kidder, Lee Lindblom, and Mark Scheel. My contribution to this work was limited to the following:

- I independently arrived at Eq. (1.21), using the argument presented in this introduction. An alternative derivation by Pfeiffer is presented in Chapter 5.
- I developed the code that, using the spectral elliptic solver developed by Pfeiffer [35], solves the constraint equations (1.18) using the extended conformal thin sandwich (e.g. [38]) method with (aside from modifications described above) the quasiequilibrium boundary conditions suggested by Cook and Pfeiffer [32].
- I solved the constraint equations for several quasicircular and noneccentric initial data sets.
- I checked Pfeiffer's derivation of the iterative scheme described in this introduction. Although I did not carry out the scheme myself for the results described in Chapter 5, I did use the method to reduce eccentricity in other initial data, such as that presented in Chapter 6.
- I made some minor contributions to the prose of Secs. 5.2 and 5.7.

My coauthors and I have submitted this chapter to Classical and Quantum Gravity, and it has been accepted for publication.

1.3.3 Reducing junk radiation in binary-black-hole simulations

Current simulations of binary-black-hole spacetimes contain, in addition to the black holes, an initial pulse of spurious, unphysical gravitational waves (e.g., Sec. 3.2 of [39]) that we refer to as "junk radiation."

This "junk" is a consequence of the way the initial data are constructed. The constraints (1.18) are typically solved by a conformal decomposition [40, 41] of the initial spatial metric:

$$g_{ij} = \psi^4 \tilde{g}_{ij}. \tag{1.25}$$

The conformal metric $\tilde{g}_{ij}$ is freely specified; ψ is determined by solving the constraint equations. Binary black hole initial data are usually taken to be conformally flat:

$$g_{ij} = \psi^4 \delta_{ij}. \tag{1.26}$$

However, it is known that isolated black holes in equilibrium do not admit conformally-flat spatial slices if the hole has linear [42] or angular [43] momentum; the holes in a binary, in general, have both. Consequently, the simplifying demand for conformal flatness leads to initial data in which the black holes are initially *not* in equilibrium; instead, they are unphysically perturbed. During the evolution, the holes vibrate, quickly relaxing to an equilibrium configuration, but as they do, gravitational waves are emitted.

These spurious gravitational waves (called "junk radiation") are unphysical (since there is no physical mechanism behind the holes' initial excitation), and they are computationally expensive. Before extracting the physically-meaningful gravitational waves from a binary black hole evolution, the simulation must run until the spurious gravitational waves have left the computational domain. Moreover, the spurious waves have fine structure that necessitates higher resolution than would otherwise be needed. Therefore, it is optimal to reduce this junk radiation as much as possible, even when the holes initially are nonspinning and move at a small ($v \sim 0.1$) velocity.

One way of reducing the junk radiation is to choose a conformal metric that superposes two boosted binary black holes:

$$\tilde{g}_{ij} = \tilde{g}_{ij}^{\mathrm{SBS}} \equiv \delta_{ij} + e^{-r_A^2/w^2}\left(g_{ij}^A - \delta_{ij}\right) + e^{-r_B^2/w^2}\left(g_{ij}^B - \delta_{ij}\right). \tag{1.27}$$

Here "SBS" stands for "superposed-boosted-Schwarzchild," and g_{ij}^A and g_{ij}^B are metrics of boosted Schwarzschild black holes centered at positions $\mathbf{r}^A$ and $\mathbf{r}^B$, respectively. The Gaussians force the metric to be conformally flat far from the holes, which ensures that g_{ij} is consistent with asymptotic flatness (i.e., that $\tilde{g}_{ij}$ is asymptotically flat and that $\psi(r \to \infty) = 1$).

In Chapter 6, I construct initial data using Eq. (1.27) for the conformal metric. Otherwise, the initial data scheme is the same as that described in Chapter 5 (and summarized in the previous subsection). Then, I evolve the SBS data (again using the Caltech-Cornell pseudospectral code [35]). I compare the SBS and conformally-flat junk waves, and find them to be smaller in the SBS case by a factor of approximately two in amplitude (four in power). This is a significant improvement. Chapter 6 is solely my own, though the research described there was carried out under the guidance of H. Pfeiffer and L. Lindblom. Some variant of it will be part of a future publication.

1.4 Bibliography

[1] A. Abramovici et al., Science **256**, 325 (1992).

[2] B. Caron et al., Class. Quantum Grav. **14**, 1461 (1997).

[3] H. Lück et al., Class. Quantum Grav. **14**, 1471 (1997).

[4] B. Willke et al., Class. Quantum Grav. **19**, 1377 (2002).

[5] M. Ando et al., Phys. Rev. Lett. **86**, 3950 (2001).

[6] A. Lazzarini, Tech. Rep., LIGO scientific collaboration (internal LIGO document) (2007), URL `http://www.ligo.caltech.edu/docs/G/G070036-00/`.

[7] Advanced LIGO: context and summary (online document accessed 28 April, 2006), URL `http://www.ligo.caltech.edu/advLIGO/scripts/summary.shtml`.

[8] T. Prince and K. Danzmann, Tech. Rep., LISA International Science Team (2007), URL `http://www.rssd.esa.int/SYS/docs/ll_transfers/LISA_Science_Requirements.pdf`.

[9] Advanced LIGO: context and summary (online document accessed 28 April, 2007), URL `http://www.ligo.caltech.edu/advLIGO/scripts/ref_des.shtml`.

[10] F. D. Ryan, Phys. Rev. D **52**, 5707 (1995).

[11] E. d'Ambrosio, R. O'Shaughnessy, and K. S. Thorne, Beam reshaping to reduce thermal noise (internal LIGO document G000223-00-D) (2000), URL `http://www.ligo.caltech.edu/docs/G/G000223-00.pdf`.

[12] E. D'Ambrosio et al., Phys. Rev. D. (submitted), (2004), `gr-qc/0409075`.

[13] R. O'Shaughnessy, S. Strigin, and S. Vyatchanin, Phys. Rev. D (submitted), (2003), `gr-qc/0409050`.

[14] M. Bondarescu and Y. Chen, (in preparation).

[15] R. O'Shaughnessy, Class. Quantum Grav. **23**, 7627 (2006).

[16] S. Vyatchanin, FDT approach calculations of Brownian noise in thin layer (internal LIGO document T040242-00Z) (2004), URL `http://www.ligo.caltech.edu/docs/T/T040242-00.pdf`.

[17] J.-Y. Vinet, Class. Quantum Grav. **22**, 1395 (2005).

[18] Y. Levin, Phys Rev. D **57**, 659 (1997).

[19] J. Agresti and R. DeSalvo, flat beam profile to depress thermal noise (internal LIGO document G050041-00-Z) (2005), URL `http://www.ligo.caltech.edu/docs/G/G050041-00`.

[20] J. Agresti and R. DeSalvo (2007), (document in preparation).

[21] L. S. Finn and K. S. Thorne, Phys. Rev. D **62**, 124021 (2000).

[22] T. P. Sotiriou and A. Apostolatos, Phys. Rev. D **71**, 044005 (2005).

[23] C. Li, (In preparation).

[24] S. A. Teukolsky, Phys. Rev. Lett. **29**, 1114 (1972).

[25] J. B. Hartle, Phys. Rev. D **8**, 1010 (1973).

[26] J. B. Hartle, Phys. Rev. D **9**, 2749 (1974).

[27] K. S. Thorne, private communication.

[28] M. Colpi, S. L. Shapiro, and I. Wasserman, Phys. Rev. Lett. **57**, 2485 (1986).

[29] F. D. Ryan, Phys. Rev. D **55**, 6081 (1996).

[30] T. D. Lee and Y. Pang, Phys. Rev. D **35**, 3637 (1987).

[31] E. Poisson, Phys. Rev. D **70**, 084044 (2004).

[32] G. B. Cook and H. P. Pfeiffer, Phys. Rev. D **70**, 104016 (2004).

[33] J. Baker, M. Campanelli, C. O. Lousto, and R. Takahashi, Phys. Rev. D **65**, 124012 (2002).

[34] P. C. Peters, Phys. Rev. **136**, B1224 (1964).

[35] H. P. Pfeiffer, L. E. Kidder, M. A. Scheel, and S. A. Teukolsky, Comput. Phys. Commun. **152**, 253 (2003).

[36] L. Lindblom, M. A. Scheel, L. E. Kidder, R. Owen, and O. Rinne, Class. Quantum Grav. **23**, S447 (2006).

[37] M. A. Scheel, H. P. Pfeiffer, L. Lindblom, L. E. Kidder, O. Rinne, and S. A. Teukolsky, Phys. Rev. D **74**, 104006 (2006), `gr-qc/0607056`.

[38] H. P. Pfeiffer and J. W. York, Jr., Phys. Rev. D **67**, 044022 (2003).

[39] G. B. Cook, Living Rev. Rel. **5**, 1 (2000).

[40] A. Lichnerowicz, J. Math Pures et Appl. **23**, 37 (1944).

[41] J. W. York, Jr., Phys. Rev. Lett. **28**, 1082 (1972).

[42] J. W. York, Jr., in *Essays in general relativity*, F. Tipler, Ed., (Academic, New York, 1981), Chap. 4, p. 39.

[43] A. Garat and R. H. Price, Phys. Rev. D **61**, 124011 (2000).

Chapter 2

The dependence of test-mass thermal noises on beam shape in gravitational-wave interferometers

In second-generation, ground-based interferometric gravitational-wave detectors such as Advanced LIGO, the dominant noise at frequencies $f \sim 40$ Hz to ~ 200 Hz is expected to be due to thermal fluctuations in the mirrors' substrates and coatings which induce random fluctuations in the shape of the mirror face. The laser-light beam averages over these fluctuations; the larger the beam and the flatter its light-power distribution, the better the averaging and the lower the resulting thermal noise. In semi-infinite mirrors, scaling laws for the influence of beam shape on the four dominant types of thermal noise (coating Brownian, coating thermoelastic, substrate Brownian, and substrate thermoelastic) have been suggested by various researchers and derived with varying degrees of rigour. Because these scaling laws are important tools for current research on optimizing the beam shape, it is important to firm up our understanding of them. This paper (1) gives a summary of the prior work and of gaps in the prior analyses, (2) gives a unified and rigorous derivation of all four scaling laws, and (3) explores, relying on work by J. Agresti, deviations from the scaling laws due to finite mirror size.

Originally published as G. Lovelace, submitted to Class. Quantum Grav. (2007), preprint available online at `http://arxiv.org/abs/gr-qc/0610041`.

2.1 Introduction and summary

Second-generation interferometric gravitational wave detectors such as Advanced LIGO will be approximately ten times more sensitive than the current LIGO interferometers, leading to an improvement in event rate such that the first few hours of data at design sensitivity will contain more signals than the entire year-long science run that is presently under way [1]. In Advanced LIGO's most sensitive frequency band ($f \sim 40$ to 200 Hz), the sensitivity is limited by internal thermal noise, i.e., by noise in the substrates and reflective coatings of the four test masses (see, e.g., Fig. 1 of [2]). Lowering the internal thermal noise would increase Advanced LIGO's event rate throughout that band.

Internal thermal noise can be divided into two different types: *Brownian thermal noise* (due to imperfections in the substrate or coating material, which couple normal modes of vibration to each other) and *thermoelastic noise* (due to random flow of heat in the substrate or coating, which causes random thermal expansion). When the laser beam shape is Gaussian, the Brownian and thermoelastic noises in the substrate (e.g. [3]) and in the coating (e.g. [4, 5]) are well understood.

One way of lowering the internal thermal noise is to i) flatten the shape of the laser beam that measures the test mass position so it better averages over the mirror faces' fluctuating shapes, and ii) enlarge it to the largest size permitted by diffraction losses. A specific enlarged, flattened shape, the *mesa beam*, has been proposed by O'Shaughnessy and Thorne and explored (theoretically) in detail by them, d'Ambrosio, Strigin and Vyatchanin [6, 7, 8], and by Agresti and DeSalvo [9, 10]. The mesa shape was found to reduce the thermal noise powers by factors of order two, with corresponding significant increases in the distances to which the planned interferometers can search. Motivated by this, mesa beams are currently being explored experimentally [11, 12].

The mesa shape is unlikely to be optimal. Bondarescu and Chen (Caltech/AEI) are currently seeking the optimal beam shape for each of the four types of noise; they are also seeking a balance between the competing demands of the four optimal shapes. Further research will require balancing practical aspects of mirror design against the (possibly impractical) ideal shapes.

In all this current research, a crucial tool is a set of scaling laws for the dependence of the four types of thermal noise on the beam shape, in the limit of a mirror that is large compared to the beam diameter ("semi-infinite mirror"). These scaling laws have been proposed by various researchers over the past several years, and they have been derived with varying degrees of rigour, and in some cases with unnecessarily restrictive assumptions. This prior work will be discussed and critiqued in Sec. 2.2.2.

Because these scaling laws are so important for current research, this paper scrutinizes them and their accuracies in some detail. In Sec. 2.2 the scaling laws and assumptions underlying them are presented and prior research on them is described. Then in Sec. 2.3 a unified and rigorous derivation of all four scaling laws is presented. In Sec. 2.4 the breakdown of the scaling laws due to finite mirror size is explored. And finally, in Sec. 2.5 a few conclusions are given.

2.2 The scaling laws and prior research on them

2.2.1 Model and summary

To explore the effect of the beam shape on the internal thermal noise, I consider a cylindrical test mass substrate of radius R and thickness H and suppose that these size scales are comparable: $R \sim H$. I choose a cylindrical coordinate system (r, φ, z) such that $r = 0$ is the mirror axis, $z = 0$ is the reflectively coated surface of the mirror substrate, and points with $0 < z < H$ are inside the mirror substrate.

An axisymmetric laser beam with intensity profile $p(r)$ is normally incident on the mirror[1]. The intensity profile is normalized, so

$$2\pi \int_0^R \mathrm{d}r r p(r) = 1. \tag{2.1}$$

The beam measures $q(t)$, a weighted average of the mirror's longitudinal position $Z(r, \varphi, t)$ (Eq. (3) of [13])

$$q(t) \equiv \int_0^{2\pi} \mathrm{d}\varphi \int_0^R \mathrm{d}r r p(r) Z(r, \varphi, t). \tag{2.2}$$

In LIGO, so as to keep diffraction losses $\lesssim 1$ ppm, the beam radius over which, say, 95% of the signal $q(t)$ is collected, is kept significantly smaller than the mirror radius R and thickness H. This motivates the idealization of the mirror as a semi-infinite slab bounded by a plane, $R \to \infty$, $H \to \infty$. (The accuracy of this infinite-test-mass (ITM) approximation will be discussed in Sec. 2.4.2.)

Internal thermal noise will cause small fluctuations in the longitudinal position of the mirror $Z(r, \varphi, t)$. The spectral density S_q associated with the measurement of the mirror position q is given by the fluctuation dissipation theorem (Eq. (1) of [13]):

$$S_q = \frac{2k_B T}{\pi^2 f^2} \frac{W_{\mathrm{diss}}}{F^2}. \tag{2.3}$$

Here k_B is Boltzmann's constant, T is the temperature of the material, and W_{diss} is the power that would be dissipated if a longitudinal force of amplitude F, frequency f, and pressure distribution $p(r)$ were applied to the mirror surface (Levin's thought experiment [13]). Because the frequencies of interest (i.e., $f \sim 100$ Hz) are far below the lowest resonant frequencies of the mirror $f_{\mathrm{res}} \sim$ (a few km/s)/(about 10 cm) $\sim 10^4$ Hz, the hypothetical applied force can be idealized as static when computing the resulting strain of the mirror.

Thus the noise S_q can be computed using the following algorithm:

1. Statically deform the (semi-infinite) mirror with a force with amplitude F and pressure distribution $p(r)$ the same as the light's intensity profile;

---

[1] The shape of the mirror faces must also be changed slightly (by height changes $\lesssim$ one wavelength of the laser light) so that $p(r)$ is an eigenmode of the arm cavity. In this paper, I assume that the mirror faces take whatever shape is necessary to support a beam with intensity profile $p(r)$.

2. compute the Brownian and thermoelastic dissipated power $W_{\rm diss}$ due to the deformation caused by the applied force;
3. substitute $W_{\rm diss}$ into Eq. (2.3) to get the spectral density S_q of the thermal noise of a measurement of the average position q.

Note that from S_q, one can easily compute the thermally-induced gravitational-wave-strain noise power $S_h(f)$ in a measurement by the interferometer. If mirrors 1 and 2 are in one arm (of length $L = 4$ km), and mirrors 3 and 4 are in the other arm (also of length L), the interferometer measures $h \equiv [(q_1 - q_2) - (q_3 - q_4)]/L$, where $q_{1,2,3,4}$ are the measured positions of the four mirrors. Because the noises in the four test masses are uncorrelated, the spectral density S_h is just $S_h = (4/L^2)S_q$. In the remainder of this article, when referring to the noise of a single test mass, the subscript "q" will be suppressed (i.e., $S \equiv S_q$), while the gravitational-wave-strain noise power will always be referred to as S_h.

In Sec. 2.3.1, I compute the strain distribution that results from applying the pressure $Fp(r)$ to a homogeneous, isotropic, semi-infinite mirror with a very thin reflective coating of a possibly different material. The calculation is a straightforward generalization of Sec. 2 of [4]. In this calculation, I model the coating as a thin layer (of order microns, as compared to the cm size scales of the substrate) which adheres to the mirror surface. In Sec. 2.3.2 I use the strain distributions to compute each of the four types of thermal noise $S(f)$. I find that if $p_1(r)$ and $p_2(r)$ are two different beam shapes, then

$$\frac{S_{1,n}}{S_{2,n}} = \frac{\int_0^\infty {\rm d}k k^n \left[\tilde{p}_1(k)\right]^2}{\int_0^\infty {\rm d}k k^n \left[\tilde{p}_2(k)\right]^2} \tag{2.4}$$

where $n = 1$ for coating Brownian and coating thermoelastic noise, $n = 0$ for substrate Brownian noise, and $n = 2$ for substrate thermoelastic noise. Here $\tilde{p}(k)$ is (up to factors of 2π) the two-dimensional Fourier transform of $p(r)$ over the surface of the mirror:

$$\begin{aligned} \tilde{p}(k) &= \int_0^\infty {\rm d}r r J_0(kr) p(r), \\ p(r) &= \int_0^\infty {\rm d}k k J_0(kr) \tilde{p}(k). \end{aligned} \tag{2.5}$$

Here $J_0(x)$ is the $0^{\rm th}$ Bessel function of the first kind (the axisymmetry allows the 2D Fourier transform to reduce to a 1D Hankel transform).

If one knows $S_{1,n}$, computing $S_{2,n}$ amounts to computing simple integrals of $\tilde{p}(k)$. If one holds everything else fixed but changes the beam shape, the scaling law (2.4) makes it straightforward to determine the improvement in the thermal noises and the corresponding improvement in the interferometer sensitivity.

In the remainder of this paper, I derive these scaling laws, comment on their implications for Advanced LIGO, and estimate their accuracy for finite test masses. In Sec. 2.2.2, I discuss prior work related to the scaling laws. In Sec. 2.3.1, I compute the strain S_{ij} due to a hypothetical applied force with amplitude F and pressure distribution $p(r)$. Then, in Sec. 2.3.2, I compute the dissipated power $W_{\rm diss}$ for the Brownian and thermoelastic dissipation in the coating and the substrate and insert $W_{\rm diss}$ into Eq. (2.3) to determine how the noise depends on the beam shape. In Sec. 2.4.1, I discuss implications of this result for Advanced LIGO, and in Sec. 2.4.2 I discuss the accuracies of the infinite-test-mass (ITM) scaling laws by comparing with others' finite-test-mass (FTM) predictions for the cases of Gaussian and mesa beam shapes. I make some concluding remarks in Sec. 2.5.

2.2.2 Discussion of prior research

2.2.2.1 Thermoelastic substrate noise

In Levin's thought experiment, the dissipation associated with thermoelastic noise arises from heat flow down temperature gradients, which are induced by compression of the coating or substrate by the applied force. The increase in entropy corresponds to a dissipated power.

In 2003, in connection with his invention of the mesa beam and exploration of its properties, O'Shaughnessy used Levin's thought experiment to derive the following scaling law for the thermoelastic substrate noise:

$$S^{\rm TE}_{\rm sub} = C^{\rm TE}_{\rm sub} \int_0^\infty {\rm d}k k^2 \tilde{p}^2(k), \tag{2.6}$$

where $C^{\rm TE}_{\rm sub}$ does not depend on the beam shape. This scaling law ultimately motivated the other three. O'Shaughnessy included his derivation of this law as Appendix H of his (as yet unpublished) 2004 paper with Strigin and Vyatchanin [8] on mesa beams. He used a slightly different (but no less rigorous) method from the unified derivation I give in Sec. 2.3.2.4 [Eq. (2.38)]. O'Shaughnessy wrote the scaling law in terms of 2D Fourier transforms; the reduction to 1D Hankel transforms makes numerical evaluation of the scaling law (2.6) very efficient (Sec. 2.4.1).

2.2.2.2 Thermoelastic coating noise

Braginsky and Vyatchanin (Appendix B.2 of [5]) and Fejer and collaborators (Sec. IV D of [14]) have independently calculated the thermoelastic coating noise for Gaussian beam shapes (though the analysis in [5] is only valid when the coating and substrate elastic properties are identical [14]). Scrutinizing the derivation in [14], Thorne speculated in 2004 (unpublished) that the thermoelastic coating noise obeys a scaling law of the form

$$S^{\rm TE}_{\rm coat} = C^{\rm TE}_{\rm coat} \int_0^\infty {\rm d}k k \tilde{p}^2(k). \tag{2.7}$$

In 2006 I verified Thorne's conjecture via almost trivial generalizations of the Braginsky-Vyatchanin and Fejer et al. analyses; my derivation is given in Sec. 2.3.2.2 [Eq. (2.28)]. In 2006 O'Shaughnessy, learning of my work but not knowing my result, extended a clever dimensional analysis argument (Sec. 2.2.2.5) that he originally invented for Brownian coating noise (below) to the other three types of noises [15]; but for thermoelastic coating noise he got an answer that disagrees with Thorne's conjecture and my result (2.7). When I pointed out the discrepancy, O'Shaughnessy found an error in his dimensional analysis and revised his manuscript to give the correct scaling law (2.7) [16].

2.2.2.3 Brownian coating noise

In Levin's thought experiment, the dissipation associated with Brownian thermal noise can be modelled as arising from a loss angle, which is an imaginary (i.e., damping) correction to the material's Young's modulus caused by coating or substrate imperfections.

In 2004, Thorne communicated to O'Shaughnessy and Vyatchanin his conjecture (2.7) for the scaling law for thermoelastic coating noise, and challenged them to find an analogous scaling law for Brownian coating noise. Independently, they each devised simple arguments that led to the law

$$S_{\mathrm{coat}}^{\mathrm{BR}} = C_{\mathrm{coat}}^{\mathrm{BR}} \int_0^\infty \mathrm{d}r r p^2(r) = C_{\mathrm{coat}}^{\mathrm{BR}} \int_0^\infty \mathrm{d}k k \tilde{p}^2(k). \tag{2.8}$$

O'Shaughnessy gave both an argument based on dimensional analysis (Sec. 2.2.2.5) and a derivation for the special case that the substrate and coating have the same elastic properties. Vyatchanin's analysis [17] was based on a derivation for Gaussian beams, followed by an argument that, if a beam with another shape $p(r)$ can be constructed by superposing Gaussian beams, then this scaling law must hold also for that other shape.

The scaling law (2.8) is *local*, i.e., the noise at a point on the mirror depends only on the beam intensity *evaluated at that point*. Thorne's intuition, however, led him to believe (incorrectly) that the scaling law should be *nonlocal*[2]. Consequently, Thorne was so highly sceptical of O'Shaughnessy's and Vyatchanin's arguments and the claimed scaling law that he—unfortunately—dissuaded both O'Shaughnessy and Vyatchanin from publishing their arguments and result.

The following year (2005), Thorne, still sceptical of the O'Shaughnessy-Vyatchanin result (2.8), suggested to me that I carry out a detailed derivation of the Brownian-coating-noise scaling law from first principles. My analysis, based on Levin's method and reported in this paper, gave the result (2.8), in agreement with O'Shaughnessy and Vyatchanin, and motivated O'Shaughnessy to publish [16] his dimensional-analysis argument.

O'Shaughnessy's derivation is restricted (unrealistically) to identical elastic properties for substrate and coating. My derivation [Eq. (2.23) below] allows the substrate and the coating to have different elastic properties. Vyatchanin's derivation is valid only for those beam shapes that can be achieved by superposing Gaussians—though it might well be that any shape can be achieved in this

---

[2] It turns out (Sec. 2.3.2.1) that nonlocal terms *do* appear at intermediate steps in the derivation but *do not* contribute to the scaling law itself.

way. My derivation is definitely valid for any axially symmetric beam shape $p(r)$.

2.2.2.4 Brownian substrate noise

In 2005 Vinet proposed [18] the following scaling law for the substrate Brownian noise:

$$S_{\rm sub}^{\rm BR} = C_{\rm sub}^{\rm BR} \int_0^\infty \mathrm{d}k \tilde{p}^2(k). \tag{2.9}$$

He deduced this law as a trivial consequence of his Eqs. (1)–(3). He did not present a derivation of those equations, but he recognized that they can be obtained by generalizing the derivation in [19], which assumes that the beam shape is Gaussian. In Sec. 2.3.2.3, I explicitly derive Eq. (2.9). In parallel with my work, O'Shaughnessy applied his dimensional analysis technique to verify Vinet's scaling law (2.9).

2.2.2.5 Dimensional analysis

O'Shaughnessy's dimensional analysis argument, referred to above, consists of three steps:

1. The scaling laws must take the form of a translation-invariant inner product of $p(r)$ with itself, since the mirror is taken to be semi-infinite. In the Fourier domain, for axisymmetric beam shapes $p_1(r)$ and $p_2(r)$, the scaling law must then take the form:

$$\frac{S_1}{S_2} = \frac{\int_0^\infty \mathrm{d}k k \tilde{G}(k) \tilde{p}_1^2(k)}{\int_0^\infty \mathrm{d}k k \tilde{G}(k) \tilde{p}_2^2(k)}. \tag{2.10}$$

2. The only length scale (other than the width of the beam) is the small coating thickness d, so $\tilde{G}(k) = k^n d$ for coating thermal noise and $\tilde{G}(k) = k^n$ for substrate thermal noise.

3. The power n is chosen by demanding that, when the beam shape is a Gaussian, the noise scale as the correct power of the beam width.

This argument turns out to produce the correct scaling laws, but without sufficient care, it can also lead one amiss. For instance, when considering thermoelastic coating noise, step (ii) must be amended, since there *is* a second length scale: the characteristic length of diffusive heat flow [5, 14]. In his original manuscript [15], O'Shaughnessy neglected this second length scale, and incorrectly deduced that $n = 3$ for coating thermoelastic noise. After I contacted O'Shaughnessy regarding this error, he corrected his analysis [16] and obtained the same result, $n = 1$, as I had derived (Sec. 2.3.2.2) below.

2.3 Derivation of the infinite-test-mass (ITM) scaling laws

2.3.1 Strain of a semi-infinite body with thin facial coatings due to a static, axisymmetric force

The thermal noise is determined by the symmetric part of the strain S_{ij} that the test mass would experience if a normal force with pressure $p(r)$ were applied to the mirror surface. In this section, I evaluate S_{ij} in the mirror substrate and coating. In Sec. 2.3.2, I use these results to compute W_{diss} [which, by Eq. (2.3), determines the thermal noise].

If the displacement vector of an element of the test mass is u_i, then the strain S_{ij} is $S_{ij} = \nabla_j u_i$. Following the methods developed in [19] (but correcting some typographical errors), Eq. (19) of [3] gives the cylindrical components of the displacement of the test mass substrate:

$$u_r = \frac{1}{2\mu}\int_0^\infty \mathrm{d}k J_1(kr)\mathrm{e}^{-kz}\left(1-\frac{\lambda+2\mu}{\lambda+\mu}+kz\right)\tilde{p}(k), \tag{2.11a}$$

$$u_\varphi = 0, \tag{2.11b}$$

$$u_z = \frac{1}{2\mu}\int_0^\infty \mathrm{d}k J_0(kr)\mathrm{e}^{-kz}\left(1+\frac{\mu}{\lambda+\mu}+kz\right)\tilde{p}(k). \tag{2.11c}$$

Here λ and μ are the Lamé coefficients of the substrate. The vector u_i satisfies the equilibrium equation $\nabla_j T_{ij} = 0$. (Throughout this paper, I use the Einstein summation convention.)

The non-vanishing components of the symmetric part of the strain are [with commas denoting partial derivatives]

$$\theta = S_{ii}, \tag{2.12a}$$

$$S_{rr} = u_{r,r} = \theta - S_{zz} - S_{\varphi\varphi}, \tag{2.12b}$$

$$S_{\varphi\varphi} = \frac{u_r}{r}, \tag{2.12c}$$

$$S_{(rz)} = S_{(zr)} = \frac{1}{2}(u_{r,z}+u_{z,r}), \tag{2.12d}$$

$$S_{zz} = u_{z,z}. \tag{2.12e}$$

Evaluating the derivatives of Eqs. (2.11a)–(2.11c) and inserting the result into Eqs. (2.12a)–(2.12e) gives

$$\theta = \frac{1}{2\mu}\int_0^\infty \mathrm{d}k k J_0(kr)\left(\frac{-2\mu}{\lambda+\mu}\right)\mathrm{e}^{-kz}\tilde{p}(k), \tag{2.13a}$$

$$S_{rr} = \theta - S_{zz} - S_{\varphi\varphi}, \tag{2.13b}$$

$$S_{\varphi\varphi} = \frac{1}{2\mu}\int_0^\infty \mathrm{d}k \frac{J_1(kr)}{r}\mathrm{e}^{-kz}\left(1-\frac{\lambda+2\mu}{\lambda+\mu}+kz\right)\tilde{p}(k), \tag{2.13c}$$

$$S_{(zr)} = -\frac{1}{2\mu}\int_0^\infty \mathrm{d}k k J_1(kr)(kz)\mathrm{e}^{-kz}\tilde{p}(k), \tag{2.13d}$$

$$S_{zz} = \frac{1}{2\mu}\int_0^\infty \mathrm{d}k k J_0(kr)\left(-\frac{\mu}{\lambda+\mu}-kz\right)\mathrm{e}^{-kz}\tilde{p}(k). \tag{2.13e}$$

Setting $z = 0$ in Eqs. (2.13a)–(2.13e) and combining with Eq. (2.5) yields the nonvanishing stresses on the substrate surface:

$$\theta|_{z=0} = \left(\frac{-1}{\lambda+\mu}\right)p(r), \tag{2.14a}$$

$$S_{rr}\,|_{z=0} = \frac{1}{2}\left(\frac{-1}{\lambda+\mu}\right)p(r) - S_{\varphi\varphi}\,|_{z=0}\,, \tag{2.14b}$$

$$S_{\varphi\varphi}\,|_{z=0} = \frac{1}{2}\left(\frac{-1}{\lambda+\mu}\right)\int_0^\infty \mathrm{d}k\frac{J_1(kr)}{r}\tilde{p}(k), \tag{2.14c}$$

$$S_{zz}|_{z=0} = \frac{1}{2}\left(\frac{-1}{\lambda+\mu}\right)p(r). \tag{2.14d}$$

Here I have used the identity

$$\int_0^\infty \mathrm{d}k k J_0(kr) J_0(kr') = \frac{\delta(r'-r)}{r'}. \tag{2.15}$$

Note that on the surface of the substrate θ and S_{zz} are *local* [i.e., their values at any point depend only on the value of $p(r)$ at that point], while $S_{\varphi\varphi}$ is *nonlocal.* The component S_{rr} can be written as the sum of a local part and a nonlocal part; the nonlocal part of S_{rr} is just $-S_{\varphi\varphi}$.

The thin-coating approximation gives the nonvanishing components of the coating strain in terms of the strain on the substrate surface (Eq. (A4) of [4]):

$$\begin{aligned}
\theta^{\text{coat}} &= \frac{\lambda + 2\mu_{\text{coat}}}{\lambda_{\text{coat}} + 2\mu_{\text{coat}}} \left(\theta - S_{zz}\right)|_{z=0} \\
&\quad + \frac{\lambda + 2\mu}{\lambda_{\text{coat}} + 2\mu_{\text{coat}}} S_{zz}|_{z=0}\,, && \text{(2.16a)} \\
S_{rr}^{\text{coat}} &= S_{rr}|_{z=0} = \theta^{\text{coat}} - S_{\varphi\varphi}^{\text{coat}} - S_{zz}^{\text{coat}}, && \text{(2.16b)} \\
S_{\varphi\varphi}^{\text{coat}} &= S_{\varphi\varphi}|_{z=0}\,, && \text{(2.16c)} \\
S_{zz}^{\text{coat}} &= \frac{\lambda - \lambda_{\text{coat}}}{\lambda_{\text{coat}} + 2\mu_{\text{coat}}} \left(\theta - S_{zz}\right)|_{z=0} \\
&\quad + \frac{\lambda + 2\mu}{\lambda_{\text{coat}} + 2\mu_{\text{coat}}} S_{zz}|_{z=0}\,. && \text{(2.16d)}
\end{aligned}$$

In [4], these conditions are said to hold in the limit that the Poisson ratio of the substrate and coating are “not too different,” but this restriction is unnecessary (see 2.7).

Finally, after inserting Eqs. (2.14a)–(2.14d) into Eqs. (2.16a)–(2.16d) I conclude that θ^{coat} and S_{zz}^{coat} are *local*; while $S_{\varphi\varphi}^{\text{coat}}$ and S_{rr}^{coat} are *nonlocal*. However, this nonlocality turns out *not* to influence the coating noises. This is because, after using Eq. (2.16b) to eliminate S_{rr}^{coat}, it turns out that the remaining nonlocal part $S_{\varphi\varphi}^{\text{coat}}$ only appears in the coating W_{diss} [according to Eqs. (2.22) and (2.27)] via the integral

$$\int_0^\infty \mathrm{d}r r S_{(ij)}^{\text{coat}} S_{(ij)}^{\text{coat}} = \int_0^\infty \mathrm{d}r r \left[(S_{rr}^{\text{coat}})^2 + (S_{\varphi\varphi}^{\text{coat}})^2 + (S_{zz}^{\text{coat}})^2 \right]$$
$$= \int_0^\infty \mathrm{d}r r \left[\left(\theta^{\text{coat}} - S_{zz}^{\text{coat}}\right)^2 + (S_{zz}^{\text{coat}})^2 + 2(S_{\varphi\varphi}^{\text{coat}})^2 - 2S_{\varphi\varphi}^{\text{coat}}\left(\theta^{\text{coat}} - S_{zz}^{\text{coat}}\right) \right]. \tag{2.17}$$

In 2.6, I show that

$$\int_0^\infty \mathrm{d}r r (S_{\varphi\varphi}^{\text{coat}})^2 - S_{\varphi\varphi}^{\text{coat}}\left(\theta^{\text{coat}} - S_{zz}^{\text{coat}}\right) = 0, \tag{2.18}$$

so only the local parts of the strain (θ^{coat} and S_{zz}^{coat}) influence the thermal noise. This fact turns out to imply local coating scaling laws in agreement with O’Shaughnessy’s [16] and Vyatchanin’s [17] arguments (Sec. 2.3.2).

2.3.2 Internal thermal noise

2.3.2.1 Brownian coating noise

For Brownian thermal noise in an elastic material, the dissipated power is [Eq. (12) of [13] with a static applied force and with $U = -(1/2)S_{ij}T_{ij}$]

$$W_{\rm diss} = -\pi f \int_0^d {\rm d}z \int_0^{2\pi} {\rm d}\varphi \int_0^\infty {\rm d}r r \phi(f) S_{ij} T_{ij}. \tag{2.19}$$

Here ϕ is the loss angle (i.e., the imaginary, damping part of the Young's modulus of the coating material) and T_{ij} is the stress. When the material is the thin reflective coating of a mirror, there are effectively *two* loss angles [4], $\phi_\parallel$ and $\phi_\perp$, defined so that in the previous equation

$$\begin{aligned} \phi(f)S_{ij}T_{ij} &\rightarrow \phi_\parallel(f)\left(S^{\rm coat}_{rr}T^{\rm coat}_{rr} + S^{\rm coat}_{\varphi\varphi}T^{\rm coat}_{\varphi\varphi}\right) + \phi_\perp(f) S^{\rm coat}_{zz}T^{\rm coat}_{zz} \\ &= \phi_\parallel(f) S^{\rm coat}_{ij}T^{\rm coat}_{ij} + \left(\phi_\perp - \phi_\parallel\right) S^{\rm coat}_{zz}T^{\rm coat}_{zz}. \end{aligned} \tag{2.20}$$

This result can be obtained by combining Eqs. (4) and (13)–(15) of [4] with Eq. (9) of [13] and recalling that in the coating, the strain [Eqs. (2.16a)–(2.16d)] is diagonal.

For a homogeneous coating, the stress $T^{\rm coat}_{ij}$ is

$$T^{\rm coat}_{ij} = -\lambda^{\rm coat}\theta^{\rm coat}\delta_{ij} - 2\mu^{\rm coat}S^{\rm coat}_{(ij)}, \tag{2.21}$$

where $\lambda^{\rm coat}$ and $\mu^{\rm coat}$ are the Lamé coefficients of the coating, $S^{\rm coat}_{(ij)}$ is the symmetric part of the coating strain, and $\theta \equiv S_{ii}$ is the expansion. Combining Eqs. (2.20), (2.19), and (2.21) gives the following expression for $W_{\rm diss}$:

$$\begin{aligned} W_{\rm diss} &= 2\pi^2 f d \phi_\parallel(f) \int_0^\infty {\rm d}r r A + 2\pi^2 f d \left[\phi_\perp(f) - \phi_\parallel(f)\right] \int_0^\infty {\rm d}r r B, \\ A &= \left(\lambda^{\rm coat}\theta^2_{\rm coat} + 2\mu^{\rm coat}S^{\rm coat}_{(ij)}S^{\rm coat}_{(ij)}\right), \\ B &= S^{\rm coat}_{zz}\left(\lambda^{\rm coat}\theta^{\rm coat} + 2\mu^{\rm coat}S^{\rm coat}_{zz}\right). \end{aligned} \tag{2.22}$$

Combining Eqs. (2.22), (2.16a)–(2.16d), (2.14a)–(2.14d), and (2.18) and then inserting the result into Eq. (2.3) gives the spectral density S of the Brownian coating noise. However, for the present purpose, only terms involving the beam shape are relevant. Absorbing all other terms into a single constant $C^{\rm BR}_{\rm coat}$ yields

$$S^{\rm BR}_{\rm coat} = C^{\rm BR}_{\rm coat} \int_0^\infty {\rm d}r r p^2(r). \tag{2.23}$$

This is a local scaling law; i.e., the noise at each point on the mirror's surface is proportional to the square of the beam intensity there. This law is the same as O'Shaughnessy's [16] and Vyatchanin's

[17] scaling law for the Brownian coating thermal noise.

Parseval's equation [which follows from Eq. (2.5)] makes it easy to rewrite this scaling law in the Fourier domain, which will facilitate comparison with the substrate noise. The result is

$$S^{\rm BR}_{\rm coat} = C^{\rm BR}_{\rm coat} \int_0^\infty {\rm d}k k \tilde{p}^2(k). \tag{2.24}$$

2.3.2.2 Thermoelastic coating noise

The calculation of the thermoelastic coating noise is similar to the calculation of Brownian coating noise. But now, in response to the static, normal applied pressure $p(r)$, the dissipated power $W_{\rm diss}$ is caused by heat flow, $\propto \nabla\delta T$, down a temperature gradient $\nabla\delta T$ caused by the material's deformation:

$$W_{\rm diss} = \frac{\pi\kappa}{T} \int_0^\infty {\rm d}z \int_0^\infty {\rm d}r r \left(\nabla\delta T\right)^2 . \tag{2.25}$$

[Eq. (5) of [3] in the case of a static applied force and after evaluating the time average and trivial φ integral]. Here T is the temperature of the coating in the absence of the deformation and κ is the material's coefficient of thermal conductivity.

Braginsky and Vyatchanin [5] and Fejer and collaborators [14] have independently solved for the thermoelastic coating noise. The results obtained in [5] are correct only when the coating and substrate have the same elastic properties (Sec. I in [14]); however, this restriction is not relevant here, since [14] and [5] agree on the coating thermoelastic noise's dependence on the beam shape $p(r)$.

If the temperature change were adiabatic, δT would simply be proportional to $\theta^{\rm coat}$ (see, e.g., Eq. (12) of [3]). (Physically, this simply means that the temperature of an element in the coating changes linearly with volume.) However, as noted in [5], the diffusive heat characteristic length ℓ_D of the substrate and coating (on the order of mm) is far larger than the coating thickness d (which is on the order of a few microns). Because diffusive heat flow in the longitudinal direction is *not* negligible, heat flow in the direction normal to the coating cannot be treated adiabatically [5]. By contrast, the *substrate* thermoelastic noise *can* be treated adiabatically (Sec. 2.3.2.4), as can the heat flow in the plane of the coating ("tangential" heat flow).

Because the tangential heat flow is adiabatic, $\partial\delta T/\partial r \sim \theta/w$, where $w \sim$ cm is the length scale over which $p(r)$ varies. On the other hand, $\partial\delta T/\partial z \sim \theta/\ell_D$, where $\ell_D \sim$ mm is the diffusive heat characteristic length. Because the tangential derivatives are much smaller than the longitudinal derivatives, all derivatives except $\partial/\partial z$ may be neglected. It follows that $W_{\rm diss}$ will depend only on $p(r)$ and not on its radial derivatives.

Based on these observations, Braginsky and Vyatchanin [5] and Fejer and collaborators [14] solve the thermoconductivity equation (e.g., Eq. (1) of [14]) for the temperature perturbations δT. Both

[5] and [14] assume that the beam shape is Gaussian, but it is quite easy to generalize their arguments to non-Gaussian beam shapes. Combining Eqs. (B5)–(B7), (66), and (68) of [14] (but now regarding their function $\rho(r)$ as a generic beam shape) shows that the temperature perturbations in the coating have the form

$$\delta T \propto p(r) \times F(z), \tag{2.26}$$

where $F(z)$ is a function of z only. [Equivalently, Eq. (2.26) can be obtained by combining Eqs. (B.10) and (B.12) of [5] (but now regarding θ as an expansion corresponding to a generic beam shape) with Eqs. (2.14a) and (2.16a).] The precise form of $F(z)$ is given in [5] and [14] but is not needed in the present discussion.

Next, Braginsky and Vyatchanin compute the squared gradient $(\nabla \delta T)^2 \simeq (\partial \delta T/\partial z)^2$ in Eq. (2.25) to obtain W_{diss}; Fejer and collaborators instead compute W_{diss} by considering the interaction of i) the *unperturbed* stress and strain [i.e., the stress and strain due to $p(r)$ when temperature perturbations are neglected], and ii) the (complex) *perturbations* of the stress and strain caused by the small temperature perturbations δT. Both methods lead to the following expression for W_{diss}: (Eqs. (B.13) and (B.10) of [5]; Eq. (69) of [14])

$$W_{\mathrm{diss}} = \mathrm{const} \times \int_0^\infty \mathrm{d}r r p^2(r). \tag{2.27}$$

Plugging this result into Eq. (2.3) gives the scaling law

$$S_{\mathrm{coat}}^{\mathrm{TE}} = C_{\mathrm{coat}}^{\mathrm{TE}} \int_0^\infty \mathrm{d}r r p^2(r) = C_{\mathrm{coat}}^{\mathrm{TE}} \int_0^\infty \mathrm{d}k k \tilde{p}^2(k). \tag{2.28}$$

This is the same scaling law as for Brownian coating thermal noise. The coating thermoelastic noise is local and is the same as O'Shaughnessy's [16] and Vyatchanin's [17] law for Brownian coating thermal noise.

2.3.2.3 Brownian substrate noise

For Brownian substrate thermal noise there is only one relevant loss angle, ϕ, so the dissipated power is (Eq. (49) of [3] with a static applied force)

$$W_{\mathrm{diss}} = 2\pi^2 f \phi(f) \int_0^\infty \mathrm{d}z \int_0^\infty \mathrm{d}r r \left(\lambda \theta^2 + 2\mu S_{(ij)} S_{(ij)}\right). \tag{2.29}$$

The integral of the squared strain can be expanded as

$$\int_0^\infty \mathrm{d}z \int_0^\infty \mathrm{d}r r S_{(ij)} S_{(ij)} = \int_0^\infty \mathrm{d}z \int_0^\infty \mathrm{d}r r \left(S_{rr}^2 + S_{\varphi\varphi}^2 + S_{zz}^2\right)$$
$$= \int_0^\infty \mathrm{d}z \int_0^\infty \mathrm{d}r r \big[\left(\theta - S_{zz}\right)^2 + S_{zz}^2 + 2S_{(rz)}^2 + 2S_{\varphi\varphi}^2 - 2S_{\varphi\varphi}\left(\theta - S_{zz}\right) \big]. \tag{2.30}$$

In 2.6, I show that

$$\int_0^\infty \mathrm{d}r r \left[S_{\varphi\varphi}^2 - S_{\varphi\varphi}\left(\theta - S_{zz}\right)\right] = 0. \tag{2.31}$$

Substituting this result into Eq. (2.30) yields

$$W_{\text{diss}} = 2\pi^2 f \phi(f) \int_0^\infty \mathrm{d}z \int_0^\infty \mathrm{d}r r \Big[\lambda\theta^2 + 2\mu\left(\theta - S_{zz}\right)^2 + 2\mu S_{zz}^2 + 4\mu S_{(rz)}^2\Big]. \tag{2.32}$$

This expression can be evaluated term by term. Inserting Eq. (2.13a) into the integral of θ^2 gives

$$I_\theta \equiv \int_0^\infty \mathrm{d}z \int_0^\infty \mathrm{d}r r \theta^2$$
$$= \frac{1}{4\mu^2}\left(\frac{2\mu}{\lambda+\mu}\right)^2 \int_0^\infty \mathrm{d}k k \tilde{p}(k) \int_0^\infty \mathrm{d}k' k' \tilde{p}(k') \int_0^\infty \mathrm{d}z \mathrm{e}^{-(k+k')z} \int_0^\infty \mathrm{d}r r J_0(kr) J_0(k'r). \tag{2.33}$$

Using the identity

$$\int_0^\infty \mathrm{d}r r J_n(kr) J_n(k'r) = \frac{\delta(k-k')}{k} \tag{2.34}$$

on Eq. (2.33) and evaluating the integral over z yields

$$I_\theta = \frac{1}{8\mu^2}\left(\frac{2\mu}{\lambda+\mu}\right)^2 \int_0^\infty \mathrm{d}k \tilde{p}^2(k). \tag{2.35}$$

The other terms in Eq. (2.32) can be evaluated similarly; they all turn out to have the same dependence on $\tilde{p}(k)$ as I_θ. Inserting this result for W_{diss} into Eq. (2.3) gives the scaling law

$$S_{\text{sub}}^{\text{BR}} = C_{\text{sub}}^{\text{BR}} \int_0^\infty \mathrm{d}k \tilde{p}^2(k). \tag{2.36}$$

This scaling law is the same as the scaling law (2.24) for the coating thermal noise except that the z integration has reduced the power of k in the integrand by one. This scaling law agrees with Eqs. (1)–(2) of [18].

2.3.2.4 Thermoelastic substrate noise

In contrast to the case of coating thermoelastic noise, the substrate thermoelastic noise *can* be treated using the adiabatic approximation. Therefore, the temperature perturbations δT that drive the substrate thermoelastic noise $S_{\mathrm{sub}}^{\mathrm{TE}}$ are proportional to the expansion, i.e., $\delta T \propto \theta$. This implies (e.g., by Eq. (2.25), or Eq. (13) of [3])

$$S_{\mathrm{sub}}^{\mathrm{TE}} = C_{\mathrm{sub}}^{\mathrm{TE}} \int_0^\infty \mathrm{d}z \int_0^\infty \mathrm{d}r r (\nabla \theta)^2 \tag{2.37}$$

with $C_{\mathrm{sub}}^{\mathrm{TE}}$ independent of the strain (and thus also the beam shape). Inserting Eq. (2.13a) into Eq. (2.37) gives the scaling law; after absorbing all constants into $C_{\mathrm{sub}}^{\mathrm{TE}}$, it takes the form

$$S_{\mathrm{sub}}^{\mathrm{TE}} = C_{\mathrm{sub}}^{\mathrm{TE}} \int_0^\infty \mathrm{d}k k^2 \tilde{p}^2(k), \tag{2.38}$$

which O'Shaughnessy, Strigin, and Vyatchanin obtain in [8]. This scaling law is the same as the scaling law (2.36) for the substrate Brownian noise except that the gradient raises the power of k by two.

2.4 Applying the ITM scaling laws to second-generation gravitational-wave interferometers

To illustrate the scaling laws (2.23), (2.28), (2.36), and (2.38), suppose that the noise $S_{\tau,k}$ [with beam shape $p_k(r)$ and thermal noise type τ] is known. Here and throughout the remainder of this article, τ is a label that takes one of the following values: coating Brownian (Coat BR), coating thermoelastic (Coat TE), substrate Brownian (Sub BR), or substrate thermoelastic (Sub TE).

Now, if the beam shape were changed to $p_u(r)$ [while holding everything[3] else fixed], then the unknown noise $S_{\tau,u}$ [with beam shape $p_u(r)$] would be [Eq. (2.4)]:

$$S_{\tau,u} = C_{\mathrm{ITM}}^2[\tau; p_u, p_k] S_{\tau,k}, \tag{2.39}$$

with

$$C_{\mathrm{ITM}}^2[\tau; p_u, p_k] \equiv \frac{\int_0^\infty \mathrm{d}k k^{n(\tau)} \tilde{p}_u^2(k)}{\int_0^\infty \mathrm{d}k k^{n(\tau)} \tilde{p}_k^2(k)} \tag{2.40}$$

and

$$n(\tau) \equiv \begin{cases} 1 & : \quad \tau = \text{Coat BR or Coat TE} \\ 0 & : \quad \tau = \text{Sub BR} \\ 2 & : \quad \tau = \text{Sub TE} \end{cases} . \tag{2.41}$$

When the beam shape is changed from p_k to p_u, the amplitude sensitivity changes by a factor

---

[3] Since here I am neglecting edge effects, "everything" means the temperature, the materials' elastic and thermal properties, the coating thickness, and the frequency. In Sec. 2.4.2, when edge effects are considered, it will be the diffraction loss, not the mirror size, that is held fixed.

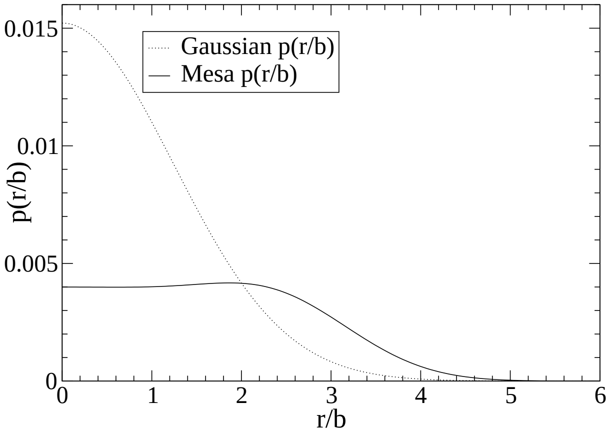

Figure 2.1: A plot of $p_{\mathrm{gauss}}(r/b)$ and $p_{\mathrm{mesa}}(r/b)$ for beams with 1 ppm diffraction losses (in the clipping approximation) on a mirror with radius $R = 17$ cm. Here $b = \sqrt{L\lambda/2\pi} = 2.6$ cm is the width of the smallest Gaussian beam that can resonate in a LIGO arm cavity with length $L = 4$ km and light wavelength $\lambda = 1064$ nm.

of $C_{\mathrm{ITM}}[\tau; p_u, p_k]$.

2.4.1 Implications for Advanced LIGO

In Advanced LIGO, the thermal noise may be significantly reduced by changing the shape of the laser beam. One proposal is to replace the Gaussian beam shape with a mesa beam (also called a flat-top beam) [6]. O'Shaughnessy, Strigin, and Vyatchanin [8] have calculated the resulting reduction in substrate thermoelastic noise, Vinet has done the same for substrate Brownian thermal noise [18], and Agresti [2] and Agresti and DeSalvo [9, 10] have done the same for both substrate and coating thermal noises—all for the realistic case of finite mirrors. The reduction in thermal noise can also be understood as a consequence of the simple ITM scaling laws derived above. Although I only compare Gaussian and flat-top beams here, the scaling law given in Eq. (2.4) makes it simple—if one neglects finite-test-mass (FTM) effects—to compute the relative change in sensitivity for any two beam shapes.

The normalized Gaussian beam shape is

$$p_{\mathrm{gauss}}(w; r) = \frac{\mathrm{e}^{-r^2/w^2}}{\pi w^2} \tag{2.42}$$

where w is the width of the Gaussian beam. It is straightforward to compute $\tilde{p}_{\mathrm{gauss}}(w; k)$, since the integral can be done analytically; the result is

$$\tilde{p}_{\mathrm{gauss}}(w; k) = \int_0^\infty \mathrm{d}r r J_0(kr) \frac{\mathrm{e}^{-r^2/w^2}}{\pi w^2} = \frac{1}{2\pi} \mathrm{e}^{-k^2 w^2/4}. \tag{2.43}$$

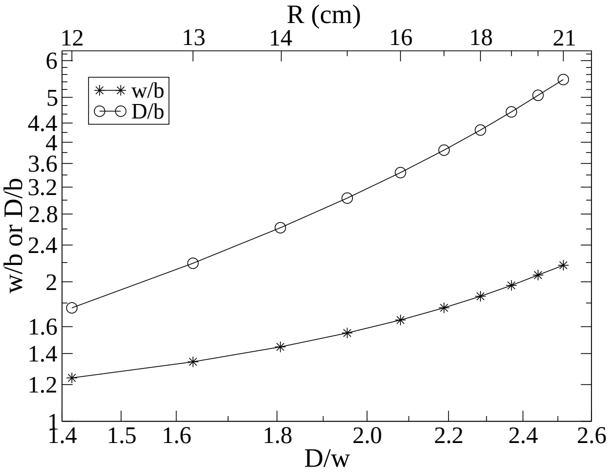

Figure 2.2: A log-log plot of the Gaussian beam-width parameter w and mesa beam-width parameter D as a function of mirror radius R (top of figure), for mirrors with 1 ppm diffraction loss in the clipping approximation. The ratio D/w is shown on the bottom of the figure. The parameter b is defined in Fig. 2.1.

In position space, the mesa beam can be written as (Eq. (2.5) of [7])

$$p_{\rm mesa}(D;r) \quad = \quad N\left|2\pi\int_0^D {\rm d}r' r' \exp\left[-\frac{(r^2+r'^2)(1-{\rm i})}{2b^2}\right]\times I_0\left[\frac{rr'(1-{\rm i})}{b^2}\right]\right|^2. \qquad (2.44)$$

Here D is a measure of the width of the beam, $b \equiv \sqrt{\lambda L/2\pi}$, with $L = 4$ km the arm length and $\lambda = 1064$ nm the wavelength of the laser beam's primary frequency, and N is a normalization constant adjusted so Eq. (2.1) is satisfied. Note that $p_{\rm mesa}(r)$ must be evaluated numerically; to compute $\tilde{p}(k)$ efficiently, I use the Fast Hankel Transform algorithm [20].

Examples of the Gaussian and mesa shapes are plotted in Fig. 2.1. In Fig. 2.2, the width parameters w and D of a sequence[4] of Gaussian and mesa beams are plotted as a function of mirror radius R for beams with 1 ppm of diffraction loss in the clipping approximation[5]. The ratio D/w is also shown on the bottom horizontal axis. It is sometimes useful to regard D and w (for 1 ppm losses) as functions of D/w rather than of R—with D/w actually being a surrogate for R.

The following three cases use Eqs. (2.39)–(2.41) to illustrate how the thermal noise in Advanced LIGO changes with different choices of Gaussian and mesa beam shapes.

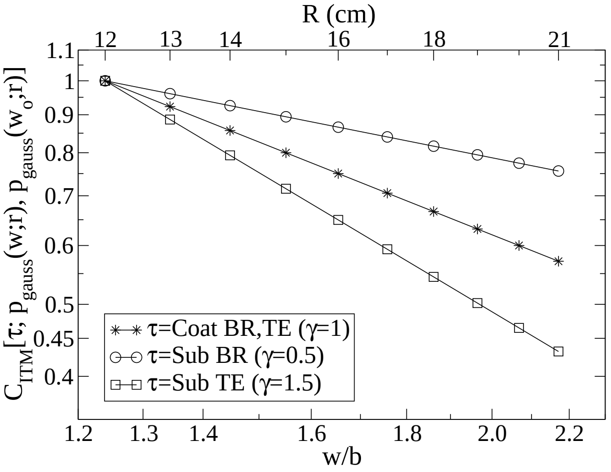

Figure 2.3: The scaling of thermal noises with beam width w for Gaussian beams in the infinite-test-mass (ITM) approximation. More specifically: a log-log plot of $C_{\mathrm{ITM}}[\tau; p_{\mathrm{gauss}}(w;r), p_{\mathrm{gauss}}(w_o;r)]$ as a function of w/b. Here $w_o/b = 1.24$, which corresponds to $R = 12$ cm and 1 ppm diffraction losses. Each curve is a power law obeying $C \propto 1/w^{\gamma}$.

2.4.1.1 Noise of a resized Gaussian beam

Suppose $p_k(r) = p_{\mathrm{gauss}}(w_o;r)$. Then the thermal noises for a Gaussian beam of some different size w are determined by evaluating $C_{\mathrm{ITM}}[\tau; p_{\mathrm{gauss}}(w;r), p_{\mathrm{gauss}}(w_o;r)]$ [Eq. (2.40)] and inserting the result into Eq. (2.39). In this well-known case (see, e.g., the discussion and references in [10]), C_{ITM} can be evaluated analytically, yielding the following relation:

$$C^2_{\mathrm{ITM}}[\tau; p_{\mathrm{gauss}}(w;r), p_{\mathrm{gauss}}(w_o;r)] \propto \frac{1}{w^{n(\tau)+1}}. \tag{2.45}$$

In Fig. 2.3, $C_{\mathrm{ITM}}[\tau; p_{\mathrm{gauss}}(w;r), p_{\mathrm{gauss}}(w_o;r)]$ is plotted as a function of the beam width w.

2.4.1.2 Noise of a resized mesa beam

Suppose $p_k(r) = p_{\mathrm{mesa}}(D_o;r)$. Then the thermal noises for a mesa beam of some different size D are determined by evaluating $C_{\mathrm{ITM}}[\tau; p_{\mathrm{mesa}}(D;r), p_{\mathrm{mesa}}(D_o;r)]$ [Eq. (2.40)] and inserting the results into Eq. (2.39). As shown in Fig. 2.4, in this case C_{ITM} does not scale as an exact power of D (although the actual relations are very well approximated by power laws).

---

[4] This particular sequence was chosen to facilitate comparison with the results of [10], which includes edge effects.

[5] In the clipping approximation, the diffraction loss is simply $2\pi \int_R^\infty dr r p(r)$, where R is the mirror radius. In the ITM approximation, R is larger than all other length scales; however, the actual, finite value of R must be used in the clipping approximation for the diffraction loss to be nonvanishing.

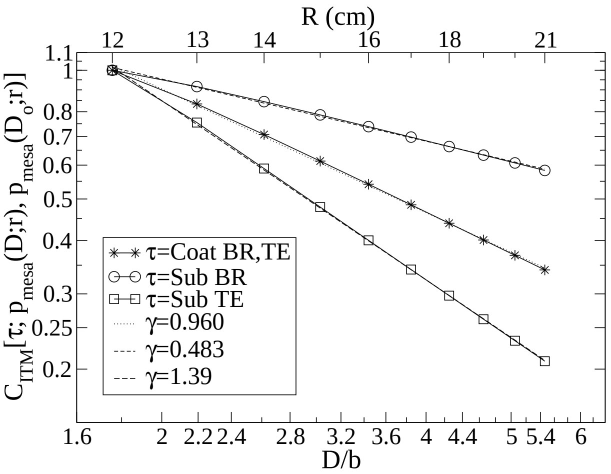

Figure 2.4: The scaling of thermal noises with beam-width parameter D for mesa beams in the infinite-test-mass approximation. More specifically: a log-log plot of $C_{\rm ITM}[\tau; p_{\rm mesa}(D;r), p_{\rm mesa}(D_o;r)]$ as a function of D/b. Here $D_o/b = 1.76$, which corresponds to a mirror radius of 12 cm and 1 ppm diffraction losses. The curves are well approximated by power laws of the form $C \propto 1/D^\gamma$.

2.4.1.3 Noise reduction by switching from a Gaussian beam to a mesa beam with the same diffraction loss and mirror radius

Finally, the scaling law (2.39) can be used to estimate the reduction in thermal noise by switching from a Gaussian beam to a mesa beam that has the same clipping-approximation diffraction loss on a mirror of the same radius.

Two complications in the resized-beam scalings are not present when scaling from Gaussian to mesa beams. First, while the original and resized beams were associated with different-sized mirrors, now the Gaussian and mesa beams are associated with the *same* mirror. Second, when relating the Gaussian and mesa beams, there is no need to specify a fiducial beam size (i.e., there is no analogue of w_o and D_o). Without these two complications, the Gaussian-to-mesa scaling is perhaps conceptually cleaner than the resized-beam scalings.

Fig. 2.5 shows $C_{\rm ITM}[\tau; p_{\rm mesa}(D;r), p_{\rm gauss}(w;r)]$ for the sequence of beams shown in Fig. 2.2 (beams with 1 ppm diffraction loss in mirrors of the same radius R). The relative improvement in amplitude sensitivity increases monotonically with the mirror radius R, or equivalently, with D/w; however, when edge effects (i.e., finite-test-mass effects) are included, there is a limit to how much the sensitivity can be improved (Sec. 2.4.2).

2.4.2 Errors due to neglecting finite-test-mass (FTM) effects

In the previous section, the ITM scaling laws predicted that, if the diffraction losses are held fixed, then the coating and substrate noises decrease monotonically with increasing beam width [Figs. 2.3,

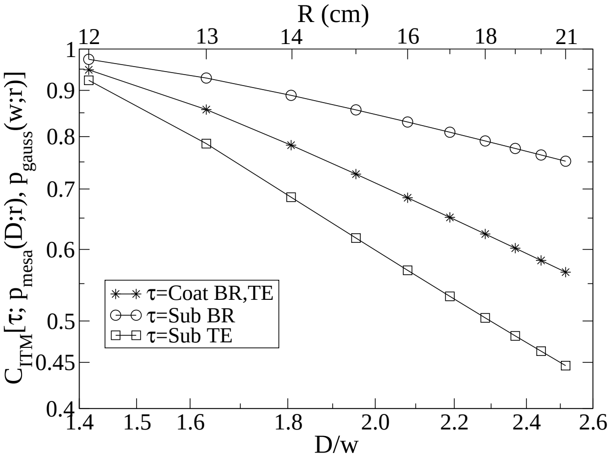

Figure 2.5: The improvement in amplitude sensitivity when mesa beams are used instead of Gaussian beams. More specifically: a log-log plot of $C_{\rm ITM}[\tau; p_{\rm mesa}(D;r), p_{\rm gauss}(w;r)]$ as a function of D/w. For each mirror radius R, w and D are chosen so that the diffraction losses are 1 ppm in the clipping approximation.

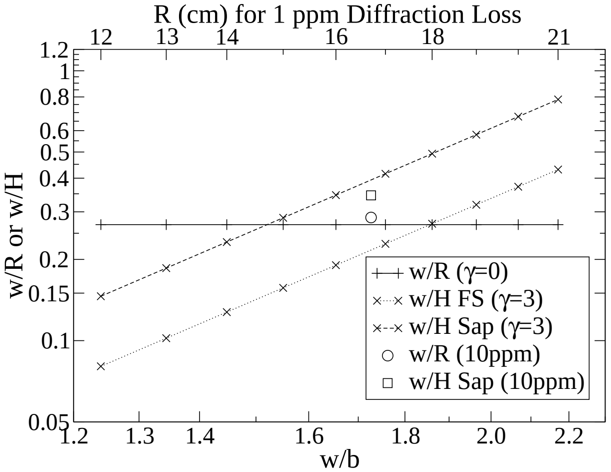

Figure 2.6: How the Gaussian beam width parameter w compares to the mirror radius R and thickness H, when i) the radius R is fixed so the clipping-approximation diffraction loss is 1 ppm (unless a 10 ppm loss is indicated), and ii) the thickness H is then determined by holding the mass at 40 kg, the Advanced-LIGO baseline mirror mass. Each curve is proportional to w^γ. FS and Sap mean fused-silica and sapphire substrates.

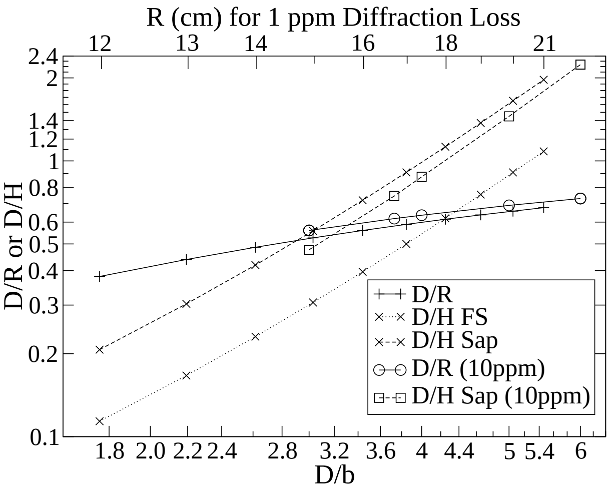

Figure 2.7: How the mesa beam width parameter D compares to the mirror radius R and thickness H, when i) the radius R is fixed so the clipping-approximation diffraction loss is 1 ppm (unless a 10 ppm loss is indicated), and ii) the thickness H is then determined by holding the mass at 40 kg. The mirror radius R for 1 ppm losses is shown on the top axis; the 10 ppm mirror radii are (from left to right) $R^{10\text{ ppm}}$ =13.94 cm, 15.7 cm, 16.37 cm, 18.85 cm, and 21.36 cm. FS and Sap mean fused-silica and sapphire substrates.

2.4, and 2.5]. In other words, for a given diffraction loss, the optimal beam width is simply "as large as possible."

However, this conclusion is only as strong as the ITM approximation. Its validity can be checked by comparing the beam widths to the corresponding mirror dimensions. In our modelling, the mirror radii R are adjusted to maintain a constant clipping-approximation diffraction loss (CADL) [Fig. 2.2], while the thicknesses H is then determined by requiring the mirror mass be 40 kg—the design specification for Advanced LIGO. (Thus H will depend on whether the substrate is fused silica (FS) or sapphire (Sap), since the densities of these materials differ by a factor of about 2.)

As shown in Figs. 2.6 and 2.7, for the sequences of beam widths considered in Sec. 2.4.1, w and D can approach or even exceed H while simultaneously being significant fractions of the R. Consequently, edge effects (finite test-mass effects) may significantly change the sensitivity scalings depicted in Figs. 2.3, 2.4, and 2.5.

To estimate the importance of these edge effects, I compare the results in Secs. 2.4.1.1–2.4.1.3 to the finite-test-mass (FTM) results[6] of Agresti and DeSalvo [10] (all types of thermal noise, 1 ppm CADL) and O'Shaughnessy, Strigin, and Vyatchanin [8] (substrate thermoelastic noise only, 10 ppm

---

[6] The FTM data used here assume that the coating extends all the way to the edge of the substrate face. In Advanced LIGO, the coating radius will actually be several mm smaller than the substrate radius (the baseline substrate radius for Advanced LIGO is 170 mm).

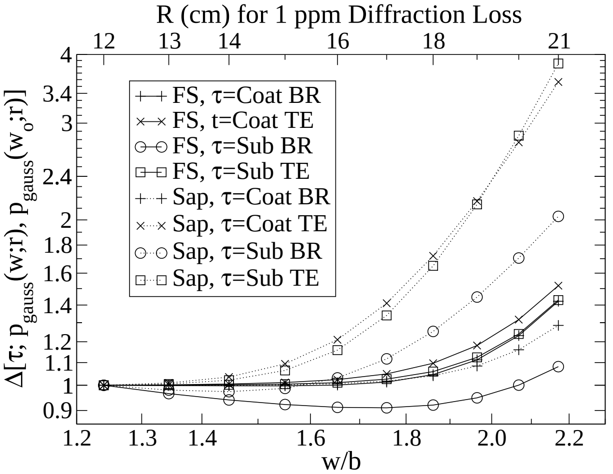

Figure 2.8: A log-log plot of $\Delta[\tau; p_{\rm gauss}(w; r), p_{\rm gauss}(w_o; r)]$. The fractional error of the sensitivity change made by neglecting edge effects is $|1-\Delta|$. Here $w_o/b = 1.24$, which corresponds to $R = 12$ cm and 1 ppm diffraction losses. The FTM values are obtained by taking ratios of the noises calculated by Agresti and DeSalvo (2007). FS and Sap mean fused-silica and sapphire substrates.

CADL). Specifically, from these data I read off the ratio

$$C_{\rm FTM}[\tau; p_u(r), p_k(r)] \equiv \sqrt{\frac{S^{\rm FTM}_{\tau,u}}{S^{\rm FTM}_{\tau,k}}}. \tag{2.46}$$

This change in sensitivity can be compared to $C_{\rm ITM}[\tau; p_k(r), p_u(r)]$, the change in sensitivity obtained by the ITM approximation. Specifically, if

$$\Delta[\tau; p_u(r), p_k(r)] \equiv \frac{C_{\rm FTM}[\tau; p_u(r), p_k(r)]}{C_{\rm ITM}[\tau; p_u(r), p_k(r)]}, \tag{2.47}$$

then $|1-\Delta|$ is the fractional error made by using the ITM approximation to compute $C[\tau; p_u(r), p_k(r)]$.

In the following subsections, I consider the errors $|1-\Delta|$ made [Secs. 2.4.1.1–2.4.1.3] by neglecting FTM effects.

2.4.2.1 Resized Gaussian beam

Fig. 2.8 plots $\Delta[\tau; p_{\rm gauss}(w; r), p_{\rm gauss}(w_o; r)]$ for mirror substrates made of fused silica, the baseline material for Advanced LIGO mirrors [1]. For comparison, the figure also shows the corresponding values of Δ for sapphire substrates.

When the substrate is fused silica, the ITM and FTM scaling laws agree to better than about 10% so long as $R \lesssim 17$ cm, the Advanced-LIGO baseline mirror radius [1]. As R increases beyond about 17 cm, $|1-\Delta|$ for fused silica increases dramatically (to about 50% when $R = 21$ cm), because for such large radii the noise *increases* (e.g. [10, 8]) with R, while the ITM scaling laws predict [Fig. 2.3] that the noise *always decreases* with increasing R.

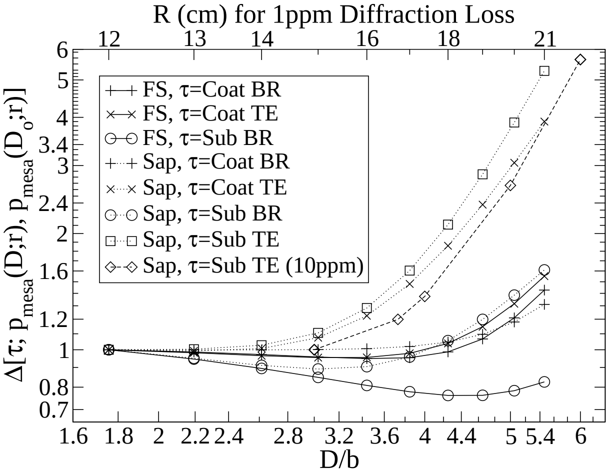

Figure 2.9: A log-log plot of $\Delta[\tau; p_{\rm mesa}(D; r), p_{\rm mesa}(D_o; r)]$. The fractional error of the sensitivity change made by neglecting edge effects is $|1 - \Delta|$. Here the diffraction losses are 1 ppm (unless 10 ppm is indicated), and $D_o/b = 1.76$ ($D_o^{10\ \rm ppm} = 3.00$), which corresponds to a mirror radius $R = 12$ cm ($R^{10\ \rm ppm} = 13.94$ cm). The corresponding mirror radii are given on the top axis (1 ppm losses) and in Fig. 2.7 (10 ppm losses). The FTM values are obtained by taking ratios of the noises calculated by Agresti and DeSalvo (2007), except for the 10 ppm values due to O'Shaughnessy, Strigin, and Vyatchanin (2003). FS and Sap mean fused-silica and sapphire substrates. (The fused-silica substrate thermoelastic noise is negligible; this case is omitted from the figure.)

When the substrate is sapphire, the FTM effects for the thermoelastic noises lead to errors that are comparable to the fused-silica FTM errors. For a mirror radius of[7] $R = 16$ cm, the fractional error $|1 - \Delta|$ for sapphire substrates is about 15% for substrate thermoelastic noise and about 20% for coating thermoelastic noise.

2.4.2.2 Resized mesa beam

The FTM effects in the resized-mesa-beam case are similar to the resized-Gaussian-beam FTM effects. Fig. 2.9 plots $\Delta[\tau; p_{\rm mesa}(D; r), p_{\rm mesa}(D_o; r)]$. When the substrate is fused silica and $R \lesssim 17$ cm, the ITM scaling law errs by less than about 10% for the coating noises and by less than about 25% for the substrate Brownian noise. (The substrate thermoelastic noise is negligible when the substrate is fused silica [10].) Again, the ITM scaling law disagrees more and more strongly as R is increased beyond 17 cm. In this regime, the noise *increases* with R, but the ITM scaling law [Fig. 2.4] predicts that the noise *always decreases* with increasing R.

When the substrate is sapphire, the FTM effects for the thermoelastic noises are comparable to the Brownian-substrate errors for fused silica. When $R = 16$ cm, the FTM effects on the sapphire thermoelastic noises correspond to a fractional error $|1 - \Delta|$ of 20%–30%.

---

[7] When sapphire was the baseline test-mass material for Advanced LIGO (it has since been abandoned in favour of fused silica), the baseline mirror radius was $R = 15.7$ cm [21].

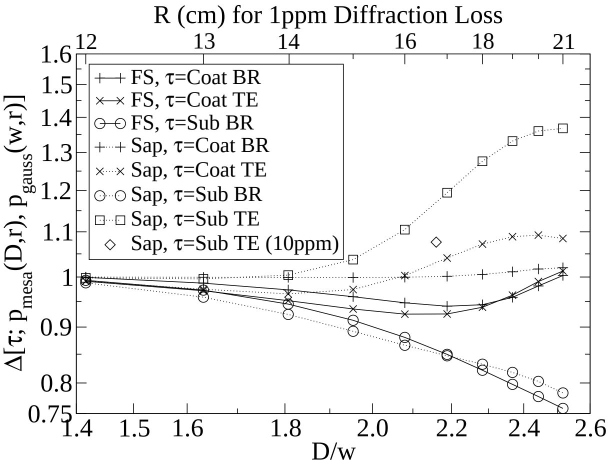

Figure 2.10: A log-log plot of $\Delta[\tau; p_{\rm mesa}(D;r), p_{\rm gauss}(w;r)]$. The beam width parameters w and D are chosen so that the diffraction loss is 1 ppm (unless 10 ppm is indicated). The corresponding mirror width for 1 ppm diffraction losses is shown on the top axis; the 10 ppm point corresponds to a mirror radius of 15.7 cm. The fractional error of the sensitivity change made by neglecting edge effects is $|1-\Delta|$. The FTM values are obtained by taking ratios of the noises calculated by Agresti and DeSalvo (2007), except for the 10 ppm value, which is due to O'Shaughnessy, Strigin, and Vyatchanin (2003). FS and Sap mean fused-silica and sapphire substrates. (The fused-silica substrate thermoelastic noise is negligible; this case is omitted from the figure.)

2.4.2.3 Switching from a Gaussian beam to a mesa beam with the same diffraction loss and mirror radius

The errors due to neglecting FTM effects in the Gaussian-to-mesa case behave qualitatively differently from (and are generally smaller than) the resized-beam errors. Fig. 2.10 plots $\Delta[\tau; p_{\rm mesa}(D;r), p_{\rm gauss}(w;r)]$ for fused silica and sapphire substrates. For both fused-silica and sapphire substrates, the coating sensitivity changes are not strongly sensitive to edge effects; in these cases, $C_{\rm FTM}$ and $C_{\rm ITM}$ differ by less than about 10% even when the beam widths exceed 17 cm (and thus are significant fractions of R and H [c.f. Figs. 2.6 and 2.7]). The substrate sensitivity changes are more sensitive to edge effects, but even then the edge effects remain below about 15%, provided that $R \lesssim 17$ cm for fused-silica substrates and $R \lesssim 16$ cm for sapphire substrates.

2.5 Conclusion

Changing the shape of the laser beam in Advanced LIGO can reduce the thermal noise, which is the limiting noise source at frequencies from 40 Hz to 200 Hz. In the Fourier domain, the relations between the thermal noise and the beam shape for semi-infinite mirrors take the form of simple scaling laws. Moreover, the coating thermal noises obey the same local scaling law. These results enable a straightforward comparison of the thermal noises for two different beam shapes when edge effects are neglected. The scaling laws predict the improvement of mesa-beam sensitivities vs.

Gaussian-beam sensitivities quite well. For 40 kg, fused-silica mirrors the substrate-noise scaling laws agree with the finite-mirror results within approximately 15% for mirror sizes not larger than the Advanced-LIGO baseline size of about 17 cm; the coating-noise scaling laws agree with the finite-mirror predictions to better than about 10%. Therefore, the infinite-test-mass scaling laws may be a very useful tool for estimating optimal beam shapes for Advanced LIGO and other future gravitational-wave interferometers.

2.6 Appendix A: Derivation of equations (2.31) and (2.18)

In this appendix, I derive Eq. (2.31), which I use in the derivation of the scaling law (2.36) for Brownian substrate noise. Then, I deduce Eq. (2.18), which I use in the derivation of the scaling law (2.23) for Brownian coating noise.

First, consider the integral

$$\int_0^\infty \mathrm{d}r r \left[S_{\varphi\varphi}^2 - S_{\varphi\varphi}\left(\theta - S_{zz}\right)\right]. \tag{2.48}$$

Combining Eqs. (2.13a) and (2.13e) gives

$$\theta - S_{zz} = \frac{1}{2\mu}\int_0^\infty \mathrm{d}k \mathrm{e}^{-kz}\tilde{p}(k)\left[\frac{-\mu}{\lambda+\mu} + kz\right] kJ_0(kr). \tag{2.49}$$

Inserting Eqs. (2.49) and (2.13c) into the left-hand side of Eq. (2.48) yields

$$\begin{aligned}&\int_0^\infty \mathrm{d}r r \left[S_{\varphi\varphi}^2 - S_{\varphi\varphi}\left(\theta - S_{zz}\right)\right]\\ &= \frac{1}{4\mu^2}\int_0^\infty \mathrm{d}k \int_0^\infty \mathrm{d}k' \mathrm{e}^{-(k+k')z}\left[\frac{-\mu}{\lambda+\mu} + kz\right]\left[\frac{-\mu}{\lambda+\mu} + k'z\right]\tilde{p}(k)\tilde{p}(k')I,\end{aligned} \tag{2.50}$$

where

$$I = \int_0^\infty \mathrm{d}r \frac{J_1(kr)J_1(k'r)}{r} - k'\int_0^\infty \mathrm{d}r J_1(kr)J_0(k'r). \tag{2.51}$$

Since k and k' are variables of integration, and since aside from I itself, (2.50) is unchanged by letting $k \leftrightarrow k'$, I can be rewritten as

$$I = \int_0^\infty \mathrm{d}r \frac{J_1(kr)J_1(k'r)}{r} - \frac{1}{2}k'\int_0^\infty \mathrm{d}r J_1(kr)J_0(k'r) - \frac{1}{2}k\int_0^\infty \mathrm{d}r J_1(k'r)J_0(kr). \tag{2.52}$$

The integrals in (2.52) are special cases of Eqs. (11.4.33), (11.4.34), and (11.4.42) of [22]:

$$\int_0^\infty \mathrm{d}r \frac{J_1(kr)J_1(k'r)}{r} = \frac{k'}{2k}\eta(k-k') + \frac{k}{2k'}\eta(k'-k), \tag{2.53a}$$

$$\int_0^\infty \mathrm{d}r J_1(kr)J_0(k'r) = \frac{\eta(k-k')}{k}. \tag{2.53b}$$

Here η is the unit step function. Inserting (2.53a) and (2.53b) into (2.52) shows that

$$I = 0 \Rightarrow \int_0^\infty \mathrm{d}r r \left[S_{\varphi\varphi}^2 - S_{\varphi\varphi}\left(\theta - S_{zz}\right)\right] = 0, \tag{2.54}$$

which is Eq. (2.31).

Next, combining Eqs. (2.16a)–(2.16d) shows that

$$S_{\varphi\varphi}^{\mathrm{coat}} = S_{\varphi\varphi}\left|_{z=0}\right. \tag{2.55a}$$

$$\theta^{\mathrm{coat}} - S_{zz}^{\mathrm{coat}} = \left(\theta - S_{zz}\right)\big|_{z=0}. \tag{2.55b}$$

Thus, setting $z = 0$ in (2.54) gives

$$\int_0^\infty \mathrm{d}r r \left[\left(S_{\varphi\varphi}^{\mathrm{coat}}\right)^2 - S_{\varphi\varphi}^{\mathrm{coat}}\left(\theta^{\mathrm{coat}} - S_{zz}^{\mathrm{coat}}\right)\right] = 0, \tag{2.56}$$

which is Eq. (2.18).

2.7 Appendix B: Junction conditions for the stress and strain of a statically deformed, semi-infinite mirror with thin coating

The junction conditions (2.16a)–(2.16d) are listed in Eq. (A4) of [4] along with the statement that for these conditions to hold, the Poisson ratios of the coating and substrate should not be "too different." This restriction is actually unnecessary, provided that the coating is sufficiently thin. One can see this as follows:

Because the coating adheres to the substrate surface, the substrate surface and coating have the same tangential displacement. Continuity of u_r and u_φ immediately implies continuity of S_{rr} and $S_{\varphi\varphi}$. A straightforward pillbox integration of the equilibrium condition $\nabla_j T_{ij} = 0$ then shows that T_{zz} and T_{rz} are also continuous across the junction.

All of the other junction conditions given in Eq. (A.4) of [4] then follow, with one exception: the junction condition on $S_{(rz)}$ should read $\mu^{\mathrm{coat}} S_{(rz)}^{\mathrm{coat}} = \mu^{\mathrm{sub}} S_{(rz)}^{\mathrm{sub}}$, not $S_{(rz)}^{\mathrm{coat}} = S_{(rz)}^{\mathrm{sub}}$. But since $T_{rz} = 0$

on the coating surface (and thus also to high accuracy throughout the thin coating), this error is irrelevant; the correct junction condition is simply $S^{\rm coat}_{(rz)} = S^{\rm sub}_{(rz)} = 0$.

2.8 Bibliography

[1] Advanced LIGO: context and summary (online document accessed 14 September, 2006), URL `http://www.ligo.caltech.edu/advLIGO/scripts/summary.shtml`.

[2] J. Agresti, Researches on non-standard optics for advanced G.W. interferometers (internal LIGO document LIGO-T040225-00-R) (2005), URL `http://www.ligo.caltech.edu/docs/T/T040225-00.pdf`.

[3] Y. T. Liu and K. S. Thorne, Phys. Rev. D **62**, 122002 (2000).

[4] G. M. Harry et al., Class. Quantum Grav. **19**, 897 (2002).

[5] V. B. Braginsky and S. P. Vyatchanin, Phys. Lett. A **312**, 244 (2003).

[6] E. d'Ambrosio, R. O'Shaughnessy, and K. S. Thorne, Beam reshaping to reduce thermal noise (internal LIGO document G000223-00-D) (2000), URL `http://www.ligo.caltech.edu/docs/G/G000223-00.pdf`.

[7] E. D'Ambrosio et al., Phys. Rev. D. (submitted), (2004), `gr-qc/0409075`.

[8] R. O'Shaughnessy, S. Strigin, and S. Vyatchanin, Phys. Rev. D (submitted), (2003), `gr-qc/0409050`.

[9] J. Agresti and R. DeSalvo, flat beam profile to depress thermal noise (internal LIGO document G050041-00-Z) (2005), URL `http://www.ligo.caltech.edu/docs/G/G050041-00`.

[10] J. Agresti and R. DeSalvo (2007), (document in preparation).

[11] J. Agresti et al., J. Phys: Conference Series **32**, 301 (2006).

[12] M. Tarallo et al., *Generation of a flat-top laser beam for gravitational-wave detectors by means of a non-spherical fabry-perot resonator,* Applied Optics (submitted) (2007), URL `http://www.ligo.caltech.edu/~jmiller/Documents/Papers/MHpaper.pdf`.

[13] Y. Levin, Phys Rev. D **57**, 659 (1997).

[14] M. M. Fejer et al., Phys. Rev. D **70**, 082003 (2004).

[15] R. O'Shaughnessy (2006), `gr-qc/0607035v1`.

[16] R. O'Shaughnessy, Class. Quantum Grav. **23**, 7627 (2006).

[17] S. Vyatchanin, FDT approach calculations of Brownian noise in thin layer (internal LIGO document T040242-00Z) (2004), URL `http://www.ligo.caltech.edu/docs/T/T040242-00.pdf`.

[18] J.-Y. Vinet, Class. Quantum Grav. **22**, 1395 (2005).

[19] F. Bondu, P. Hello, and J.-Y. Vinet, Phys. Lett. A **246**, 227 (1998).

[20] A. E. Siegman, Opt. Lett. **1**, 13 (1977).

[21] P. Fritschel, Advanced LIGO systems design (internal LIGO document T010075-00-D) (2001), URL `http://www.ligo.caltech.edu/docs/T/T010075-00.pdf`.

[22] M. Abramowitz and I. A. Stegun, Eds., *Handbook of Mathematical Functions* (Dover Publications, New York, 1964).

Chapter 3

Tidal coupling of a Schwarzschild black hole and circularly orbiting moon

We describe the possibility of using LISA's gravitational-wave observations to study, with high precision, the response of a massive central body (e.g., a black hole or a soliton star) to the tidal gravitational pull of an orbiting, compact, small-mass object (a white dwarf, neutron star, or small-mass black hole). Motivated by this LISA application, we use first-order perturbation theory to study tidal coupling for a special, idealized case: a Schwarzschild black hole of mass M, tidally perturbed by a "moon" with mass $\mu \ll M$ in a circular orbit at a radius $b \gg M$ with orbital angular velocity Ω. We investigate the details of how the tidal deformation of the hole gives rise to an induced quadrupole moment $\mathscr{I}_{ij}$ in the hole's external gravitational field at large radii, including the vicinity of the moon. In the limit that the moon is static, we find, in Schwarzschild coordinates and Regge-Wheeler gauge, the surprising result that *there is no induced quadrupole moment*. We show that this conclusion is gauge dependent and that *the static, induced quadrupole moment for a black hole is inherently ambiguous*, and we contrast this with an earlier result of Suen, which gave, in a very different gauge, a nonzero static-induced quadrupole moment with a sign opposite to what one would get for a fluid central body. For the orbiting moon and the central Schwarzschild hole, we find (in agreement with a recent result of Poisson) a time-varying induced quadrupole moment that is proportional to the time derivative of the moon's tidal field, $\mathscr{I}_{ij} = (32/45)M^6\dot{\mathcal{E}}_{ij}$ and that therefore is out of phase with the tidal field by a spatial angle $\pi/4$ and by a temporal phase shift $\pi/2$. This induced quadrupole moment produces a gravitational force on the moon that reduces its orbital energy and angular momentum at the same rate as the moon's tidal field sends energy and angular momentum into the hole's horizon. As a partial analog of a result derived long ago by Hartle for a spinning hole and a static distant companion, we show that the orbiting moon's tidal field induces a tidal bulge on the hole's horizon, and that the rate of change of the horizon shape (i.e., the horizon shear) *leads* the perturbing tidal field at the horizon by an angle $4M\Omega$. We prefer to avoid introducing an ingoing null geodesic, as Hartle did in his definition of the phase shift, because the moon is in the central body's near zone ($b \ll 1/\Omega$) and thus should interact with the horizon instantaneously, not causally. We discuss the implications of these results for LISA's future observations of tidal coupling, including the inappropriateness of using the concepts of *tidal polarizability* and *tidal lag or lead angle*, for the massive central body, when discussing LISA's observations.

Originally published as H. Fang and G. Lovelace, Phys. Rev. D. **72** (2005) 124016.

3.1 Introduction and summary

3.1.1 Motivations

One of the primary scientific requirements for LISA (the Laser Interferometer Space Antenna) is to map, in exquisite detail, the spacetime geometries of massive black holes (and, if they exist, other massive, compact bodies) by using the gravitational waves emitted by inspiraling white dwarfs, neutron stars, and small-mass black holes. This emission process has come to be called "Extreme Mass Ratio Inspiral" (EMRI, pronounced emm-ree). The possibility of making such maps from EMRI waves was discussed by Thorne in the early 1990s (e.g., in [1, 2]). In 1995 Ryan [3] laid the first detailed foundation for such mapping: he showed that, when the massive, central body is general-relativistic, axisymmetric, and reflection-symmetric, and when the orbiting object is in a near-equatorial, near-circular orbit in the vacuum region surrounding the body, the full details of the central body's metric are encoded in (i) the phase evolution of the waves and also in (ii) the evolution of the frequencies (or phases) of wave modulation produced by orbital precession. Phinney [4] has given the name "bothrodesy" to the mapping of a black hole's metric via EMRI waves, and bothrodesy has been identified, by the LISA International Science Team (LIST), as one of the prime goals for LISA [5]. The initial phase of scoping out LISA's data analysis challenges for EMRI waves is now underway [6, 7].

Ryan's proof that the EMRI waves carry a map of the central body's metric ignored completely the influence of tidal coupling between the central body and the orbiting object. Finn and Thorne [8] have shown that, for values of the body and object masses in the range relevant to LISA, the tidal coupling can have an influence as large as a few percent on the evolution of the waves' inspiral phase—

a phase that should be measurable to a fraction of a cycle out of tens or hundreds of thousands of cycles. Thus, the influence of the tidal coupling may be measurable with rather high precision. Because, in Ryan's analysis, the map is encoded redundantly in the EMRI waves' inspiral phase and in their modulations, it is reasonable to hope that the tidal coupling will break that redundancy in such a manner as to permit extraction of both the map and details of the central body's response to the tidal gravitational pull of the orbiting object [9].

Thorne [10] has argued that if we are to keep an open mind about the physical nature of the central body from the outset [e.g., if we are to allow for the possibility that it is a boson star (e.g., [11, 12]) or a soliton star (e.g., [13]) rather than a black hole], then we must describe the tidal coupling in a manner that can encompass all possible types of central bodies—a body-independent manner.

In the case of the earth and moon, the tidal coupling is normally described in terms of the rise and fall of the earth's surface or ocean's surface, and in terms of energy dissipation in the earth's oceans. Noticeably different from this, the tidal coupling in the case of a black hole has always, until now, been described in terms of the influence of the orbiting object's gravitational field on the hole's horizon—the perturbation of the horizon's 2-metric (e.g., [14, 15]), or the conversion of the tidal field into gravitational radiation at the horizon by gravitational blue-shifting and the energy and angular momentum carried inward by those waves (e.g., [16]).

One tidal feature in common between a black hole, the earth, a boson or soliton star, and all other conceivable central bodies, is the body's tidally-induced multipole moments and multipolar gravitational fields. It is these induced fields, acting back on the orbiting object, that change the object's orbital energy and angular momentum, secularly change its orbit, and thereby alter the emitted gravitational waves. For this reason, Thorne [10] has proposed that we adopt these induced multipole fields or moments as our body-independent description of tidal coupling when analyzing LISA data.

As a first step in exploring Thorne's proposal, we compute in this paper the tidally induced quadrupole moment and its back reaction on the orbiting object in the special case where the central body is a Schwarzschild black hole, and the object is a distant, circularly orbiting moon.

3.1.2 Framework and results

Consider a moon of mass μ orbiting around a massive central body at a large distance. When the central body is a planet [17] (see Sec. III of [15] for a review), the external tidal field produced by the moon, denoted by $\mathcal{E}_{ij}^{\rm ext}$, raises a tide on the central body and induces a quadrupole moment $\mathscr{I}_{ij}^{\rm ind}$ that is proportional to $\mathcal{E}_{ij}^{\rm ext}$. The proportionality constant is the body's polarizability. Because of viscous dissipation, the induced quadrupole moment $\mathscr{I}_{ij}^{\rm ind}$ will be slightly out of phase with $\mathcal{E}_{ij}^{\rm ext}$; it will have a small phase lag with respect to the applied field. This phase lag is generally referred to as the tidal lag angle, and can be defined equivalently as the ratio of the tangential and radial component of the tidally-induced force acting back on the moon. One objective of this paper is to explore whether this type of characterization via polarizability and lag angle is also reasonable when the central body is a black hole.

To explore this, we study a model problem where the moon is orbiting circularly around a massive Schwarzschild black hole of mass M ($\gg \mu$) at large distance b ($\gg M$). We assume the separation b is large enough that there exists an intermediate region between the hole and moon where (i) gravity is weak so space is nearly flat; (ii) the moon's tidal field does not vary appreciably. This region is referred to as the black hole's local asymptotic rest frame (LARF) [18]. Because the spacetime is nearly flat, one can write down the full tidal field in the LARF (in Cartesian coordinates) to linear order in each multipole moment as [19]

$$\begin{aligned}\mathcal{E}_{ij} \equiv R_{0i0j} &= -\sum_{\ell=0}^{\infty} \frac{(-1)^\ell}{\ell!} \mathscr{I}_{A_\ell} \left(\frac{1}{r}\right)_{,ijA_\ell} \\ &\quad - \sum_{\ell=2}^{\infty} \frac{(2\ell-1)!!}{(\ell-2)!} \mathscr{Q}_{ijA_{\ell-2}} X_{A_{\ell-2}}. \end{aligned} \tag{3.1}$$

Here $\mathscr{I}_{A_\ell}$ and $\mathscr{Q}_{A_\ell}$ are the ℓth internal and external moments; they are symmetric and trace free (STF) in their tensor indices $A_\ell \equiv a_1...a_\ell$ [20]. The "internal moments" $\mathscr{I}_{A_\ell}$ characterize the central body, while the "external moments" $\mathscr{Q}_{A_\ell}$ characterize the gravitational fields of distant sources that perturb the central body. In our problem, the tidal field $\mathcal{E}^{\rm ext}_{ij}$ is physically the same as the external quadrupole moment $\mathscr{Q}_{ij}$; they differ only by a constant scaling factor, $\mathcal{E}_{ij} = -(1/3)\mathscr{Q}_{ij}$. The internal quadrupole moment is induced by the applied tidal field and characterizes the tidal deformation of the central body.

Eq. (3.1) is the gravitational analogy to the multipole expansion of an electromagnetic field. It will be sufficiently accurate for our purpose, since we shall compute the nonspherical parts of the Riemann curvature tensor by solving the linearized Einstein field equations. It will be shown in Sec. 3.2 that only multipole moments with $\ell = 0, 2$ are relevant to our problem. Dropping all other terms in Eq. (3.1) and contracting with the unit spatial vector yields

$$\mathcal{E}_{ij} n^i n^j = -\frac{2M}{r^3} + \mathcal{E}^{\rm ext}_{ij} n^i n^j - \frac{18 \mathscr{I}^{\rm ind}_{ij} n^i n^j}{r^5}, \tag{3.2}$$

where we have identified $\mathscr{I}$ in Eq. (3.1) as the total mass of the black hole and substituted the external tidal field $\mathcal{E}^{\rm ext}_{ij}$ for $\mathscr{Q}_{ij}$. In the last term, $\mathscr{I}^{\rm ind}_{ij}$ represents the quadrupole moment induced on the black hole by the external tidal field.

In Secs. 3.3 and 3.4.1 of this paper we compute the induced quadrupole moment in Regge-Wheeler gauge, obtaining

$$\mathscr{I}_{ij}^{\rm ind} = \frac{32}{45} M^6 \dot{\mathcal{E}}_{ij}^{\rm ext}. \tag{3.3}$$

The same result was recently derived by Poisson from calculating the averaged rate of change of mass and angular momentum of the perturbed black hole [21]. Note that $\mathscr{I}_{ij}^{\rm ind}$ is proportional to the time derivative of $\mathcal{E}_{ij}^{\rm ext}$ (a time derivative caused by the moon's motion) and is therefore completely out of phase with the external tidal field (by 90 degrees in time and 45 degrees in space). As we will show in Sec. 3.5, this out-of-phase induced moment is gauge invariant and is responsible for the torque that changes the orbital energy and angular momentum. Thus it is also responsible for the tidally-induced portion of the orbital evolution and the phase evolution of the gravitational waves.

The piece of the induced quadrupole moment that is proportional to and in-phase with the applied tidal field is ambiguous (in a sense that we shall discuss in Sec. 3.4.2); in Schwarzschild coordinates and Regge-Wheeler gauge, it *vanishes.* If there had been an unambiguous piece of $\mathscr{I}_{ij}^{\rm ind}$ in phase with $\mathcal{E}_{ij}^{\rm ext}$, then this in-phase piece would have defined a polarizability, and the ratio of out-of-phase piece to the in-phase piece would have been, in a certain well-defined sense, the small tidal lag angle. Thus, our result can be regarded as saying that both the polarizability and the lag angle of a black hole are ambiguous (in the sense discussed in Sec. 3.4.2).

Although we find that the tidal lag angle in the LARF, in the case of a Schwarzschild black hole, is ambiguous, we can still define and calculate an angular tidal shift on the horizon (as opposed to in the LARF or out at the moon). We study this horizon phase shift in Sec. 3.5. Hartle [15] has calculated[1] the tidal lag angle for the problem of a bulge raised on *slowly rotating* hole's horizon by a *stationary moon*, and he has shown it to be *negative*: the horizon's tidal bulge *leads* the applied tidal field due to the horizon's teleological definition (i.e., a definition in terms of the future fate of null rays). As in Hartle's case, we can compare the phase of the shape of our *nonrotating* horizon to our *moving* moon's position by mapping the moon to the horizon with an ingoing, zero-angular momentum, null geodesic. In Sec. 3.5, we find that this prescription leads to a *lead* angle between the moon and the horizon

$$\delta_{\text{null map}} = \frac{8}{3} M\Omega + \Omega b^*, \tag{3.4}$$

where Ω is the orbital angular frequency of the moon and b^* is the moon's tortoise coordinate $b^* \equiv b + 2M \log(b/2M - 1)$.

For comparison, Hartle's result [15] for the tidal lead angle in the case of the rotating hole and distant, stationary moon in the equatorial plane, is (after correcting a sign error, as discussed in footnote 6)

$$\delta^{\rm H}_{\text{null map}} = \frac{2a}{3M} + \frac{a}{b} = \frac{8}{3} M\Omega_H + 4\frac{M^2\Omega_H}{b}, \tag{3.5}$$

---

[1] We review the principal results of Hartle's investigation in Sec. 3.5.2.1.

Here a is the hole's specific angular momentum, and Ω_H is the horizon angular velocity. The radius of the moon's position b is sufficiently large that the moon is essentially stationary. Throughout this paper, we use the superscript "H" to indicate results corresponding to Hartle's system, i.e., to a system with a stationary moon and rotating horizon. Other results (without the subscript "H") correspond to our system of a distant moon, orbiting at frequency Ω, which perturbs a Schwarzschild black hole).

Our result (3.4) differs from Hartle's (3.5)—even though we initially expected that the tidal phase shift should depend only on the difference in angular velocities of the applied tidal field and the horizon generators, so the results would be the same. The terms that differ arise from the particular choice to map the moon to the horizon using an ingoing, zero-angular momentum null ray.

We prefer an alternative definition of the tidal lead angle, one that is independent of b^*; we prefer to define the tidal phase shift as the angle between the perturbing tidal field at the horizon and the shear (which is the rate of change of the shape) of the horizon [22]. This definition avoids introducing null connections between the moon (which, at radius $b \ll \Omega^{-1}$, is in the near zone) and the horizon. Using this definition, we find that the shear of the central hole *leads* the perturbing tidal field at the horizon by an angle

$$\delta_{\text{Horizon}} = \delta^{\text{H}}_{\text{Horizon}} = 4M\Omega. \tag{3.6}$$

The tidal lead angle is the same whether one considers a stationary moon perturbing a rotating hole or an orbiting moon perturbing a non-rotating hole.

The rest of paper is organized as follows. In Sec. 3.2, we decompose the applied tidal field in the LARF into a time-dependent part and a static part. In Sec. 3.3 we analyze fully the time-dependent part and deduce the dynamical part of the induced quadrupole moment [Eq. (3.24)]. In Sec. 3.4, we solve for the static perturbation and discuss the ambiguity in defining the static part of the induced quadrupole moment. In Sec. 3.5, we study the phase shift between the deformation of the horizon and the applied tidal and compare the result with the phase shift as defined by Hartle. A brief conclusion is made in Sec. 3.6. Throughout the paper, we use geometrized units with $G = c = 1$.

3.2 Problem setup

We study small perturbations of a non-spinning black hole caused by an orbiting moon. The unperturbed background metric is the Schwarzschild metric:

$$ds^2 = -\left(1 - \frac{2M}{r}\right)dt^2 + \frac{dr^2}{1 - 2M/r} + r^2(d\theta^2 + \sin^2\theta d\phi^2), \tag{3.7}$$

where M is the mass of the central hole. At large radii (i.e., in the LARF), we will study the perturbations in a notation that treats the Schwarzschild coordinates (r, θ, ϕ) as though they were flat-space spherical coordinates. These coordinates are related to the Cartesian coordinates $(x, y, z) = (x^1, x^2, x^3)$ by

$$(x^1, x^2, x^3) = r(\sin\theta\cos\phi, \sin\theta\sin\phi, \cos\theta).$$

We will denote the radial vector with length r by $\mathbf{x}$, the unit radial vector by $\mathbf{n}$, and their components by x^j and n^j, respectively.

Let a moon of mass μ move along a circular orbit with radius b in the equatorial plane ($b \gg M \gg \mu$). The moon's position is specified by

$$\mathbf{x}^{\mathrm{s}} = b\ \mathbf{n}^{\mathrm{s}} = b\ (\cos\Omega t, \sin\Omega t, 0), \tag{3.8}$$

where the superscript "s" stands for the "source" of the perturbation and $\Omega = \sqrt{M/b^3}$ is the moon's orbital angular frequency, satisfying $\Omega b \ll 1$. The moon's tidal field $\mathcal{E}^{\mathrm{ext}}_{ij}$ is the double gradient of the moon's Newtonian gravitational potential. Its value in the LARF (at $r \ll b$ but $r \gg M$) is well approximated by

$$\begin{aligned}\mathcal{E}^{\mathrm{ext}}_{ij} &= -\left.\left(\frac{\mu}{|\mathbf{x}-\mathbf{x}^{\mathrm{s}}|}\right)_{,ij}\right|_{r=0} \\ &= \frac{\mu}{b^3}\left(\delta_{ij} - 3n^{\mathrm{s}}_i n^{\mathrm{s}}_j\right).\end{aligned} \tag{3.9}$$

Note that although the applied tidal field is defined in the LARF, the induced quadrupolar field $\mathscr{I}^{\mathrm{ind}}_{ij}$ of greatest interest is not in the LARF, but further out in the vicinity of the moon's orbit, where it interacts with the moon.

The tidal field (3.9) can be decomposed into spherical, harmonic modes [23]. The result of the decomposition is

$$\begin{aligned}\mathcal{E}^{\mathrm{ext}}_{ij} &= \frac{\mu}{b^3}\sqrt{\frac{6\pi}{5}}\left(\sqrt{\frac{2}{3}}\mathscr{Y}^{20}_{ij} - \mathscr{Y}^{22}_{ij}e^{-i\omega t} - \mathscr{Y}^{2-2}_{ij}e^{i\omega t}\right) \\ &\equiv \mathcal{E}^{\mathrm{ext},20}_{ij} + \mathcal{E}^{\mathrm{ext},22}_{ij} + \mathcal{E}^{\mathrm{ext},2-2}_{ij}\end{aligned} \tag{3.10}$$

with $\omega \equiv 2\Omega$ and $\mathcal{E}^{\mathrm{ext},2m}_{ij}$ ($m = 0, \pm 2$) equal to the corresponding $\mathscr{Y}^{2m}_{ij}$ term. Here the $\mathscr{Y}^{2m}_{ij}$ are position-independent, rank-2, symmetric trace-free (STF) tensors defined in Eqs. (3.68)–(3.69) and are related to the familiar $\ell = 2$ spherical harmonics $Y^{2m}(\theta, \phi)$ by Eq. (3.67). (See Eqs. (2.7)–(2.14) of [23] for the general mapping between order ℓ spherical harmonics and rank-ℓ STF tensors). The explicit values of the tidal field components are

$$\mathcal{E}_{ij}^{\mathrm{ext},20} = -\frac{\mu}{2b^3}\begin{pmatrix} 1 & 0 & 0 \\ 0 & 1 & 0 \\ 0 & 0 & -2 \end{pmatrix}, \tag{3.11a}$$

$$\mathcal{E}_{ij}^{\mathrm{ext},2\pm2} = -\frac{3\mu}{4b^3}\begin{pmatrix} 1 & \pm i & 0 \\ \pm i & -1 & 0 \\ 0 & 0 & 0 \end{pmatrix} e^{\mp i\omega t}. \tag{3.11b}$$

The tidal field $\mathcal{E}_{ij}^{\mathrm{ext}}$ [Eq. (3.10)] is the source of perturbations of the central hole; it is an even-parity $\ell = 2$ external tidal field. We shall therefore perform our calculation in the even-parity Regge-Wheeler gauge, mode by mode ($\ell = 2, m = 0, \pm2$). The tidal field $\mathcal{E}_{ij}^{\mathrm{ext}}$ also sets the outer boundary condition for the problem: the $O(r^0)$ terms in the perturbed tidal field $\mathcal{E}_{ij}$ must go to $\mathcal{E}_{ij}^{\mathrm{ext}}$ in the LARF [Eq. (3.2)].

The inner boundary condition is set differently, depending on whether the perturbations are static or time-dependent. For the static perturbations generated by $\mathcal{E}_{ij}^{20}$, we impose a "regularity boundary condition": the perturbations must be physically finite at $r = 2M$. For the time-dependent perturbations generated by $\mathcal{E}_{ij}^{\mathrm{ext},2\pm2}$, we impose the "ingoing-wave boundary condition": the perturbations have the asymptotic behavior $\sim e^{\mp i\omega r^*}$ when approaching the horizon. Here r^* is the tortoise coordinate $r^* \equiv r + 2M\log(r/2M - 1)$.

3.3 Time-dependent part of the perturbation

3.3.1 The perturbed metric

We will specialize to $(\ell, m) = (2, 2)$ in solving for the time-dependent part of the metric perturbation. The $(\ell, m) = (2, -2)$ results can be obtained by complex conjugating the $(2, 2)$ results. For briefness, a superscript "22" will not be added to quantities calculated in this harmonic mode in this section, unless a distinction is needed. Throughout this section, we refer to Appendix 3.8 for details of the perturbation calculation.

In the standard Regge-Wheeler gauge, the $(\ell, m) = (2, 2)$ time-dependent perturbations take the form [24]

$$\begin{aligned} h_{ab}^{(22)} &= Y^{22}(\theta,\phi)e^{-i\omega t} \\ &\times \begin{vmatrix} H(1-\frac{2M}{r}) & H_1 & 0 & 0 \\ H_1 & H(1-\frac{2M}{r})^{-1} & 0 & 0 \\ 0 & 0 & r^2K & 0 \\ 0 & 0 & 0 & r^2K\sin^2\theta \end{vmatrix} . \end{aligned} \tag{3.12}$$

Here H, H_1 and K are functions of r alone. These radial functions are solutions of the perturbed Einstein equations; they can be constructed from the Zerilli function $\mathbb{Z}(r)$ [25], which satisfies a second-order ordinary differential equation [Eq. (3.73)]. Specifically, H_1, K, and H are given in terms of $\mathbb{Z}(r)$ by Eqs. (3.70)–(3.72). Instead of solving for $\mathbb{Z}$(r) directly, one may obtain the Zerilli function from its odd-parity correspondent, the Regge-Wheeler function $\mathbb{X}(r)$, which obeys a simpler differential equation [24, 26] that is easier to solve [Eq. (3.74)]:

$$\left[\frac{d^2}{dr^{*2}}+\omega^2-\Big(1-\frac{2M}{r}\Big)\Big(\frac{\ell(\ell+1)}{r^2}-\frac{6M}{r^3}\Big)\right]\mathbb{X}(r)=0,$$

where $d/dr^* = (1-2M/r)d/dr$. The Zerilli function $\mathbb{Z}(r)$ is expressed in terms of $\mathbb{X}(r)$ by Eq. (3.75). Thus, the metric perturbation is determined by the single radial function $\mathbb{X}(r)$, by way of Eq. (3.75) to get $\mathbb{Z}(r)$ and then Eqs. (3.70)–(3.72) to get H_1, K, and H.

The analytic solution for $\mathbb{X}$(r) with the ingoing-wave boundary condition at horizon was derived by Poisson and Sasaki [27]. Their solution, X^H in their notation and for the limiting case $\omega r \ll 1$, is what we have used in our analysis. With our slow motion assumption $\Omega b \ll 1$, $X^H(\omega r \ll 1)$ will be sufficient to cover the region inside the moon's orbit—including the LARF, where we read out the induced quadrupole moment. Following Poisson and Sasaki's notation, we define the dimensionless quantity

$$\varepsilon \equiv 2M\omega. \tag{3.13}$$

We then combine Eqs. (3.4), (3.11), and (3.12) of [27] to obtain

$$\begin{aligned} X^H(\omega r \ll 1) &= \mathcal{A}\left(\frac{r}{2M}\right)^3 e^{i\omega(r-2M)} \\ &\times \; F(c_1,c_2;c_3;1-\frac{r}{2M})e^{-i\omega r^*}, \end{aligned} \tag{3.14}$$

where $\mathcal{A}$ is an overall scaling factor that did not appear in [27] but will be determined by the outer boundary condition in our problem; F is the hypergeometric function with parameters [Eq. (3.11) of [27] with $\ell = 2$]

$$\begin{aligned} c_1 &= -i\varepsilon + O(\varepsilon^2), \\ c_2 &= 5 - i\varepsilon + O(\varepsilon^2), \\ c_3 &= 1 - 2i\varepsilon. \end{aligned} \tag{3.15}$$

Note that expression (3.14) for X^H is only accurate to first order in ε. We then expand Eq. (3.14) in large r and keep terms to first order in ε

$$X^H = \mathcal{A}\left[\left(1 + \frac{13}{12}i\varepsilon\right)\tilde{r}^3 + \sum_{n=5}^{\infty} \frac{i\varepsilon}{n\tilde{r}^{n-3}} + O(\varepsilon^2)\right], \tag{3.16}$$

where $\tilde{r} \equiv r/2M$ is the dimensionless radius. Next, we use Eq. (3.75) to get $\mathbb{Z}(r)$. Then the perturbed metric components can be constructed using Eqs. (3.70)–(3.72). In the following, all quantities will be calculated up to first order in ε and we will suppress "$O(\varepsilon^2)$" in our expressions.

3.3.2 Induced quadrupole moment in the LARF

Once the perturbed metric is known, it is straightforward to calculate the full Riemann tensor and extract from it the first-order tidal field in the LARF:

$$\mathcal{E}_{ij}^{(1)} \quad \equiv \quad R_{0i0j}^{(1)} = R_{0i0j} - R_{0i0j}^{(0)}, \tag{3.17}$$

where a superscript of "(0)" or "(1)" indicates the quantity is of zeroth or first order in the perturbation. In our calculation, we found it convenient to look at the $0r0r$ component of the first-order Riemann tensor in the LARF, since

$$R_{0r0r}^{(1)} = R_{0i0j}^{(1)} n_i n_j = \mathcal{E}_{ij}^{(1)} n_i n_j. \tag{3.18}$$

From this equation we can read off $\mathcal{E}_{ij}^{(1)} = R_{0i0j}^{(1)}$, the first-order tidal field in Cartesian coordinates in the LARF, from the Riemann tensor in Schwarzschild coordinates. By the procedure outlined in this paragraph we have deduced the following $(\ell, m) = (2, 2)$ part of $\mathcal{E}_{ij}^{(1)}$ in the LARF:

$$\mathcal{E}_{ij}^{(1),22} = -\frac{3\mathcal{A}}{4M^3}\left[1 + \frac{4}{3}i\varepsilon + \sum_{n=5}^{\infty} \frac{i\varepsilon}{n\tilde{r}^n}\right] \mathscr{Y}_{ij}^{22} e^{-i\omega t}. \tag{3.19}$$

The outer boundary condition states that the $O(r^0)$ [i.e., $O(\tilde{r}^0)$] term of $\mathcal{E}_{ij}^{(1),22}$ must equal $\mathcal{E}_{ij}^{\text{ext},22}$

[Eq. (3.11b)]. This determines the scaling factor to be

$$\mathcal{A} = \frac{4\mu M^3}{b^3}\sqrt{\frac{2\pi}{15}}\left(1 - \frac{4}{3}i\varepsilon\right). \tag{3.20}$$

Inserting Eq. (3.20) into Eq. (3.19), we can write $\mathcal{E}_{ij}^{(1),22}$ as

$$\mathcal{E}_{ij}^{(1),22} = \mathcal{E}_{ij}^{\mathrm{ext},22} - \frac{\mu}{b^3}\sqrt{\frac{6\pi}{5}}\sum_{n=5}^{\infty}\frac{i\varepsilon}{n\tilde{r}^n}\mathscr{Y}_{ij}^{22}e^{-i\omega t}. \tag{3.21}$$

Here the $O(1/\tilde{r}^5)$ term, by Eq. (3.2), contains the induced quadrupole moment. The $O(1/\tilde{r}^6)$ and higher terms are proportional to the $O(1/\tilde{r}^5)$ term and contain no new information; they represent the non-linear coupling between the induced quadrupole and the black hole's monopole moment.

Comparing the $O(1/\tilde{r}^5)$ term in Eq. (3.2) and the $O(1/r^5)$ term in Eq. (3.21), we find that

$$\mathscr{I}_{ij}^{22} = \frac{32}{45}M^6\dot{\mathcal{E}}_{ij}^{\mathrm{ext},22}. \tag{3.22}$$

Complex conjugating this equation yields the $(\ell, m) = (2, -2)$ part of the induced quadrupole moment:

$$\mathscr{I}_{ij}^{2-2} = \frac{32}{45}M^6\dot{\mathcal{E}}_{ij}^{\mathrm{ext},2-2}. \tag{3.23}$$

Thus, the time dependent part, i.e., the dynamical part (DP), of the induced quadrupole moment is given by

$$\mathscr{I}_{ij}^{\mathrm{ind,\ DP}} = \frac{32}{45}M^6\left(\dot{\mathcal{E}}_{ij}^{\mathrm{ext},22} + \dot{\mathcal{E}}_{ij}^{\mathrm{ext},2-2}\right) = \frac{32}{45}M^6\dot{\mathcal{E}}_{ij}^{\mathrm{ext}}. \tag{3.24}$$

This agrees with the result recently obtained by Poisson [21] by a very different method. Note that the induced quadrupole moment is proportional to the time derivative of the applied tidal field. Hence the induced quadrupole moment and the applied tidal field are completely out of phase with each other ($\pi/4$ phase shift in space, $\pi/2$ in time). This leads to a dissipative force acting back on the moon.

From the induced quadrupole moment (3.24), we define a corresponding Newtonian potential in the LARF and out to the moon's orbit:

$$\Phi = -\frac{3}{2}\mathscr{I}_{ij}^{\mathrm{ind,\ DP}}\frac{n^i n^j}{r^3}. \tag{3.25}$$

Then the force acting back on the moon can be found by evaluating the gradient of Φ at the moon's position:

$$\mathbf{F} = -\nabla\Phi|_{\mathbf{x}^{\mathrm{s}}} = -\frac{32}{5}\left(\frac{\mu}{b}\right)^2\left(\frac{M}{b}\right)^{13/2}\mathbf{e}_\phi. \tag{3.26}$$

Eq. (3.26) shows that the force is tangential and opposite to the moon's motion. The energy loss from the moon's orbital motion is then

$$\dot{E} = -\mathbf{F} \cdot \mathbf{v} = \frac{32}{5} M^4 \mu^2 \Omega^6, \tag{3.27}$$

where $\mathbf{v} = \Omega b \mathbf{e}_\phi$. It is straightforward to show that there is also an angular momentum loss of magnitude $\dot{E}/\Omega$. Eq. (3.27) agrees with Poisson and Sasaki's calculation of the rate at which the perturbation carries energy into the black hole's horizon at the leading post-Newtonian order [27].

3.4 The static, axisymmetric part of the perturbation

3.4.1 Static-induced quadrupole moment

We now specialize to the even-parity, static part of the moon's perturbation: $(\ell, m) = (2, 0)$. The Regge-Wheeler metric for this type of perturbation has the form [24]

$$\begin{aligned} h_{ab}^{(20)} = \mathrm{Diag}\Big[\Big(1 - \frac{2M}{r}\Big) \hat{H}_2,\ \frac{\hat{H}_2}{1 - 2M/r}\ , \\ r^2 \hat{K}_2,\ r^2 \hat{K}_2 \sin^2\theta \Big] \times Y^{20}(\theta, \phi) \end{aligned} \tag{3.28}$$

where "Diag" is short for diagonal matrix and $\hat{H}_2$ and $\hat{K}_2$ are functions of r only. The general solution to the field equation governing $\hat{H}_2$ can be expressed in terms of the associated Legendre functions [14]:

$$\hat{H}_2(r) = \alpha_2 P_2^2 \left(\frac{r}{M} - 1 \right) + \beta_2 Q_2^2 \left(\frac{r}{M} - 1 \right), \tag{3.29}$$

where α_2 and β_2 are constants to be determined. The solution to $\hat{K}_2$ can then be obtained from that of $\hat{H}_2$ (Appendix C). As r approaches $2M$, we have [28]

$$Q_\ell^2(r/M - 1) \sim (r/M)^{-1/2},$$

so the Q_2^2 term in Eq. (3.29) becomes divergent at $r = 2M$ and we must set the coefficient β_2 to be zero in order for the perturbation to be finite there. As r goes to infinity[2],

$$P_\ell^2(r/M - 1) \sim (r/M)^\ell.$$

Therefore the remaining P_2^2 term in Eq. (3.29) keeps growing quadratically as r becomes large, corresponding to the non-asymptotic-flatness due to the presence of the moon.

With the metric perturbation $h_{ab}^{(20)}$, we compute the Riemann tensor from the full metric and series expand the result up to linear order in α_2 (i.e., first order in the perturbation). The $0r0r$

---

[2] Valid for all Re $\ell > -1/2$

component of the resulting first-order Riemann tensor is found to be

$$R^{(1)}_{0r0r} = \frac{3\alpha_2}{M^2}\, Y^{20}(\theta, \phi). \tag{3.30}$$

From this and from Eq. (3.10), we obtain the first-order tidal field in the Cartesian basis

$$\mathcal{E}^{(1)}_{ij} = \frac{3\alpha_2}{M^2}\, \mathscr{Y}^{20}_{ij}. \tag{3.31}$$

The static, first-order tidal field thus contains *only* an $O(r^0)$ term, which should be identified as the static part of the applied external field $\mathcal{E}^{\text{ext},20}_{ij}$ [Eq. (3.11a)]. The coefficient α_2 is determined from this identification to be $\alpha_2 = \sqrt{4\pi/45}\,\mu M^2/b^3$. Since there is no $O(1/r^5)$ term present in Eq. (3.31), we infer that there is no static-induced quadrupole moment:

$$\mathscr{I}^{20}_{ij} = 0. \tag{3.32}$$

This is quite a counter-intuitive result. It is worth pointing out, however, that the absence of negative powers of r in Eq. (3.31) follows directly from the regularity condition we imposed at $r = 2M$. If the radius $r = 2M$ were well inside the central body itself, which naturally is the case for any nonrelativistic body with weak self-gravity, then the Q^2_2 term in Eq. (3.29) would survive and give rise to an induced quadrupole moment. Eq. (3.32) may also be the consequence of the gauge (Regge-Wheeler) we choose to work in. Is it possible to give a gauge-invariant definition of static, induced multipole moment in a non-asymptotically-flat spacetime? This is the question we shall investigate in the next subsection.

We now summarize and conclude that the total induced quadrupole moment *in our chosen gauge* is

$$\mathscr{I}^{\text{ind}}_{ij} = \mathscr{I}^{20}_{ij} + \mathscr{I}^{22}_{ij} + \mathscr{I}^{2-2}_{ij} = \frac{32}{45} M^6 \dot{\mathcal{E}}^{\text{ext}}_{ij}, \tag{3.33}$$

which is proportional to the time derivative of the external tidal field—not the field itself as one would expect for Newtonian tidal couplings.

Lastly, we move from the LARF to the perturbed horizon and examine the effect of the static perturbation there. Hartle has shown [14] that to first order in the perturbation, the coordinate location of the event horizon of a slowly rotating black hole perturbed by a stationary distribution of matter is still at $r = 2M$. This is also true for a Schwarzschild black hole under static perturbations. Evaluating the full metric at $r = 2M$, we find the horizon metric is given by

$$ds^2_H = 4M^2\Big[1 - 2\mu(M^2/b^3)P_2(\cos\theta)\Big]\left(d\theta^2 + \sin^2\theta d\phi^2\right), \tag{3.34}$$

where P_2 is the Legendre function. From this metric the scalar curvature of the horizon is obtained as

$$\mathscr{R} = \frac{1}{2M^2}\Big[1 - 4\mu(M^2/b^3)P_2(\cos\theta)\Big]. \tag{3.35}$$

So it is clear that the shape of the horizon does acquire a small quadrupolar component. But this deformation is *not* accompanied by an induced quadrupole moment in the LARF, at least in our chosen gauge.

3.4.2 Ambiguity of the static-induced quadrupole moment

In the previous subsection, we found that a Schwarzschild black hole has a vanishing static-induced quadrupole moment (SIQM) in response to the external tidal field $\mathcal{E}_{ij}^{\text{ext},20}$. To see that this vanishing of the SIQM might possibly be a gauge effect, imagine replacing the radial coordinate r in the expression $\Phi = (1/2)\mathcal{E}_{ij}^{\text{ext},20} n^i n^j r^2$ for the external tidal Newtonian potential by $r = \bar{r}(1 + \chi M^5/\bar{r}^5)^{1/2}$, where χ is some dimensionless number of order unity. The result is $\Phi = (1/2)\mathcal{E}_{ij}^{\text{ext},20} n^i n^j \bar{r}^2 + (\chi/2)M^5\mathcal{E}_{ij}^{\text{ext},20} n^i n^j/\bar{r}^3$. By comparing this expression with Eq. (3.2) we read off a SIQM $\mathscr{I}_{ij} = (\chi/18)M^5\mathcal{E}_{ij}^{\text{ext},20}$. In Newtonian theory this procedure would obviously be naive, but in general relativity, where the unperturbed black hole metric can be expanded in powers of M/r and the coefficients in that expansion depend on one's choice of radial coordinate and that choice is a "gauge" issue, this type of procedure is not obviously naive at all.

From our point of view, the best way to explore the gauge dependence of the SIQM is to ask whether it is physically measurable. If (as we shall find) physical measurements give a result that is ambiguous at some level, then that ambiguity constitutes a sort of gauge dependence of the SIQM.

In this section we shall study a thought experiment for measuring the SIQM, one based on coupling to a small, static external "test" octupole field $\mathcal{E}_{ijk}$ (proportional to the symmetrized and trace-removed gradient of some fiducial external quadrupolar tidal field). For simplicity we take $\mathcal{E}_{ijk}$ to be axisymmetric around the same z axis as our static external tidal field $\mathcal{E}_{ij}^{\text{ext},20}$; i.e., we take it to be proportional to a tensor spherical harmonic of order $(\ell, m) = (3, 0)$:

$$\mathcal{E}_{ijk} \sim \mathscr{Y}_{ijk}^{30}.$$

The analysis in [29] says that, any SIQM $\mathscr{I}_{ij}$ (created in the black hole by $\mathcal{E}_{ij}^{\text{ext},20}$) will couple to the external octupole moment to produce a force that gradually changes the hole's momentum[3]:

$$\dot{P}^i = -\frac{1}{2}\,\mathcal{E}^i{}_{jk}\mathscr{I}_{jk}. \tag{3.36}$$

(Eq. (1.12) of [18]; Eq. (4b) of [29]). The same will be true if the central black hole is replaced by a

---

[3] The test octupole field may also induce a static octupole moment $\mathscr{I}_{ijk}$ in the central black hole, which will couple to the external quadrupolar tidal field. This coupling, as we shall show, contributes to the ambiguities in the definition of the SIQM.

neutron star or any other spherical body. The rate of change of momentum $\dot{P}^i$ can also be evaluated by a surface integral of the Landau-Lifshitz pseudotensor $t^{ij}_{\rm LL}$ in the LARF [18]:

$$\dot{P}^i = -\oint (-g)\; t^{ij}_{\rm LL}\; dS_j. \tag{3.37}$$

Eqs. (3.36) and (3.37) for the coupling-induced force on the hole actually have ambiguities that arise from nonlinearities in the Einstein field equations. The origin of those ambiguities is discussed with care in Sec. I of Thorne and Hartle [18]. In this subsection we use Eq. (3.37) to calculate the force on the hole, and shall identify the ambiguities as those terms in which the force depends on the location of the integration surface. The result of our calculation will tell us, by comparison with Eq. (3.36), the SIQM and the amount by which it is ambiguous.

To compute the pseudotensor for insertion into Eq. (3.37), we must solve for the metric perturbation containing both the quadrupole and octupole terms:

$$\begin{aligned} h_{ab} &= h^{(20)}_{ab} + h^{(30)}_{ab} \\ &= \sum_{\ell=2,3} \mathrm{Diag}\Big[(1-2M/r)\,\hat{H}_\ell,\; \frac{\hat{H}_\ell}{1-2M/r}\;, \\ &\qquad\qquad r^2\hat{K}_\ell,\; r^2\hat{K}_\ell \sin^2\theta \Big] \times Y^{\ell 0}(\theta,\phi). \end{aligned} \tag{3.38}$$

When $\ell = 2$, the general solution to $\hat{H}_2$ is given in Eq. (3.29). For $\ell = 3$, we have

$$\hat{H}_3(r) = \alpha_3 P^2_3\left(\frac{r}{M} - 1\right) + \beta_3 Q^2_3\left(\frac{r}{M} - 1\right). \tag{3.39}$$

In order that both types of perturbation be finite at $r = 2M$, β_2 and β_3 must be set to zero [see Eq. (3.30)]. In order to deal with more general cases, however, we keep *non-vanishing* values for β_2 and β_3 in Eqs. (3.29) and (3.39) so the following analysis will be valid for stars as well as black holes. [For central bodies other than black holes, β_2 and α_2 (and similarly β_3 and α_3) are not independent of each other: β_2 is proportional to α_2 with a proportionality constant that depends on the body's internal physical properties]. Having specified the metric perturbation, we then insert the full metric into the expression for the pseudotensor (Eq. (20.22) of [30])

$$\begin{aligned} (-g)t^{\alpha\beta}_{\rm LL} &= \frac{1}{16\pi}\Big\{ \mathfrak{g}^{\alpha\beta}{}_{,\lambda}\mathfrak{g}^{\lambda\mu}{}_{,\mu} - \mathfrak{g}^{\alpha\lambda}{}_{,\lambda}\mathfrak{g}^{\beta\mu}{}_{,\mu} + g_{\lambda\mu}g^{\nu\rho}\mathfrak{g}^{\alpha\lambda}{}_{,\nu}\mathfrak{g}^{\beta\mu}{}_{,\rho} \\ &- \left(g^{\alpha\lambda}g_{\mu\nu}\mathfrak{g}^{\beta\nu}{}_{,\rho}\mathfrak{g}^{\mu\rho}{}_{,\lambda} + g^{\beta\lambda}g_{\mu\nu}\mathfrak{g}^{\alpha\nu}{}_{,\rho}\mathfrak{g}^{\mu\rho}{}_{,\lambda} \right) \\ &+ \frac{1}{2}g^{\alpha\beta}g_{\lambda\mu}\mathfrak{g}^{\lambda\nu}{}_{,\rho}\mathfrak{g}^{\rho\mu}{}_{,\nu} + \frac{1}{8}\left(2g^{\alpha\lambda}g^{\beta\mu} - g^{\alpha\beta}g^{\lambda\mu}\right) \\ &\times \left(2g_{\nu\rho}g_{\sigma\tau} - g_{\rho\sigma}g_{\nu\tau}\right)\mathfrak{g}^{\nu\tau}{}_{,\lambda}\mathfrak{g}^{\rho\sigma}{}_{,\mu}\Big\}, \end{aligned} \tag{3.40}$$

and evaluate the surface integral at some radius $r = R$ in the LARF. Because of the axisymmetry of the perturbed spacetime, only the z-component of $\dot{P}^i$ is nonzero. The result, up to first-order coupling and with uninteresting numerical coefficients being suppressed, has the following form:

$$\begin{aligned} \dot{P}^z &= \alpha_3\alpha_2 \left[\frac{R^4}{M^4} \ \& \ \frac{R^3}{M^3} \ \& \ \frac{R^2}{M^2} \ \& \ \frac{R}{M} \ \& \ 1 \ \& \ ...\right] \\ &+ \alpha_3\beta_2 \left[1 \ \& \ \frac{M}{R} \ \& \ ...\right] + \beta_3\alpha_2 \left[\frac{M^3}{R^3} \ \& \ \frac{M^4}{R^4} \ \& \ ...\right], \end{aligned} \tag{3.41}$$

where "&" is to be read "and a term of the order."

The constant terms in Eq. (3.41) [i.e., the "1"s] that are independent of the integration radius R are the ones to be compared with Zhang's result (3.36) so as to deduce the gauge-invariant SIQM. Other terms that depend on R constitute ambiguities[4]. Terms with positive power(s) of R/M appear because the spacetime is not asymptotically flat, and they prevent us from minimizing the ambiguities by simply pushing the integration surface to infinity.

Let us step back and write down the most general form that the SIQM can take. By order of magnitude analysis of the response of any physical body (black hole, star, planet, moon, ...) to a tidal field, we must have

$$\mathscr{I}_{ij} \sim L^5(1+\xi)\ \mathcal{E}^{\mathrm{ext},20}_{ij}. \tag{3.42}$$

Here L is the size of the body ($L \sim M$ for a black hole) and ξ is a dimensionless number describing the SIQM's dependence on the integration radius R—deviations from being well-defined. From Eq. (3.31), we know the external tidal field scales as $\sim \alpha_2/M^2$. Similarly for the external octupole field, $\mathcal{E}_{ijk} \sim \alpha_3/M^3$. Using these relations, Eq. (3.36) becomes

$$\begin{aligned} \dot{P}^i &\sim L^5(1+\xi)\ \mathcal{E}^{\mathrm{ext},20}_{jk}\ \mathcal{E}^{i}{}_{jk} \\ &\sim \alpha_2\alpha_3 \left[\frac{L^5}{M^5} + \frac{\xi L^5}{M^5}\right]. \end{aligned} \tag{3.43}$$

Here the first term in the square bracket should be identified as the "1"s in Eq. (3.41) [note again that β_2 and α_2 are not independent of each other for stars]; and the second term should be identified as the sum of all R-dependent terms:

$$\frac{\xi L^5}{M^5} = \frac{R^4}{M^4} \ \& \ ... \ \& \ \frac{R}{M} \ \& \ \frac{M}{R} \ \& \ .... \tag{3.44}$$

In the case of a black hole we have $L \sim M$ and the smallest the right-hand side of Eq. (3.44)

---

[4] The M^2/R^2 term includes the effect of any octupole moment induced on the central body by the test octupole field. Note that $\dot{P}^i$ is a dimensionless vector. On dimensional grounds, the coupling between any induced octupole moment and the external tidal field must take the form $\mathscr{I}^{ijk}\mathcal{E}_{jk}/R^2$ to contribute to $\dot{P}^i$. (Nonlinear coupling to the monopole moment can lead to similar terms that scale as higher, but not lower, powers of $1/R$).

can be is ~ 1 (for $R \sim M$), so $\xi \gtrsim 1$, i.e., *the SIQM for a Schwarzschild black hole is ambiguous by an amount* $\gtrsim M^5\mathcal{E}_{ij}^{\mathrm{ext},20}$, i.e., *totally ambiguous*, since the largest we could expect $\mathscr{I}_{ij}$ to be is $\sim M^5\mathcal{E}_{ij}^{\mathrm{ext},20}$.

For central objects with $L \gg M$ (e.g., the Earth) we must choose $R > L$. The right-hand side of Eq. (3.44) is then minimized by setting $R \simeq L$, giving $\xi \sim M/L \ll 1$ ($\sim 10^{-9}$ in the case of the Earth) for the fractional ambiguities in the SIQM.

We comment that our result for a Schwarzschild black hole differs from what Suen has derived. Suen has given an unambiguous prescription to read out static multipole moments in non-asymptotically-flat spacetimes, which is based on transforming coordinates into a particular set of de Donder coordinates [31]. He has used his prescription to calculate the induced quadrupole moment of a Schwarzschild black hole when it is perturbed by a static, equatorial matter ring at large distances [19]. According to his prescription, the SIQM does *not* vanish. It is proportional to the tidal field produced by the ring:

$$\mathscr{I}_{ij} = -\frac{4}{21}M^5\mathcal{E}_{ij}^{\mathrm{ring}}. \tag{3.45}$$

The incompatibility between this result and the vanishing SIQM that we derived in Sec. 3.4.1 in Regge-Wheeler gauge and Schwarzschild coordinates illustrates the ambiguities of the SIQM. Both results, zero and $(-4/21)M^5\mathcal{E}_{ij}$, are less than or of order the ambiguity.

3.5 The tidal phase shift

In the LARF, the time-dependent induced quadrupole moment is $\pi/4$ out of phase with the perturbing tidal field (Sec. 3.3.1). This large phase shift is quite different from the small phase lag angle, caused by viscous dissipation, between a planet's induced quadrupole moment and the perturbing tidal field. A closer black-hole analogy to a planet's viscous phase lag may be found by considering the tide raised on the hole's horizon by an orbiting moon.

In this section, we compute the tidal phase shift on the horizon for our perturbed Schwarzschild black hole. We will discuss in what sense it is and is not analogous to the fluid-planet's viscous phase lag. To calculate this phase shift, it is convenient to use the Newman-Penrose formalism [32] (see, e.g., Chapter 1 of [33] for a review of the Newman-Penrose formalism). Appendix 3.10 summarizes some details of the Newman-Penrose formalism that are relevant for our purpose.

We consider two approaches to defining the tidal phase shift. In Sec. 3.5.1, we define the phase shift only in terms of quantities on the horizon (following the method suggested in Sec. VIIC of [22]), while in Sec. 3.5.2, we define a phase between the tide raised on the horizon and the "retarded" position of the moon (following the method used by Hartle in [15]).

3.5.1 Phase of the tidal bulge on the horizon

For Sec. 3.5 and Appendix 3.10 only, we use ingoing Eddington-Finkelstein coordinates $(\tilde{V}, r, \theta, \phi)$ and a $(+\ -\ -\ -)$ signature of the metric. The Schwarzschild metric in these coordinates is

$$ds^2 = \left(1 - \frac{2M}{r}\right) d\tilde{V}^2 - 2d\tilde{V}dr - r^2\left(d\theta^2 + \sin^2\theta d\phi^2\right). \tag{3.46}$$

The ingoing Eddington-Finkelstein null time coordinate $\tilde{V}$ is related to the Schwarzschild time coordinate t and radial coordinate r by the following equation (Eq. (1b) of Box 32.2 of [30]):

$$\tilde{V} = t + r^* = t + r + 2M \ln |r/2M - 1|\,, \tag{3.47}$$

and the Eddington-Finkelstein radial and angular coordinates $\{r, \theta, \phi\}$ are identical to those of Schwarzschild.

Our slowly orbiting moon deforms the Schwarzschild event horizon. By analogy with Newtonian tides, we would like to describe the horizon deformation as a perturbation that co-rotates (at a slightly different phase) with the tidal field that drives it. But this viewpoint inherently envisions the perturbed event horizon as a two-dimensional, evolving surface, rather than as a three-dimensional, global surface in spacetime. Therefore, before we can consider the *phases* of quantities on the horizon, we must first specify what we mean by *time* on the horizon.

Begin by considering the Schwarzschild event horizon (which is, of course, the three-surface $r = 2M$). There is a preferred way to slice the horizon into a single-parameter family of two-surfaces; this preferred slicing uses two-surfaces that are orthogonal to the Schwarzschild Killing vector $\partial_t = \partial_{\tilde{V}}$ that is timelike at the moon and null on the horizon. Following Hartle [15], we call this family of two-surfaces the "instantaneous horizon." The instantaneous horizon can be pictured as an evolving two-surface defined by $r = 2M$ and $\tilde{V} = \text{const}$, so that $\tilde{V}$ plays the role of a "time" coordinate. Throughout this section, we use the terms "horizon" and "instantaneous horizon" interchangeably unless otherwise indicated.

We now consider how the horizon's perturbation evolves with time $\tilde{V}$. The moon's tidal field, characterized in the LARF by [Eq. (3.10)]

$$\mathcal{E}_{ij}^{\text{ext}} = \mathcal{E}_{ij}^{\text{ext},20} + \mathcal{E}_{ij}^{\text{ext},22} + \mathcal{E}_{ij}^{\text{ext},2-2},$$

deforms the otherwise spherical, static horizon. Because $\mathcal{E}_{ij}^{\text{ext},20}$ is static and axisymmetric, it cannot contribute to the phase shift. For the remaining tidal fields, $\mathcal{E}_{ij}^{\text{ext},2\pm2}$, we shall consider only the $(2,2)$ mode in detail and the result for the $(2,-2)$ mode follows immediately.

On the horizon, it is the tangential-tangential components of the perturbing tidal field that drive the deformation (see, e.g., Eq. (6.80) of [22]); knowledge of these components is physically equivalent to knowledge of the Teukolsky function Ψ_0 [16] (see, e.g., Eq. (A7) of [34]). The Teukolsky function is a particular component of the Weyl tensor [Eq. (3.86a)].

The horizon deformation is governed by the Newman-Penrose equation (Eq. (2.11) of [15])

$$(\partial_{\tilde{V}} - 2\epsilon)\sigma^{(1)} = -2(i\Omega + \epsilon)\sigma^{(1)} = \Psi_0^{(1)}. \tag{3.48}$$

This is also the "tidal force equation" (equation (6.80) of [22]). Here $\sigma = -\Sigma^{(1)}$ is a Newman-Penrose spin coefficient [Eq. (3.84e)] and $\Sigma^{(1)}$ is the shear (i.e., the rate of change of the shape[5]) of the instantaneous horizon. Note that because Σ and Ψ_0 vanish on the unperturbed instantaneous horizon, the spin coefficient ϵ takes its Schwarzschild value, which (in our tetrad) is the surface gravity of the instantaneous horizon $g_H = (4M)^{-1}$.

Knowing $\Psi_0^{(1)}$, we can evaluate the horizon shear. Because $\Psi_0^{(1)}$ is first order in the perturbation, it may be evaluated on the horizon simply by letting r go to $2M$.

Beginning with the $(\ell, m) = (2, 2)$ metric perturbation [Eq. (3.12), except we now choose the metric signature to be $(+\ -\ -\ -)$], we compute the perturbed Riemann tensor near the horizon and read off the component $\Psi_0^{(1)}$. The result is

$$\begin{aligned}\Psi_0^{(1)} &= -i\sqrt{\frac{\pi}{5}}\frac{\mu M \Omega}{b^3}\ {}_2Y^{22} e^{-2i\Omega\tilde{V} + (8/3)M\Omega} + O(M^2\Omega^2) \\ &= |\Psi_0^{(1)}| \exp\left[2i\left(\phi - \Omega\tilde{V} + \frac{4}{3}M\Omega - \frac{\pi}{4}\right)\right] \\ &\quad + O(M^2\Omega^2).\end{aligned} \tag{3.49}$$

Here ${}_2Y^{22}$ is the spin-weighted spherical harmonic

$${}_2Y^{22} = \frac{1}{2}\sqrt{\frac{5}{\pi}}\sin^4\left(\frac{\theta}{2}\right) e^{2i\phi}.$$

With $\Psi_0^{(1)}$ in hand, we can calculate $\Sigma^{(1)}$ via Eq. (3.48). Inserting $\epsilon = 2g_H$ and $\omega = 2\Omega$ into Eq. (3.48) yields

$$\begin{aligned}\Sigma^{(1)} &= \frac{\Psi_0^{(1)}}{i\omega + 2\epsilon} \\ &= 4M\Psi_0^{(1)} e^{-2i\Omega/g_H} + O(M^2\Omega^2) \\ &= |\Sigma^{(1)}| \exp\left[2i\left(\phi - \Omega\tilde{V} + \frac{4}{3}M\Omega - \frac{\pi}{4} - \delta_{\text{Horizon}}\right)\right] \\ &\quad + O(M^2\Omega^2)\end{aligned} \tag{3.50}$$

---

[5] Recall that the shape of the instantaneous horizon (a two-dimensional surface) is completely specified by its intrinsic scalar curvature $\mathscr{R}$.

where

$$\delta_{\rm Horizon} \equiv \Omega/g_H = 4M\Omega. \tag{3.51}$$

The shear $\Sigma^{(1)}$ *leads* $\Psi_0^{(1)}$ (or equivalently, the perturbing tidal field at the horizon) by an angle $\delta_{\rm Horizon}$. [Note that the first equality in Eq. (3.50) appears in [15] as Eq. (2.12).]

The shear is the time derivative of the shape. Therefore, the shape has a phase

$$\mathscr{R}^{(1)} = |\mathscr{R}^{(1)}| \exp\left[2i\left(\phi - \Omega\tilde{V} - \frac{8}{3}M\Omega\right)\right]. \tag{3.52}$$

In other words, the shear leads the shape by $\pi/4$.

The horizon phase shift in Eq. (3.51) follows directly from the tidal force equation (3.48). It is gauge-invariant since it only makes reference to gauge-invariant quantities measured on the instantaneous horizon. In [22] [Eq. (7.45), Fig. 57, and the surrounding discussion], an analogous horizon phase shift $\delta^{\rm H}_{\rm Horizon}$ was deduced from the tidal force equation for a slowly rotating black hole perturbed by a stationary, axisymmetric tidal field—physically the same problem as Hartle studied [15]:

$$\delta^{\rm H}_{\rm Horizon} = \Omega_H/g_H = 4M\Omega_H = \delta_{\rm Horzion}\,|_{\Omega\to\Omega_H}\,. \tag{3.53}$$

Here Ω_H is the horizon angular velocity.

Although Hartle also used the tidal force equation in his calculations, he chose to define the tidal phase shift in a different way and made his result gauge-invariant by making a connection between the angular positions on the horizon and angular positions at infinity through a null ray—a choice we will consider in detail in Sec. 3.5.2.1 and apply to our problem in Sec. 3.5.2.2.

The phase lead $\delta_{\rm Horizon}$ is, in some ways, analogous to the phase shift of a tide raised on a non-rotating fluid planet. In the latter case, viscous dissipation causes the shape of the planet's surface to lag the normal-normal component of the perturbing tidal field by a small angle $\delta_{\rm visc}$; somewhat analogously, the horizon shear leads the tangential-tangential component of the perturbing tidal field. Both phase shifts are small angles associated with dissipation (which manifests itself as a secular evolution of the energy and angular momentum of the moon's orbit). In the absence of dissipation, there is no phase shift. On the other hand, the phase shift $\delta_{\rm Horizon}$ is a *lead* angle while $\delta_{\rm visc}$ is a *lag* angle. Hartle explains this difference as a consequence of the teleological nature of the horizon [15]. Also as Hartle observed, when the angular velocity Ω is not small compared with $1/M$, the deformation of the horizon cannot be described in terms of a phase shift [15].

3.5.2 Phase shift between the tidal bulge and the moon

As an alternative to the above way of defining the tidal phase shift, one can define it as the angle between the tidal bulge on the horizon and the location of the moon in its orbit. Hartle used this approach when he computed the tidal lead on a rotating hole perturbed by a stationary moon [15]. First, we will briefly summarize the aspects of Hartle's analysis which are relevant to our purpose. Then, we will apply his method to a slowly rotating moon around an otherwise Schwarzschild black hole.

3.5.2.1 Tidal phase shift between a rotating horizon and stationary moon

In [15], Hartle considers the problem of a distant, stationary moon perturbing a slowly rotating black hole.

The Kerr metric can be written as

$$\begin{aligned} ds^2 &= \left(1 - \frac{2Mr}{\Sigma}\right) d\tilde{V}^2 - 2d\tilde{V}dr + \frac{4aMr\sin^2\theta}{\Sigma} d\tilde{V}d\tilde{\phi} \\ &\quad +2a\sin^2\theta dr d\tilde{\phi} - \Sigma d\theta^2 \\ &\quad -\sin^2\theta\left(a^2 + r^2 + \frac{2a^2Mr\sin^2\theta}{\Sigma}\right) d\tilde{\phi}^2. \end{aligned} \tag{3.54}$$

Here $\Sigma \equiv r^2 + a^2\cos^2\theta$. The coordinates $\tilde{V}$ and $\tilde{\phi}$ are related to the usual Boyer-Lindquist coordinates t and ϕ by

$$\begin{aligned} dt &= d\tilde{V} - \frac{r^2 + a^2}{\Delta} dr \\ d\phi &= d\tilde{\phi} - \frac{a}{\Delta} dr \end{aligned} \tag{3.55}$$

where $\Delta \equiv r^2 - 2Mr + a^2$. When $a = 0$, Eq. (3.54) reduces to the Schwarzschild metric in Eddington-Finkelstein coordinates [Eq. (3.46)].

The event horizon is the surface $r = r_+ \equiv M + \sqrt{M^2 - a^2}$. Just as in the Schwarzschild case considered above, the event horizon can be sliced into a single-parameter family of two-dimensional surfaces using the Killing vector $\partial_{\tilde{V}}$ which is timelike at infinity and null on the horizon. This family of surfaces is the instantaneous horizon.

The distant moon raises a tidal bulge on the central hole's instantaneous horizon. In the limit that the moon is far away, the change in the horizon's shape (or equivalently, the change in the scalar curvature $\mathscr{R}$ of the instantaneous horizon), is purely quadrupolar.

The deformation is driven by the transverse-transverse component of the tidal field at the horizon, which is physically equivalent to the Teukolsky function, a particular component of the Riemann tensor Ψ_0 [Eq. (3.86a)]. This component vanishes in the unperturbed Kerr spacetime [Eq. (3.93a)], and the first-order correction $\Psi_0^{(1)}$ has the form

$$\Psi_0^{(1)} = S^{\ell m}(r)\ {}_2Y^{\ell m}(\theta, \tilde{\phi}) \tag{3.56}$$

where ${}_2Y^{\ell m}$ is a spin-weight-2 spherical harmonic. Because the perturbation is purely quadrupolar, we need only consider the case $\ell = 2, m = 2$ here, although Hartle considers the generic case. Hartle uses Teukolsky's solution [35] for the stationary radial functions $S^{\ell m}$ due to the ℓ-pole perturbation caused by a distant, stationary point particle with mass μ. Furthermore, while Hartle treats the case of a moon at any location $(\theta, \tilde{\phi})$, for concreteness we specify the moon's position as $(\theta, \tilde{\phi}) = (\pi/2, 0)$. On the horizon, the Teukolsky function turns out to have the value (combining Eqs. (4.30), (4.31), (4.15), and (4.18) of [15])

$$\begin{aligned}\Psi_0^{(1),\mathrm{H}} &= \frac{i\mu M\Omega_H}{2\sqrt{6}b^3}\sin^4\left(\frac{\theta}{2}\right)\exp\left[2i\left(\tilde{\phi}+2M\Omega_H\right)\right] \\ &\quad +O\left(\frac{M^4}{b^4}\right)+O\left(M^2\Omega_H^2\right). \end{aligned} \tag{3.57}$$

The tidal field deforms the instantaneous horizon, changing its shape and thus its two-dimensional scalar curvature $\mathscr{R}$. Hartle computes the quadrupolar correction to the scalar curvature, $\mathscr{R}^{(1),\ell=2,\mathrm{H}}$, of the instantaneous horizon [Eq. (3.90)]. His result is (Eqs. (4.26)–(4.27) of [15])

$$\begin{aligned}\mathscr{R}^{(1),\ell=2,\mathrm{H}} &\propto \cos\left[2\left(\tilde{\phi}+\frac{14}{3}M\Omega_H\right)\right] \\ &\quad +O\left(\frac{M^4}{b^4}\right)+O\left(M^2\Omega_H^2\right). \end{aligned} \tag{3.58}$$

Instead of measuring the angle between the shear σ and the tidal field Ψ_0 on the horizon, Hartle defines his phase lead as the angle between the shape and the moon's angular position. To make this definition gauge-invariant, Hartle chooses ingoing, zero-angular-momentum, null geodesics to be "lines of constant angle." He then compares the angular position of the horizon tidal bulge,

$$\tilde{\phi}^{\mathrm{H}}_{\mathrm{bulge}} = -\frac{14}{3}M\Omega_H \tag{3.59}$$

to the angular position of the moon on the horizon.

Consider stationary moon in the equatorial plane at (large) radius $r = b$ and at angular position $\phi = 0$. An ingoing null ray, originating from the moon, intersects the instantaneous horizon at angular position[6]

$$\tilde{\phi}^{\mathrm{H}}_{\mathrm{moon}} = a/b - a/2M. \tag{3.60}$$

---

[6] Note that there is a sign error in Hartle's analysis. Hartle incorrectly states that the ingoing null ray intersects the horizon at $+a/2M + O(a/b)$, not $-a/2M + O(a/b)$. Had we also made this error, there would be a coefficient of 20/3 instead of 8/3 in Eq. (3.61).

The tidal bulge therefore *leads* the moon's position by an amount

$$\begin{aligned}\delta^{\mathrm{H}}_{\text{null map}} &= \tilde{\phi}^{\mathrm{H}}_{\text{moon}} - \tilde{\phi}^{\mathrm{H}}_{\text{bulge}} \\ &= \frac{8}{3}M\Omega_H + 4\frac{M^2\Omega_H}{b}. \end{aligned} \tag{3.61}$$

Here we have used the relation (valid for small a/M) that $a = 4M^2\Omega_H$, with Ω_H being the angular velocity of the hole. For simplicity, one can then take the limit $b \to \infty$.

Before continuing, we should remark that Hartle's prescription for constructing $\delta^{\mathrm{H}}_{\text{null map}}$ can be described without reference to the moon's position. Begin by computing the angular location of the tidal bulge on the horizon. Next, ingoing, zero-angular-momentum null rays from infinity define lines of constant angle, so that there is a one-to-one correspondence between angular positions on the horizon and angular positions at infinity. The angular position at infinity of the tidal bulge can thus be computed. Finally, perform the calculation again, but this time perturb a *non-rotating spacetime*; in this case, there will be no tidal friction. Because the Kerr and Schwarzschild spacetimes are asymptotically identical, one can unambiguously compare the angular position of the tidal bulge in the presence and in the absence of tidal friction: $\delta^{\mathrm{H}}_{\text{Null Map}} = \phi^{\mathrm{H}}_{\text{bulge}} - \phi^{\mathrm{H}}_{\text{bulge, no friction}}$. This is equivalent to the previous definition of $\delta^{\mathrm{H}}_{\text{null map}}$ provided that $b \to \infty$.

However, this alternative formulation of $\delta^{\mathrm{H}}_{\text{null map}}$ breaks down when the moon, not the horizon, rotates. The rotation is then described by Ω, which is a parameter of the perturbation, not of the background spacetime. To eliminate tidal friction, one must let $\Omega \to 0$, which eliminates the perturbation[7]. Because of this failure, we prefer to consider Hartle's phase shift as a comparison of the position of the tidal bulge with the position of the moon.

3.5.2.2 Tidal phase shift between a non-rotating horizon and rotating moon

A similar analysis can be applied to our system, in which a distant moon in a slow, circular orbit raises a tide on a non-rotating black hole.

The moon orbits the central black hole along the world line specified by Eq. (3.8). In other words, the moon has a phase given by

$$\phi_{\text{moon}}(\tilde{V}) \equiv \Omega t = \Omega(\tilde{V} - b^*). \tag{3.62}$$

This must be compared with the location of the bulge on the hole's future horizon. Eq. (3.52) for $\mathscr{R}^{(1)}$ [or, alternatively, inserting Eq. (3.49) into Eq. (3.90)] shows that the tip of the tidal bulge has a phase given by

$$\phi_{\text{bulge}} = \Omega\tilde{V} + \frac{8}{3}M\Omega. \tag{3.63}$$

---

[7] Even if $\Omega \to 0$ resulted in a non-zero perturbation, it is unclear how to distinguish such a perturbation from a small change in the coordinates of the background spacetime.

As time $\tilde{V}$ passes, this bulge rotates around and around the horizon, with the same angular velocity Ω as the moon that raises the tide.

Following Hartle, we compare the angular location of the tidal bulge, $\phi_{\rm bulge}(\tilde{V})$, with the angular location of the moon, $\phi_{\rm moon}(\tilde{V})$, using ingoing, zero angular momentum (ZAM) null rays to provide the connection between ϕ at the moon's orbit and ϕ on the horizon. In the ingoing Eddington-Finkelstein coordinates that we are using, these ZAM rays have a very simple form:

$$\{\tilde{V}, \theta, \phi\} = \text{constant}\ ,\ \ r \text{ decreases from } b \text{ to } 2M\ . \tag{3.64}$$

Since $\tilde{V}$, θ, and ϕ are all constant along these rays, they give us a one-to-one map of events $\{\tilde{V}, r = b, \theta, \phi\}$ at the moon's orbital radius to events $\{\tilde{V}, r = 2M, \theta, \phi\}$ on the horizon that have identically the same $\tilde{V}$, θ, and ϕ. With the aid of this map, we conclude that the angle by which the horizon bulge lags the moon's position is

$$\delta_{\rm null\ map} \equiv \phi_{\rm bulge}(\tilde{V}) - \phi_{\rm moon}(\tilde{V}) = \frac{8}{3} M\Omega + \Omega b^*. \tag{3.65}$$

[Eqs. (3.62) and (3.63)]. Again, the phase shift is a phase lead, not a phase lag, due to the teleological nature of the horizon.

In addition to the teleological phase shift of order $M\Omega$, $\delta_{\rm null\ map}$ contains a much larger term of magnitude Ωb^*; this term reflects the choice to use an ingoing-null-ray mapping between the moon and the horizon. A similar term appears in Hartle's calculation [Eq. (3.61)], but in Hartle's system the term is much *smaller* than the teleological phase shift size (specifically, smaller by a factor of M/b), whereas $\Omega b^* \gg M\Omega$.

One could avoid this problem by *defining* the phase shift to include only terms of order $M\Omega$ and $M\Omega_H$. With this definition, the remaining tidal phase leads are the same: $(8/3)M\Omega$, as one would expect, given that a there should be no tidal shift at all if the moon were to rotate at the hole's angular velocity, i.e., if $\Omega = \Omega_H$.

We prefer, however, to define the tidal lead angle in as the angle $\delta_{\rm Horizon} = 4M\Omega$ by which the horizon shear leads the horizon tidal field. This angle, in contrast to $\delta_{\rm null\ map}$, is defined in terms of an "instantaneous" (spacelike) connection between the moon and the horizon, i.e., by the near zone mapping of the moon's position to the horizon tidal field's [$\Psi_0^{(1)}$'s] maximum. [Had the moon been in the radiation zone ($b \gg \lambda/2\pi$), one would have expected the connection to be light-like.]

3.6 Conclusion

For our simple system of a Schwarzschild black hole and circularly orbiting moon, we have found that the time-dependent part of the moon's tidal field induces a quadrupole moment that is unambiguous.

The static-induced quadrupole moment was found to be zero in the Regge-Wheeler gauge, but it is ambiguous in general. The ambiguity of the static-induced quadrupole moment leads to an ambiguity in the phase of the induced quadrupole moment in the LARF; however, the tidal bulge on the horizon still has a well-defined phase shift with respect to the orbiting moon. Because of the ambiguity of the induced quadrupole moment and the LARF phase shift, we conclude that the polarizability and phase shift are not suitable for constructing a body-independent description of tidal coupling in EMRIs.

However, this conclusion does not eliminate the possibility of developing a body-independent language to describe tidal coupling, including cases where the central body is a black hole. It might be possible, for instance, to define a new set of induced "dissipative multipole moments" for the central body—i.e., moments that vanish in the absence of tidal friction. Such dissipative moments would still be linear in the perturbing tidal field, so one could still define a polarizability. Also, by ignoring any non-dissipative tidal coupling, the phase shift might no longer contain additional information. Even if such an extension does not prove feasible, tidal coupling can still be described in the more conventional (but still body-independent) language of energy and angular momentum transfer between the moon and the central body.

Other future work could include generalizing our analysis to spinning black holes, treating noncircular, non-equatorial orbits, and (most importantly) studying how information about tidal coupling in EMRIs can be extracted from the gravitational waves detected by LISA.

3.7 Appendix A: Symmetric trace-free tensor notation for spherical harmonics

The scalar spherical harmonics $Y^{\ell m}(\theta,\phi)$ can be written in terms of of rank-ℓ symmetric trace-free (STF) tensors [23]. The spherical harmonics $Y^{2m}(\theta,\phi)$ that have been used in this paper are

$$Y^{2\pm 2}(\theta,\phi) = \frac{1}{4}\sqrt{\frac{15}{2\pi}}\sin^2\theta e^{\pm 2i\phi} \tag{3.66a}$$

$$Y^{20}(\theta,\phi) = \frac{1}{8}\sqrt{\frac{5}{\pi}}\left(1+3\cos 2\theta\right). \tag{3.66b}$$

They can be written in terms of rank-2 STF tensors as (Eq. (2.11) of [23])

$$Y^{2m}(\theta,\phi) = \mathscr{Y}^{2m}_{ij} n^i n^j, \tag{3.67}$$

where $n^i \equiv x^i/r$ and $\mathscr{Y}^{2m}_{ij}$ are the STF tensors given by (Eq. (2.12) of [23]):

$$\mathscr{Y}^{20}_{ij} = -\frac{1}{4}\sqrt{\frac{5}{\pi}}\begin{pmatrix} 1 & 0 & 0 \\ 0 & 1 & 0 \\ 0 & 0 & -2 \end{pmatrix}, \tag{3.68}$$

$$\mathscr{Y}^{2\pm2}_{ij} = \frac{1}{4}\sqrt{\frac{15}{2\pi}}\begin{pmatrix} 1 & \pm i & 0 \\ \pm i & -1 & 0 \\ 0 & 0 & 0 \end{pmatrix}. \tag{3.69}$$

3.8 Appendix B: Time-dependent perturbation equations

In Regge-Wheeler gauge, the metric perturbation for a given even-parity (ℓ, m, ω) mode depends on the three radial functions H, H_1, and K. In this appendix, we introduce the Zerilli function $\mathbb{Z}$ and the Regge-Wheeler function $\mathbb{X}$ and describe how we obtain the radial functions from them. The description here will hold for a general (ℓ, m, ω), while the results derived in Sec. (3.3) rely on the special case when $(\ell, m, \omega) = (2, 2, 2\Omega)$.

The original Zerilli's master function is defined implicitly through its relation with the two radial functions H_1 and K [Eqs. (13) and (14) of [25] with ${R_{LM}}^{(e)}$ replaced by $\mathbb{Z}$]:

$$H_1 = -i\omega\frac{\lambda r^2 - 3\lambda M r - 3M^2}{(r-2M)(\lambda r + 3M)}\mathbb{Z} - i\omega r\frac{d\mathbb{Z}}{dr}, \tag{3.70}$$

$$K = \frac{\lambda(\lambda+1)r^2 + 3\lambda M r + 6M^2}{r^2(\lambda r + 3M)}\mathbb{Z} + \frac{d\mathbb{Z}}{dr^*}, \tag{3.71}$$

where

$$\lambda \equiv \frac{1}{2}(\ell-1)(\ell+2).$$

Using the algebraic relationship (Eq. (10) of [26])

$$\begin{aligned}\left(\frac{3M}{r} + \lambda\right)H &= \left[i\omega r - \frac{i(\lambda+1)M}{\omega r^2}\right]H_1 + \\ &\quad \left(\lambda + \frac{M}{r} - \frac{M^2/r^2 + \omega^2 r^2}{1 - 2M/r}\right)K\end{aligned}$$

one can obtain H in terms of the Zerilli function

$$H = \left[\frac{\omega^2 r^2}{2M - r} + \frac{s_1}{r^2(3M + \lambda r)^2}\right]\mathbb{Z} + s_2\frac{d\mathbb{Z}}{dr}, \tag{3.72}$$

in which

$$\begin{aligned} s_1 &= 9M^2(M+\lambda r)+\lambda^2 r^2[3M+(\lambda+1)r], \\ s_2 &= \frac{-3M^2-3\lambda M r+\lambda r^2}{r(3M+\lambda r)}. \end{aligned}$$

The Zerilli function obeys the wave equation (Eqs. (18) and (19) of [25]):

$$\left[\frac{d^2}{dr^{*2}}+\omega^2-V(r)\right]\mathbb{Z}=0, \tag{3.73}$$

in which the potential term is given by

$$\begin{aligned} V(r) &= \frac{2(r-2M)}{r^4(\lambda r+3M)^2}\Big[\lambda^2(\lambda+1)r^3+ \\ &\qquad 3\lambda^2 M r^2+9\lambda M^2 r+9M^3\Big]. \end{aligned}$$

The odd-parity master function, the Regge-Wheeler function, is defined in Eq. (23) of [24] (and is called Q in Regge and Wheeler's notation). It obeys the differential equation (Eq. (7) of [26]):

$$\left[\frac{d^2}{dr^{*2}}+\omega^2-\Big(1-\frac{2M}{r}\Big)\Big(\frac{\ell(\ell+1)}{r^2}-\frac{6M}{r^3}\Big)\right]\mathbb{X}=0. \tag{3.74}$$

The connection between the Regge-Wheeler and Zerilli functions was first found by Chandrasekhar and is listed, e.g., in Eq. (152) of Ch. 4 of [33]:

$$\begin{aligned} \Big[\lambda(\lambda+1)-3iM\omega\Big]\mathbb{Z} &= \left[\lambda(\lambda+1)+\frac{9M^2(r-2M)}{r^2(\lambda r+3M)}\right]\mathbb{X} \\ &+ 3M\left(1-\frac{2M}{r}\right)\frac{d\mathbb{X}}{dr}. \end{aligned} \tag{3.75}$$

This completes our metric reconstruction scheme from the Regge-Wheeler function. We are now ready to evaluate the radial metric perturbation functions H, H_1, and K for the $(\ell,m)=(2,2)$ mode of the perturbations. Expanding X^H [given in Eq. (3.16) in powers of $\tilde{r}\equiv r/2M$ to first order in $\varepsilon\equiv 2M\omega$], we obtain

$$X^H=\mathcal{A}\left[\Big(1+\frac{13}{12}i\varepsilon\Big)\tilde{r}^3+\sum_{n=5}^{\infty}\frac{i\varepsilon}{n\tilde{r}^{n-3}}+O(\varepsilon^2)\right]. \tag{3.76}$$

Here $\mathcal{A}$ is an overall scaling factor (Eq. (3.20) in Sec. 3.3.1). While the summation can be rewritten as a closed-form expression, we prefer to stay in the series notation, since our interest is in reading various powers of r in the resulting first-order tidal field. Eq. (3.76) is the value of the Regge-Wheeler function in the LARF; inserting it into Eq. (3.75) yields the expression for $\mathbb{Z}$ in the LARF [We shall suppress "$O(\varepsilon^2)$" hereafter]:

$$\begin{aligned}
\mathbb{Z} &= \mathcal{A}\Big(1+\frac{4i\varepsilon}{3}\Big)\Big[\tilde{r}^3+\frac{3\tilde{r}^2}{4}-\frac{9\tilde{r}}{16}-\frac{21}{64}+\frac{63}{256\tilde{r}}\Big] \\
&+ \mathcal{A}\Big[\frac{-945-236i\varepsilon}{5120\tilde{r}^2}+\frac{8505+15436i\varepsilon}{61440\tilde{r}^3}+O\Big(\frac{1}{\tilde{r}^4}\Big)\Big].
\end{aligned}$$

Inserting $\mathbb{Z}$ into Eqs. (3.70), (3.71), and (3.72) yields H_1, K, and H. Expanded in powers of $\tilde{r}$ and to first order in ε, these radial functions are given by

$$\begin{aligned}
H &= \frac{\mathcal{A}}{M}\Big[(3+4i\varepsilon)(\tilde{r}^2-\tilde{r})+\frac{i\varepsilon}{10\tilde{r}^3}+\frac{3i\varepsilon}{20\tilde{r}^4}\Big]+O\big(\tilde{r}^{-5}\big) \\
H_1 &= \frac{i\mathcal{A}\varepsilon}{4M}\Big[-8\tilde{r}^3-2\tilde{r}^2+4\tilde{r}+1 \\
&\qquad +\tilde{r}^{-1}+\tilde{r}^{-2}+\tilde{r}^{-3}+\tilde{r}^{-4}\Big]+O(\tilde{r}^{-5}) \\
K &= \frac{\mathcal{A}}{M}\Big[(3+4i\varepsilon)\Big(\tilde{r}^2-\frac{1}{2}\Big)+\frac{i\varepsilon}{10\tilde{r}^3} \\
&\qquad +\frac{i\varepsilon}{8\tilde{r}^4}+\frac{9i\varepsilon}{70\tilde{r}^5}+\frac{i\varepsilon}{8\tilde{r}^6}\Big]+O(\tilde{r}^{-7}). \qquad (3.77)
\end{aligned}$$

3.9 Appendix C: Time-independent perturbation equations

As is evident from the time-dependent perturbation theory, as $\omega \to 0$, H_1 goes to zero. In the static case, then, there are only two radial functions, $\hat{H}$ and $\hat{K}$ (where the hats signify that they represent the time-independent perturbations). Specializing to the axisymmetric case, the metric perturbation is

$$\begin{aligned}
h_{ab}^{(\ell 0)} = \mathrm{Diag}\Big[&(1-2M/r)\,\hat{H},\ \frac{\hat{H}}{1-2M/r}\ , \\
&r^2\hat{K},\ r^2\hat{K}\sin^2\theta\Big]\times Y^{\ell 0}(\theta,\phi).
\end{aligned}$$

The linearized Einstein equations governing $\hat{H}$ and $\hat{K}$ are given in Eqs. (9d) and (9e) of [26] with $H_1=0$ and $\omega=0$ ($k=0$ in Edelstein and Vishveshwara's notation):

$$\frac{d\hat{K}}{dr} = \frac{d\hat{H}}{dr}+\frac{2M}{r^2}\left(1-\frac{2M}{r}\right)^{-1}\hat{H}, \qquad (3.78)$$

$$\frac{2M}{r^2}\frac{d\hat{K}}{dr} = \left(1-\frac{2M}{r}\right)\frac{d^2\hat{H}}{dr^2}+\frac{2}{r}\frac{d\hat{H}}{dr}-\frac{\ell(\ell+1)}{r^2}\hat{H}. \qquad (3.79)$$

Eliminating $d\hat{K}/dr$ from these two equations, we can then write a single second-order differential equation for H in terms of the variable $z \equiv r/M - 1$ (same as Eq. (4.9) of [14]):

$$(1-z^2)\frac{d^2\hat{H}}{dz^2} - 2z\frac{d\hat{H}}{dz} + \left[\ell(\ell+1) - \frac{4}{1-z^2}\right]\hat{H} = 0.$$

This takes a form of the associated Legendre differential equation. The general solution for $\hat{H}$ is therefore

$$\hat{H} = \alpha_\ell P_\ell^2(r/M-1) + \beta_\ell Q_\ell^2(r/M-1). \tag{3.80}$$

With the general solution for $\hat{H}$, we can integrate Eq. (3.78) or (3.79) to find $\hat{K}$. For $\ell = 2$, we have

$$\begin{aligned}\hat{K}_2(r) &= \left[\alpha_2 P_2^1\left(r/M-1\right) + \beta_2 Q_2^1\left(r/M-1\right)\right] \\ &\quad \times \frac{2M}{\sqrt{r(r-2M)}} + \hat{H}_2(r).\end{aligned} \tag{3.81}$$

3.10 Appendix D: Newman-Penrose formalism

In this appendix, we summarize some equations of the Newman-Penrose formalism for our choice of tetrad. *In this Appendix and in Sec. 3.5 only*, we use ingoing Eddington-Finkelstein coordinates $(\tilde{V}, r, \theta, \phi)$ and a $(+\ -\ -\ -)$ signature of the metric.

3.10.1 Newman-Penrose quantities for Schwarzschild

We adopt the Hartle-Hawking null tetrad, which is given by Eqs. (4.2) of [15], together with the normalization conditions $\ell^\mu n_\mu = 1$ and $m^\mu \bar{m}_\mu = -1$. The tetrad vectors have components [using the notation $e^\mu = (e^{\tilde{V}}, e^r, e^\theta, e^\phi)$]

$$\ell^\mu = \left(1, \frac{1}{2} - \frac{M}{r}, 0, 0\right) \tag{3.82a}$$

$$n^\mu = (0, -1, 0, 0) \tag{3.82b}$$

$$m^\mu = \left(0, 0, \frac{1}{\sqrt{2}r}, \frac{i}{\sqrt{2}r\sin\theta}\right) \tag{3.82c}$$

$$\bar{m}^\mu = \left(0, 0, \frac{1}{\sqrt{2}r}, -\frac{i}{\sqrt{2}r\sin\theta}\right). \tag{3.82d}$$

Note that throughout this Appendix, an overbar denotes complex conjugation.

From these basis vectors, we define the direction derivatives

$$D = \ell^\mu \partial_\mu,\ \Delta = n^\mu \partial_\mu,\ \delta = m^\mu \partial_\mu \text{ and } \bar{\delta} = \bar{m}^\mu \partial_\mu. \tag{3.83}$$

Our conventions for the spin coefficients follow [15] [specifically, Eqs. (2.2) and (2.3)]. The spin coefficients are defined by

$$\begin{aligned}
\kappa &= \ell_{\mu;\nu} m^{\mu} \ell^{\nu} && (3.84a)\\
\pi &= -n_{\mu;\nu} \bar{m}^{\mu} \ell^{\nu} && (3.84b)\\
\rho &= \ell_{\mu;\nu} m^{\mu} \bar{m}^{\nu} && (3.84c)\\
\mu &= -n_{\mu;\nu} \bar{m}^{\mu} m^{\nu} && (3.84d)\\
\sigma &= \ell_{\mu;\nu} m^{\mu} m^{\nu} && (3.84e)\\
\lambda &= -n_{\mu;\nu} \bar{m}^{\mu} \bar{m}^{\nu} && (3.84f)\\
\epsilon &= \frac{1}{2}\left(\ell_{\mu;\nu} n^{\mu} \ell^{\nu} - m_{\mu;\nu} \bar{m}^{\mu} \ell^{\nu}\right). && (3.84g)\\
\alpha &= \frac{1}{2}\left(\ell_{\mu;\nu} n^{\mu} \bar{m}^{\nu} - m_{\mu;\nu} \bar{m}^{\mu} \bar{m}^{\nu}\right). && (3.84h)\\
\beta &= \frac{1}{2}\left(\ell_{\mu;\nu} n^{\mu} m^{\nu} - m_{\mu;\nu} \bar{m}^{\mu} m^{\nu}\right). && (3.84i)
\end{aligned}$$

The spin coefficients for the Schwarzschild spacetime are

$$\begin{aligned}
\kappa &= \sigma = \lambda = \nu = \tau = \pi = \gamma = 0 && (3.85a)\\
\epsilon &= \frac{M}{2r^2} && (3.85b)\\
\rho &= -\frac{r-2M}{2r^2} && (3.85c)\\
\mu &= -\frac{1}{r} && (3.85d)\\
\alpha &= -\beta = -\frac{1}{2\sqrt{2}r\tan\theta}. && (3.85e)
\end{aligned}$$

Because we are only interested in vacuum regions of spacetime, the Riemann and Weyl tensors are interchangeable. The Weyl components are defined in vacuum by

$$\begin{aligned}
\Psi_0 &= -R_{\alpha\beta\gamma\delta} \ell^{\alpha} m^{\beta} \ell^{\gamma} m^{\delta} && (3.86a)\\
\Psi_1 &= -R_{\alpha\beta\gamma\delta} \ell^{\alpha} n^{\beta} \ell^{\gamma} m^{\delta} && (3.86b)\\
\Psi_2 &= -\frac{1}{2} R_{\alpha\beta\gamma\delta}\left(\ell^{\alpha} n^{\beta} \ell^{\gamma} n^{\delta} + \ell^{\alpha} n^{\beta} m^{\gamma} \bar{m}^{\delta}\right) && (3.86c)\\
\Psi_3 &= -R_{\alpha\beta\gamma\delta} \ell^{\alpha} n^{\beta} \bar{m}^{\gamma} n^{\delta} && (3.86d)\\
\Psi_4 &= -R_{\alpha\beta\gamma\delta} n^{\alpha} \bar{m}^{\beta} n^{\gamma} \bar{m}^{\delta}. && (3.86e)
\end{aligned}$$

Their values for the Schwarzschild spacetime are

$$\Psi_0 = \Psi_1 = \Psi_3 = \Psi_4 = 0, \tag{3.87a}$$

$$\Psi_2 = -\frac{M}{r^3}. \tag{3.87b}$$

The Ricci identities are

$$\left(\nabla_\mu \nabla_\nu - \nabla_\nu \nabla_\mu\right) e_\gamma = R_{\sigma\gamma\mu\nu} e^\sigma. \tag{3.88}$$

Inserting the null tetrad vectors for e^σ and projecting along the tetrad yields the Ricci identities in Newman-Penrose notation. One of these equations is, in our tetrad and evaluated on the horizon,

$$D\sigma^{(1)} - 2\epsilon\sigma^{(1)} = \partial_{\tilde{V}}\sigma^{(1)} - 2\epsilon\sigma^{(1)} = \Psi_0^{(1)}. \tag{3.89}$$

(Note that we have used the fact that σ and Ψ_0 vanish for Schwarzschild.) This is the *tidal force equation*; it relates $\Psi_0^{(1)}$, which is physically equivalent to the tangential-tangential component of the perturbing tidal field on the horizon, to σ, which is physically equivalent to the shear of the instantaneous horizon.

The shape of the perturbed instantaneous horizon is determined by its two-dimensional scalar curvature $\mathscr{R} + \mathscr{R}^{(1)}$ where $\mathscr{R}$ is the curvature of the unperturbed horizon. According to the tidal force equation (3.89), $\Psi_0^{(1)}$ drives the shear, which is the "rate of change of the shape" of the horizon as measured by fiducial observers on the horizon [22]. Thus, it is not surprising that $\mathscr{R}^{(1)}$ can be computed directly from $\Psi_0^{(1)}$. Hartle [15] has derived the explicit formula, a consequence of Gauss' relation [36], in the Newman-Penrose formalism with the present choice of coordinates and tetrad:

$$\mathscr{R}^{(1)} = -4\mathrm{Im}\left[\frac{(\bar{\delta} + 2\pi - 2\alpha)(\bar{\delta} + \pi - 4\alpha) + 2\epsilon\lambda}{\omega(i\omega + 2\epsilon)}\right]\Psi_0^{(1)} \tag{3.90}$$

where ω is the frequency of the perturbation. When a Schwarzschild black hole is perturbed by a distant moon in a slow, circular, orbit with angular velocity Ω, then $\omega = 2\Omega$.

3.10.2 Newman-Penrose quantities for Kerr

Finally, to facilitate our comparison to Hartle's results, we here list the relevant Newman-Penrose quantities for the Kerr spacetime [Eq. (3.54)] using Hartle's choice [15] of coordinates and tetrad. In the limit $a = 0$, Hartle's tetrad and spin coefficients reduce to those listed in the previous subsection.

The null tetrad vectors [using the notation $e^\mu = (e^{\tilde{V}}, e^r, e^\theta, e^{\tilde{\phi}})$] are

$$\begin{aligned}
\ell^\mu &= \left(1, \frac{r^2 - 2Mr + a^2}{2\left(r^2 + a^2\right)}, 0, \frac{a}{r^2 + a^2}\right) && \text{(3.91a)}\\
n^\mu &= \left(0, -\frac{2(a^2 + r^2)}{2r^2 + a^2 + a^2 \cos 2\theta}, 0, 0\right)\\
&\quad + \frac{-a^2 + a^2 \cos 2\theta}{2\left(a^2 + 2r^2 + a^2 \cos 2\theta\right)} \ell^\mu\\
&\quad + \frac{-a \sin\theta}{\sqrt{2}\left(ir + a\cos\theta\right)} m^\mu\\
&\quad + \frac{-a \sin\theta}{\sqrt{2}\left(-ir + a\cos\theta\right)} \bar{m}^\mu && \text{(3.91b)}\\
m^\mu &= \left(0, -\frac{a \sin\theta \left(r^2 - 2Mr + a^2\right)}{2\sqrt{2}\left(r^2 + a^2\right)\left(-ir + a\cos\theta\right)},\right.\\
&\qquad \left.\frac{1}{\sqrt{2}\left(r + ia\cos\theta\right)}, \frac{\left(ir + a\cos\theta\right)\csc\theta}{\sqrt{2}\left(r^2 + a^2\right)}\right) && \text{(3.91c)}\\
\bar{m}^\mu &= \left(0, -\frac{a \sin\theta \left(r^2 - 2Mr + a^2\right)}{2\sqrt{2}\left(r^2 + a^2\right)\left(ir + a\cos\theta\right)},\right.\\
&\qquad \left.\frac{1}{\sqrt{2}\left(r - ia\cos\theta\right)}, \frac{\left(-ir + a\cos\theta\right)\csc\theta}{\sqrt{2}\left(r^2 + a^2\right)}\right). && \text{(3.91d)}
\end{aligned}$$

Then, one can compute the spin coefficients for this tetrad from Eqs. (3.84a)–(3.84i):

$$\begin{aligned}
\kappa &= \sigma = 0 && \text{(3.92a)}\\
\lambda &= O(a^2) && \text{(3.92b)}\\
\nu &= O(a^2) && \text{(3.92c)}\\
\tau &= \frac{-i(2M + r)\sin\theta a}{2\sqrt{2}r^3} && \text{(3.92d)}\\
\pi &= \frac{i(4M + r)\sin\theta a}{2\sqrt{2}r^3} && \text{(3.92e)}\\
\gamma &= \frac{-i\cos\theta a}{2r^2} + O(a^2) && \text{(3.92f)}\\
\epsilon &= \frac{M}{2}\frac{r^2 - a^2}{\left(r^2 + a^2\right)^2} = \frac{M}{2r^2} + O(a^2) && \text{(3.92g)}
\end{aligned}$$

$$\begin{aligned} \rho &= -\frac{r-2M}{2r^2} - \frac{i(r-2M)\cos\theta a}{2r^3} \\ &\quad +O(a^2) \end{aligned} \tag{3.92h}$$

$$\mu = -\frac{1}{r} + O(a^2) \tag{3.92i}$$

$$\begin{aligned} \alpha &= \frac{-\cot\theta}{2\sqrt{2}r} - \frac{i[-3M+(2M+2r)\cos 2\theta]a}{4\sqrt{2}r^3\sin\theta} \\ &\quad +O(a^2) \end{aligned} \tag{3.92j}$$

$$\begin{aligned} \beta &= \frac{\cot\theta}{2\sqrt{2}r} - \frac{i[M+r+(r-M)\cos 2\theta]a}{4\sqrt{2}r^3\sin\theta} \\ &\quad +O(a^2). \end{aligned} \tag{3.92k}$$

The directional derivatives are then given by Eq. (3.83).

Using the Kerr metric [Eq. (3.54)] and Hartle's choice for the tetrad [Eqs. (3.91a)–(3.91d)], one can compute the curvature for Kerr and read off the curvature scalars via Eqs. (3.86a)–(3.86e):

$$\Psi_0 = \Psi_1 = 0 \tag{3.93a}$$

$$\Psi_2 = -\frac{M}{(r-ia\cos\theta)^3} \tag{3.93b}$$

$$\Psi_3 = -\frac{3iaM\sin\theta}{\sqrt{2}\,(r-ia\cos\theta)^4} \tag{3.93c}$$

$$\Psi_4 = \frac{3ia^2M\sin^2\theta}{(ir+a\cos\theta)^5}. \tag{3.93d}$$

The tidal force equation (3.89) relates $\Psi_0^{(1)}$ to $\sigma^{(1)}$. The correction to the scalar curvature of the horizon, $\mathscr{R}^{(1)}$, is given by Eq. (3.90).

For a stationary moon perturbing a slowly rotating Kerr black hole, the frequency of the perturbation is $\omega = -2\Omega_H = -8M^2\Omega_H$.

3.11 Bibliography

[1] A. Abramovici et al., Science **256**, 325 (1992).

[2] K. S. Thorne, in *Proceedings of the Snowmass 94 Summer Study on Particle and Nuclear Astrophysics and Cosmology*, E. Kolb and R. Peccei, Eds., (World Scientific, Singapore, 1995), p. 398, http://xxx.lanl.gov/abs/gr-qc/9506086.

[3] F. D. Ryan, Phys. Rev. D **52**, 5707 (1995).

[4] The word "bothrodesy" was coined by Sterl Phinney, and he first used it in a seminar at Caltech on June 8, 2001.

[5] E. S. Phinney, *LISA Science Requirements*, Presentation to the LISA International Science Team [LIST], 12 December 2001, URL `http://www.tapir.caltech.edu/~listwg1/`.

[6] J. R. Gair et al., Class. Quantum Grav. **21**, S1595 (2004).

[7] J. R. Gair et al., in *GW-DAW proceedings* (2004), URL `http://arxiv.org/abs/gr-qc/0405137`.

[8] L. S. Finn and K. S. Thorne, Phys. Rev. D **62**, 124021 (2000).

[9] K. S. Thorne, in *The Future of Theoretical Physics and Cosmology*, G. Gibbons, E. P. S. Shellard, and S. J. Rankin, Eds., (Cambridge University Press, 2003), Ch. 5.

[10] K. S. Thorne, private communication.

[11] M. Colpi, S. L. Shapiro, and I. Wasserman, Phys. Rev. Lett. **57**, 2485 (1986).

[12] F. D. Ryan, Phys. Rev. D **55**, 6081 (1996).

[13] T. D. Lee and Y. Pang, Phys. Rev. D **35**, 3637 (1987).

[14] J. B. Hartle, Phys. Rev. D **8**, 1010 (1973).

[15] J. B. Hartle, Phys. Rev. D **9**, 2749 (1974).

[16] S. A. Teukolsky, Phys. Rev. Lett. **29**, 1114 (1972).

[17] G. H. Darwin, Philos. Trans. R. Soc. (Pt. I) **170**, 1 (1879).

[18] K. S. Thorne and J. B. Hartle, Phys. Rev. D **31**, 1815 (1985).

[19] W. M. Suen, Phys. Rev. D **34**, 3633 (1986).

[20] We follow the same notation as in [23].

[21] E. Poisson, Phys. Rev. D **70**, 084044 (2004).

[22] K. S. Thorne, R. Price, and D. MacDonald, *Black Holes: The Membrane Paradigm.* (Yale University Press, New Haven, 1986).

[23] K. S. Thorne, Rev. Mod. Phys. **52**, 299 (1980).

[24] T. Regge and J. A. Wheeler, Phys. Rev. **108**, 1063 (1957).

[25] F. J. Zerilli, Phys. Rev. D **2**, 2141 (1970).

[26] L. Edelstein and C. V. Vishveshwara, Phys. Rev. D **1**, 3514 (1970).

[27] E. Poisson and M. Sasaki, Phys. Rev. D **51**, 5753 (1995).

[28] A. Erdélyi et al., *Higher Transcendental Functions*, Vol. I (McGraw-Hill, New York, 1953).

[29] X.-H. Zhang, Phys. Rev. D **31**, 3130 (1985).

[30] C. Misner, K. S. Thorne, and J. A. Wheeler, *Gravitation* (W. H. Freeman and Company, New York, 1973).

[31] W. M. Suen, Phys. Rev. D **34**, 3617 (1986).

[32] E. Newman and R. Penrose, J. Math. Phys. **3**, 566 (1962).

[33] S. Chandrasekhar, *The Mathematical Theory of Black Holes* (Oxford University Press, Oxford, 1985).

[34] R. H. Price and K. S. Thorne, Phys. Rev. D **33**, 915 (1986).

[35] S. Teukolsky, Ph.D. thesis, California Institute of Technology (1973).

[36] S. Kobayashi and K. Nomizu, *Foundations of Differential Geometry*, Vol. II (Interscience, New York, 1963).

Chapter 4

A generalization of Ryan's theorem: probing tidal coupling with gravitational waves from nearly circular, nearly equatorial, extreme-mass-ratio inspirals

Extreme-mass-ratio inspirals (EMRIs) and intermediate-mass-ratio inspirals (IMRIs)—binaries in which a stellar-mass object spirals into a massive black hole or other massive, compact body—are important sources of gravitational waves for LISA and LIGO, respectively. Thorne has speculated that the waves from EMRIs and IMRIs encode, in principle, all the details of (i) the central body's spacetime geometry (metric), (ii) the tidal coupling (energy and angular momentum exchange) between the central body and orbiting object, and (iii) the evolving orbital elements. Fintan Ryan has given a first partial proof that this speculation is correct: Restricting himself to nearly circular, nearly equatorial orbits and ignoring tidal coupling, Ryan proved that the central body's metric is encoded in the waves. In this paper we generalize Ryan's theorem. Retaining Ryan's restriction to nearly circular and nearly equatorial orbits, and dropping the assumption of no tidal coupling, we prove that Thorne's conjecture is nearly fully correct: the waves encode not only the central body's metric but also the evolving orbital elements and (in a sense slightly different from Thorne's conjecture) the evolving tidal coupling.

Originally published as C. Li and G. Lovelace, submitted to Phys. Rev. D (2007), preprint available online at `http://arxiv.org/abs/gr-qc/0702146`.

4.1 Introduction and summary

The LIGO-GEO-VIRGO-TAMA network of broadband ground-based laser interferometers, aimed at detecting gravitational waves in the high-frequency band 10–10^4 Hz, is already operating at or near its initial design sensitivities. In the next decade, LISA (the Laser Interferometer Space Antenna) will open up the low-frequency gravitational-wave window (10^{-4}–0.1 Hz).

Among the most important sources of gravitational waves for LISA are extreme-mass-ratio inspirals (EMRIs), which are systems in which a small object (with mass $\mu \sim M_\odot$) orbits a supermassive black hole or other central body (boson star [1, 2] or soliton star [3] or naked singularity or ...) with mass $M \sim 10^6 M_\odot$. Recently, Brown and collaborators [4] have estimated that advanced detectors in LIGO (the Laser Interferometric Gravitational-Wave Observatory) may detect up to $\sim$ 10–30yr^{-1} *intermediate mass ratio inspirals* (IMRIs), which are analogous to EMRIs but have less massive central bodies (masses M in the range of $\sim 10^2$–$10^4 M_\odot$).

Thorne has conjectured[1] that the waves from an EMRI or IMRI contain, encoded in themselves (at least in principle): (i) the spacetime geometry (metric) of the massive central body, (ii) the tidal coupling (evolving rate of energy and angular momentum exchange) between the orbiting object and the central body, and (iii) the evolving orbital elements. This conjecture (which has been partially proved; see below) has motivated placing EMRIs high on LISA's list of target sources [8], and has motivated research to: (a) prove Thorne's conjecture with the widest generality possible, or, if it is false, determine what information actually *is* encoded in the EMRI and IMRI waves [4, 9]; (b) develop data analysis techniques for searching for EMRI and IMRI waves in LISA [10, 11] and LIGO [12] data; (c) scope out the accuracy with which LISA and LIGO can extract the encoded information from EMRI and IMRI waves (and if the central body appears to be a black hole, the accuracy with which its properties agree with those of a hole) [13, 14]; and (d) develop data analysis techniques for extracting the waves' information [15].

Fintan Ryan [6] has proved a theorem that is an important step toward verifying Thorne's conjecture. Specifically, he has proved that it is possible in principle to recover the full spacetime geometry from EMRI waves under the following assumptions: i) the central body is general-relativistic, stationary, axisymmetric, reflection-symmetric, and asymptotically-flat (SARSAF), ii) the small object travels on a nearly circular and nearly equatorial orbit, and iii) there is no tidal coupling. Moreover, Ryan has shown that the multipole moments that determine the spacetime geometry are *redundantly* encoded in the gravitational waves and can be extracted using *either* of the two precession

---

[1] Thorne's conjecture has grown over time. Originally, in the early 1990s, he conjectured (or, more precisely, asserted!) that the waves encode "a portion" of the spacetime geometry (e.g., p. 326 of [5]). By 1994, when Fintan Ryan proved his theorem, Thorne was arguing that the entire spacetime geometry would be encoded (see, e.g., the introduction to Ryan's paper [6]). In 2002, when thinking about how LISA might test the laws of black-hole physics, Thorne realized that the tidal coupling might also be encoded along with the central body's spacetime geometry; see [7]. Only recently, when advising the authors about their research, did Thorne realize that the evolving orbital elements might also be extractable (private communication).

frequencies (about a circular orbit and about the equatorial plane) *or* the waves' phase evolution.

The purpose of this paper is to generalize Ryan's theorem. We retain assumptions (i) and (ii) (SARSAF spacetime and nearly circular, nearly equatorial orbit) but relax assumption (iii) by allowing for a small amount of tidal coupling. We show that in this case, Thorne's conjecture is nearly correct: the waves encode not only the central body's metric but also the evolving orbital elements and (in a sense slightly different from Thorne's conjecture) the evolving tidal coupling. (Assumption (ii), that the orbit is nearly circular and nearly equatorial, is relaxed in a companion paper by Li [9]). Assumption (i) has been generalized to the case of electrovacuum spacetimes in [16].

Motivated by the result of Fang and Lovelace [17] that the only unambiguous part of the tidal coupling is the time-dependent, dissipative portion (at least when the central body is a non-spinning black hole and the orbit is large and circular), we characterize the tidal coupling by the rates of energy and angular momentum exchange between the central body and the orbiting object, $\dot{E}_{\rm body}$ and $\dot{L}_{\rm body}$. (Throughout this paper, a dot means derivative with respect to the coordinate time t, which is the time measured by an inertial observer in the asymptotically flat region of the spacetime.) Actually, we only need to consider $\dot{E}_{\rm body}$, because once it is known, $\dot{L}_{\rm body}$ can be deduced from the standard energy-angular momentum relation for circular orbits and their influence on waves and tides, $\dot{E} = \Omega_{\rm orbit}\dot{L}$. (Here $\Omega_{\rm orbit}$ is the orbital angular velocity, which is the same as the waves' observed primary angular frequency aside from a factor 2.)

This paper is organized as follows: In Sec. 4.2, we begin by noting that, when there is a small amount of tidal coupling (as we assume), then the redundancy in Ryan's analysis is broken. One can still use Ryan's algorithm for the precession frequencies to recover the central body's spacetime geometry. Then, by making use of the observed (time-independent) spacetime geometry and the measured, evolving amplitudes associated with the precession frequencies, one can also recover from the EMRI waves the evolving orbital parameters. Having relied on non-dissipative aspects of the waves to deduce the spacetime geometry and orbit, one can then—as we show in Sec. 4.3—use the waves' dissipation-induced phase evolution to deduce the tidal coupling.

In our somewhat delicate discussion of deducing the tidal coupling (Sec. 4.3), we begin by noting that the sum of the power radiated to infinity and the power fed into the central body via tidal coupling, $\dot{E}_{\rm total} = \dot{E}_\infty + \dot{E}_{\rm body}$ is equal to the power lost from the orbit, which can be deduced from the waves' observed phase evolution. The central body influences this observed $\dot{E}_{\rm total}$ in two ways: (i) by generating a nonzero $\dot{E}_{\rm body}$, the quantity that interests us, and (ii) by very slightly altering $\dot{E}_\infty$. To help quantify these two body influences, in Sec. 4.3.2 we show how one can deduce, from the observations, the rate $\dot{E}_{\infty{\rm NBI}}$ that energy would be radiated to infinity if there were *no body influences*. The difference between the measured $\dot{E}_{\rm total}$ and the deduced $\dot{E}_{\infty{\rm NBI}}$ is the influence of the body's structure on the total energy loss from the orbit, $\dot{E}_{\rm total,BI} \equiv \dot{E}_{\rm total} - \dot{E}_{\infty{\rm NBI}}$. This measured/deduced body influence on the total energy loss consists of two tiny pieces: the power that actually goes into the body via tidal coupling, $\dot{E}_{\rm body}$, and the body's tiny influence on the power radiated to infinity, $\dot{E}_{\infty\rm BI} \equiv \dot{E}_\infty - \dot{E}_{\infty\rm NBI}$:

$$\dot{E}_{\rm total,BI} \equiv \dot{E}_{\infty\rm BI} + \dot{E}_{\rm body}\ . \tag{4.1}$$

In principle (as described above), from the observational data plus general-relativity theory we know the body's influence on the total energy loss $\dot{E}_{\rm total,BI}$ with complete precision. This is not quite what Thorne conjectured, but it is close, and it is the only complete-precision statement we have been able to make about measuring the influence of tidal coupling.

Thorne conjectured we could deduce $\dot{E}_{\rm body}$ from the observed waves. This, in fact appears not to be possible (in principle) with complete precision. However, we argue in Sec. 4.3.3 and the Appendix that, if the central body is highly compact, then the unknown $\dot{E}_{\infty\rm BI}$ will be smaller than $\dot{E}_{\rm body}$ by $\sim v^n \ll 1$, where v is the orbital velocity and n is some high power; and we show that, when the body's external metric is that of Schwarzschild or Kerr, then $n = 5$. As a result, aside from a very small $O(v^n)$ uncertainty due to the influence of the body on the energy radiated to infinity, the tidal coupling power $\dot{E}_{\rm body}$ is equal to the known influence of the body on the total energy loss $\dot{E}_{\rm total,BI}$.

A brief conclusion is made in Sec. 4.4.

4.2 Extracting the spacetime geometry and orbital elements

Aside from allowing tidal coupling, we treat the same class of EMRIs as did Ryan:

First, we assume the central body's exterior spacetime is a vacuum, stationary, axisymmetric, reflection symmetric, and and asymptotic flat (SARSAF) solution of Einstein's equations. The exterior spacetime metric can be written as (e.g., Eq. (7.1.22) of [18])

$$ds^2 = -F(dt - \omega d\phi)^2 + \frac{1}{F}[e^{2\gamma}(d\rho^2 + dz^2) + \rho^2 d\phi^2], \tag{4.2}$$

where F, ω and γ are functions of ρ and $|z|$. In SARSAF spacetimes, there is a one-to-one correspondence between the spacetime metric and a series of scalar multipole moments $(M_{2i}, S_{2i+1}),\quad i = 0, 1, \cdots$ [19, 20]. Here $M_0 \equiv M$ is the mass of the central body, S_1 is its spin, M_2 is its mass quadrupole moment, etc. To extract the geometry of the spacetime surrounding the central body, it is sufficient to extract the multipole moments $\{M_\ell, S_\ell\}$ [6].

Second, we let a small object with mass $\mu \ll M$ move about the central body in a nearly circular, nearly equatorial orbit.

For precisely circular, equatorial, geodesic motion, the waves obviously have a single fundamental frequency Ω_ϕ that is associated with the circular motion $\phi = \Omega_\phi t$. When the geodesic orbit is slightly nonradial, it is easy to show that its radius ρ undergoes periodic motion with some angular frequency

Ω_ρ; and when slightly nonequatorial, its vertical coordinate z undergoes periodic motion with another angular frequency Ω_z. These geodesic motions give rise to gravitational waves that are triperiodic: a discrete spectrum with frequencies equal to Ω_ϕ, Ω_ρ, Ω_z, and their sums and differences (see [9] for a proof, patterned after the proof by Drasco and Hughes [21] for the Kerr metric). The frequency difference $\Omega_\rho - \Omega_\phi$ shows up as an orbital periapsis precession, and $\Omega_z - \Omega_\phi$ as an orbital plane precession; these precessions produce corresponding modulations of the gravitational waveforms.

In our case, the orbits are not geodesics; they evolve due to gravitational radiation reaction. Because of the extreme mass ratio, the radiation reaction can be described by the adiabatic approximation. In this approximation, on the timescale of an orbital period, the small object moves very nearly along a geodesic of the central body's gravitational field. On a timescale much larger than the orbital period, the object moves from one geodesic to another as it loses energy and angular momentum to gravitational radiation. It follows that the three frequencies $\{\Omega_\phi(t), \Omega_\rho(t), \Omega_z(t)\}$ each evolve with time on the radiation reaction timescale, which is much longer than the orbital periods.

In principle, a large amount of information can be encoded in the time evolution of the waves' three fundamental frequencies $\{\Omega_\phi(t), \Omega_\rho(t), \Omega_z(t)\}$ and the complex amplitudes (amplitudes and phases) of the various spectral components. The largest amplitudes are likely to be those for the second harmonic of Ω_ϕ and for the two precessions, $h_{2\Omega_\phi}(t)$, $h_{\Omega_\rho-\Omega_\phi}(t)$, and $h_{\Omega_\rho-\Omega_z}(t)$. We shall call these the primary-frequency component, and the precessional components of the waves. To simplify our prose, we shall refer to Ω_ρ and Ω_z as the "precession frequencies" even though the actual frequencies of precession are $\Omega_\rho - \Omega_\phi$ and $\Omega_z - \Omega_\phi$.

Thorne's conjecture can be expressed mathematically as the claim that these time-evolving frequencies and amplitudes encode fully and separably,

1. The values of all the central body's multipole moments $\{M_\ell, S_\ell\}$,
2. The rates $\dot{E}_{\rm body}$ and $\dot{L}_{\rm body}$ at which the orbiting object's tidal pull deposits energy and angular momentum into the central body, and
3. The time-evolving orbital elements, i.e., the orbit's semi-latus rectum $p(t)$, eccentricity $e(t)$, and inclination angle $\iota(t)$.

Ryan's theorem [6] states that, if there is no tidal coupling, then all the SARSAF moments $\{M_{2i}, S_{2i+1}\}$ are encoded in the time evolving frequencies fully, separably, and redundantly. Ryan did not explicitly address the encoding of the three orbital elements $p(t)$, $e(t)$ and $\iota(t)$. However, their encoding is an almost trivial extension of his analysis:

Specifically, Ryan noticed that the three fundamental frequencies are independent of e and ι to first order in these small quantities, i.e., they are functions solely of the moments and the semi-latus rectum p. One can eliminate p by regarding the precession frequencies Ω_z and Ω_ρ as functions of the moments and Ω_ϕ, or equivalently as functions of the moments and the Post-Newtonian (PN) expansion parameter $v \equiv (M\Omega_\phi)^{1/3} \simeq$ (orbital velocity). Expanding $\Omega_z(v; S_\ell, M_\ell)$ and $\Omega_\rho(v; S_\ell, M_\ell)$ in powers of v, Ryan found the following pattern of coefficients (with each moment first appearing at a different power of v), from which all the moments can be extracted separably (Eqs. (18)–(19) of [6]):

$$\begin{aligned} \frac{\Omega_\rho}{\Omega_\phi} &= 3v^2 - 4\frac{S_1}{M^2}v^3 + \left(\frac{9}{2} - \frac{3M_2}{2M^3}\right)v^4 + \cdots \\ \frac{\Omega_z}{\Omega_\phi} &= 2\frac{S_1}{M^2}v^3 + \frac{3M_2}{2M^3}v^4 + \cdots . \end{aligned} \tag{4.3}$$

This result leads to Ryan's algorithm for extracting information. First, from the waves' observed time-evolving precession frequencies and time-evolving primary frequency, one can deduce the functions $\Omega_{z,\rho}(\Omega_\phi)$ and thence $\Omega_{z,\rho}(v)$; second, expanding in powers of v, one can then read out the multipole moments $\{M_\ell, S_\ell\}$ from either $\Omega_z(v)$ or $\Omega_\rho(v)$.

We almost trivially augment onto Ryan's algorithm the following steps for extracting the time-evolving orbital elements: Third, knowing the moments and thence the metric, one can use the geodesic equation to deduce $p(t)$ from $\Omega_\phi(t)$. Fourth, one can use wave-generation theory and knowledge of the metric to deduce $e(t)$ and $\iota(t)$ from the amplitudes $h_{\Omega_\rho - \Omega_\phi}$ and $h_{\Omega_z - \Omega_\phi}$ of the wave modulations due to periapse precession and orbital plane precession.

4.3 Probing tidal coupling

We now drop Ryan's restriction of no tidal coupling. This does not alter Eqs. (4.3) for Ω_ρ and Ω_z as functions of v, i.e., of the orbital frequency Ω_ϕ, since all three frequencies only depend on the geodesic motion and hence only depend on the multipole moments $\{M_\ell, S_\ell\}$. On the other hand, the evolution of the frequencies, as functions of time, *will* depend on the tidal coupling.

More generally, we can divide the physical quantities of our analysis into two categories: i) "static": those quantities related to the geodesic motion of the orbiting object, and ii) "dynamic": those quantities related to the inspiral of the object (i.e., to the evolving rate at which the object moves from geodesic to geodesic). All static quantities are independent of tidal coupling and all dynamic quantities depend on it.

This suggests that Ryan's analysis can be extended to include tidal coupling. First, the static quantities can be used to deduce the the central body's multipole moments, just as in Ryan's original argument as sketched above. Then, the dynamic quantities, combined with knowledge of the spacetime metric, can be used to extract tidal-coupling information. This extension is discussed in the following subsections.

4.3.1 The phase evolution when tidal coupling is neglected

Following Ryan, we characterize the phase evolution of EMRI waves by the number of primary-frequency cycles of waves per logarithmic frequency interval, as a function of the primary waves' slowly increasing frequency $f = \Omega_\phi/\pi$. This quantity can be written as (Eq. (4) of [6])

$$\Delta N(f) \equiv \frac{f\,dt}{d\ln f} = \frac{f^2}{df/dt}. \tag{4.4}$$

This phase evolution $\Delta N(f)$ can be measured by gravitational-wave detectors with high precision.

If there is no tidal coupling *and* no other influence of the structure of the central body on the waves, as Ryan assumed, then it is possible to read off the multipole moments (and also the small object's mass[2]) from a PN expansion of $\Delta N(f)$ (Eq. (57) of [6]):

$$\begin{aligned}\Delta N_{\rm NBI} = \frac{5}{96\pi}\left(\frac{M}{\mu}\right) v^{-5}\Bigg[& 1 + \frac{743}{336}v^2 - 4\pi|v|^3 \\ & + \frac{113}{12}\frac{S_1}{M^2}v^3 + \left(\frac{3058673}{1016064} - \frac{1}{16}\frac{S_1^2}{M^4} + 5\frac{M_2}{M^3}\right)v^4 \\ & + \sum_{\ell=4,6,\ldots} \frac{(-1)^{\ell/2}(4\ell+2)(\ell+1)!!\,[M_\ell + \mathrm{TNILM}]\,v^{2\ell}}{3\ell!!M^{\ell+1}} \\ & + \sum_{\ell=3,5,\ldots} \frac{(-1)^{(\ell-1)/2}(8\ell+20)\ell!!\,[S_\ell + \mathrm{TNILM}]\,v^{2\ell+1}}{3(\ell-1)!!M^{\ell+1}}\Bigg].\end{aligned} \tag{4.5}$$

Here "NBI" stands for *no body influence* and "TNILM" stands for *terms nonlinear in lower moments.* [Recall that $v = (M\Omega_\phi)^{1/3} = (\pi M f)^{1/3}$.] So long as tidal coupling is negligible, then, the spacetime multipole moments can be determined redundantly from *either* $\Delta N(f)$ [Eq. (4.5)] *or* the periapse precession frequency $\Omega_\rho(\Omega_\phi)$ *or* the orbital-plane precession frequency $\Omega_z(\Omega_\phi)$ [Eqs. (4.3)].

4.3.2 Tidal coupling and the phase evolution

When tidal coupling effects are included, the redundancy is broken. The multipole moments $\{M_\ell, S_\ell\}$ can still [Eq. (4.3)] be determined from $\Omega_{\rho,z}(\Omega_\phi)$, while (as the following discussion shows), the tidal coupling can be determined from $\{M_\ell, S_\ell\}$ and $\Delta N(f)$.

As a preliminary to discussing this, we explain why it is sufficient, in analyzing tidal coupling, to focus on energy exchange between the orbit, the body and the waves, and ignore angular momentum exchange. Since the body is in a (nearly) circular, geodesic orbit, changes in its orbital energy and

---

[2] The mass of the small object can be determined from $\Delta N(f)$ *even when there is tidal coupling.* The leading-PN-order part of the energy flux (equivalently, the leading-PN-order part of $\Delta N(f)$) is independent of tidal coupling. One can thus equate the leading-PN-order parts of $\Delta N(f)$ and $\Delta N_{\rm NBI}$ [Eq. (4.5)]. After inserting the mass M (obtained from one of the precession frequencies), one can solve for μ. The precession frequencies, in contrast, are independent of μ [Eq. (4.3)].

angular momentum are related by

$$\dot{E}_{\rm orbit} = \Omega_\phi \, \dot{L}_{\rm orbit}, \tag{4.6a}$$

aside from second-order corrections due to the slight orbital ellipticity and inclination angle. Our entire analysis is restricted to first-order corrections, so those second-order corrections are negligible. Similarly, since the energy and angular momentum radiated to infinity are carried by the primary waves, with angular frequency $\omega = 2\pi f = 2\Omega_\phi$ (aside from negligible contributions from the precessions, which are second order in the ellipticity and inclination), each graviton carries an energy $\hbar\omega = 2\hbar\Omega_\phi$ and an angular momentum $2\hbar$ (with this last 2 being the graviton spin). Therefore, the energy and angular momentum radiated to infinity are related by

$$\dot{E}_\infty = \Omega_\phi \, \dot{L}_\infty. \tag{4.6b}$$

Conservation of energy and of angular momentum, together with Eqs. (4.6a) and (4.6b), then imply that

$$\dot{E}_{\rm body} = \Omega_\phi \, \dot{L}_{\rm body}, \tag{4.6c}$$

for the energy and angular momentum deposited in the body by tidal coupling. Eq. (4.6) implies that, once we understand, observationally, the energy exchange, an understanding of the angular momentum exchange will follow immediately.

Now turn to the influence of the body's internal structure on the observed energy exchange.

The total rate that energy is lost from the orbit (which then goes to infinity and the body) is related to the phase evolution $\Delta N(f)$ by

$$\dot{E}_{\rm total} = -\dot{E}_{\rm orbit} = -\frac{dE_{\rm orbit}}{df}\frac{df}{dt} = -f^2 \frac{dE_{\rm orbit}}{df}\frac{1}{\Delta N}. \tag{4.7}$$

The phase evolution ΔN and the primary frequency f are known from observation, and, after using the precession frequencies to compute the spacetime metric (Sec. 4.2), it is possible to compute $dE_{\rm orbit}/df$ via the geodesic equation[3]. Thus everything on the right-hand side of Eq. (4.7) can be determined from observed quantities, which means that $\dot{E}_{\rm total}$ is measurable.

Another measurable quantity, we claim, is the rate that energy would be lost from the orbit if

---

[3] To do this, first insert the multipole moments $\{M_\ell, S_\ell\}$ into the geodesic equation. Then, solve the geodesic equation for the family of circular, equatorial orbits about the central body. Each orbit i will have a particular value of energy $E_{{\rm orbit},i}$ and frequency f_i; this one-to-one mapping between $E_{\rm orbit}$ and f can then be used to compute $dE_{\rm orbit}/df$.

the body's structure had no influence. This quantity is [by analogy with Eq. (4.7)]

$$\dot{E}_{\mathrm{total,NBI}} = -f^2 \frac{dE_{\mathrm{orbit}}}{df} \frac{1}{\Delta N_{\mathrm{NBI}}}. \tag{4.8}$$

Knowing the moments as a function of frequency from measurements of the precessions, ΔN_{NBI} can be computed from the moments via Ryan's phasing relation[4] (4.5), and, as we have seen, dE_{orbit}/df can also be computed from the observations; so $\dot{E}_{\mathrm{total,NBI}}$ is, indeed, observable, as claimed. Therefore the influence of the body's structure on the orbit's total energy loss

$$\dot{E}_{\mathrm{total,BI}} = \dot{E}_{\mathrm{total}} - \dot{E}_{\mathrm{total,NBI}} \tag{4.9}$$

is also observable.

This body influence on the total energy loss consists of two parts: the energy that goes into the body via tidal coupling, $\dot{E}_{\mathrm{body}}$, and a tiny body-influenced modification of the rate that the waves carry energy to infinity

$$\dot{E}_{\mathrm{total,BI}} = \dot{E}_{\mathrm{body}} + \dot{E}_{\infty \mathrm{BI}} \ , \tag{4.10}$$

where

$$\dot{E}_{\infty \mathrm{BI}} = \dot{E}_{\infty} - \dot{E}_{\mathrm{total,NBI}} \ . \tag{4.11}$$

Thorne conjectured that the energy exchange due to tidal coupling, $\dot{E}_{\mathrm{body}}$, would be observable. We doubt very much that it is, since in general we see no way to determine the relative contributions of $\dot{E}_{\mathrm{body}}$ and $\dot{E}_{\infty \mathrm{BI}}$ to the observed total body influence $\dot{E}_{\mathrm{total,BI}}$. The best one can do, in general, in validating Thorne's conjecture, is to extract the central body's total influence on the orbital energy loss, $\dot{E}_{\mathrm{total,BI}}$. However, in the special case of a body that is exceedingly compact, we can do better, as we shall explain in the next subsection.

4.3.3 The dependence of the $\dot{E}_{\infty}$ on the central body's internal structure

Consider a central body sufficiently compact that gravity near its surface blue-shifts the orbiting object's tidal field, making it appear like ingoing gravitational waves as seen by stationary observers. This is the case, for example, when the central body is a black hole. Then, we claim, the ratio

---

[4] Ryan calculates the phasing relation to 2PN order (i.e., to $O(v^4)$ past leading order). By extending Ryan's calculation to higher post-Newtonian orders, the terms omitted from Eq. (4.5) can be written explicitly.

$\dot{E}_{\infty\mathrm{BI}}/\dot{E}_{\mathrm{body}}$ is very small:

$$\frac{\dot{E}_{\infty\mathrm{BI}}}{\dot{E}_{\mathrm{body}}} \sim v^n \ll 1 \ , \tag{4.12}$$

where n is a large number, very likely 5. For LISA, almost all of the wave cycles used in extracting information from the waves will be from radii where $v \lesssim 0.5$ so $v^5 \lesssim 0.03$. For example, for a Kerr black hole, if the spin parameter is $a/M \lesssim 0.5$, then at the innermost stable circular orbit, $v \lesssim 0.5$. Consequently, almost all of the measured $\dot{E}_{\mathrm{total,BI}}$ will go into the body itself via tidal coupling, so $\dot{E}_{\mathrm{body}}$ will be measured to good accuracy.

To understand our claim that $\dot{E}_{\infty\mathrm{BI}}/\dot{E}_{\mathrm{body}} \sim v^n$ for some large n, consider a central body whose external metric is that of a Kerr black hole. In this case, one can use the Teukolsky formalism [22] (first-order perturbation theory in the mass ratio μ/M) to compute the energies radiated to infinity and tidally coupled into the central body. We have carried out that Teukolsky analysis for general a/M and present the details for the special case $a = 0$ in the Appendix. Here we explain the underlying physics. We begin with some preliminaries:

We need only consider the primary-frequency waves, $f = \Omega_\phi/\pi$, since they account for all the energy loss and transfer, up to corrections second order in the eccentricity e and inclination angle ι. This means, correspondingly, that we can restrict ourselves to a precisely circular and equatorial orbit. The waves and tidal coupling then have predominantly spheroidal harmonic order $\ell = m = 2$ and frequency f (angular frequency $\omega = 2\pi f = 2\Omega_\phi$). Since we only want to know, to within factors of order unity, the ratio $\dot{E}_{\infty\mathrm{BI}}/\dot{E}_{\mathrm{body}}$, it will be sufficient to restrict ourselves to these dominant $\ell = m = 2$, $\omega = 2\Omega_\phi$ perturbations.

In the Teukolsky formalism, these perturbations are embodied in a radial "wave function" that can be normalized in a variety of different ways. The usual normalization, based on the Newman-Penrose field ψ_4, is bad for physical insight because it treats outgoing waves and ingoing waves quite differently (see the Appendix). One normalization that treats them on the same footing sets the radial wave function equal to that of the tidal gravitational field ("electric-type" components of the Weyl or Riemann curvature tensor) measured by "zero-angular-momentum" observers, ZAMOs (a family of observers, each of whom resides at fixed radius r and polar angle θ). We shall denote that tidal field [with $e^{-i\omega t} \times$ (spheroidal harmonic) factored out so the field is complex, not real] by $\mathcal{E}$. Another, closely related normalization for the radial wave function sets its modulus squared equal to the rate of flow of energy. We shall denote this choice by Ψ. At large radii, $\mathcal{E} \sim (\ddot{h}_+ + i\ddot{h}_\times) = \omega^2(h_+ + ih_\times)$, where h_+ and $h_\times$ are the dimensionless gravitational wave fields; so the radiated energy is $\dot{E}_\infty \sim r^2|\dot{h}_+ + i\dot{h}_\times|^2 \sim (r/\omega)^2\mathcal{E}_\infty^2$, which tells us that $\Psi_\infty \sim (r/\omega)\mathcal{E}_\infty$. Near the body's surface (i.e., near where the horizon would be if the body were a Kerr black hole), the energy flux is $\dot{E} \sim (r/\omega)^2|\alpha^2\mathcal{E}|^2$, where α is the Kerr-metric lapse function, which goes to zero at the horizon

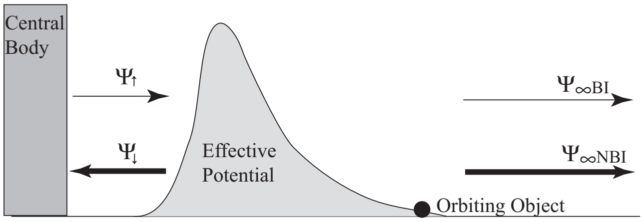

Figure 4.1: The renormalized tidal gravitational fields Ψ produced near a central body's surface and at large radii by the orbiting object, when the central body has the same exterior metric as a Kerr black hole.

radius. (The ZAMOs' divergently large outward speed, relative to infalling observers, causes them to see a divergently large tidal field; the factor α^2 corrects for that divergence; see, e.g., the discussion in Sec. VI.C.2 of [23].) Thus, in order to ensure that the power flow is the square of the renormalized radial wave function,

$$\dot{E} \sim |\Psi|^2 \,, \tag{4.13}$$

we must renormalize the ZAMO-measured tidal field $\mathcal{E}$ by

$$\begin{aligned} \Psi &\sim (r/\omega)\mathcal{E} \text{ at } r \to \infty \,, \\ \Psi &\sim (\alpha^2 r/\omega)\mathcal{E} \text{ near body} \,. \end{aligned} \tag{4.14}$$

With these preliminaries finished, we can give our physical argument for Eq. (4.12) in terms of the radial wave function Ψ. Our argument relies on Fig. 4.1.

If the central body is a Kerr black hole, then the boundary condition on Ψ at its surface (the horizon) is purely downgoing waves, and at infinity, purely outgoing waves. The ratio of downgoing power at the horizon to outgoing power at infinity has the standard Kerr values [24, 25]: $\dot{E}_{\rm body}/\dot{E}_{\infty\rm NBI} \sim v^8$ if the hole's spin angular velocity Ω_H is much less than the orbital angular velocity Ω_ϕ; and $\dot{E}_{\rm body}/\dot{E}_{\infty\rm NBI} \sim v^5$ if $\Omega_H \gg \Omega_\phi$. (Here we have used the *no-body-influence* notation $\dot{E}_{\infty\rm NBI}$ for the outgoing power because a central black hole's internal structure is unable to influence the waves radiated to infinity.) Correspondingly, by virtue of Eq. (4.13), the ratio of the downgoing field at the horizon $\Psi_\downarrow$ to the outgoing field at infinity $\Psi_{\infty\rm NBI}$ is

$$\frac{\Psi_\downarrow}{\Psi_{\infty\rm NBI}} \sim \left\{ \begin{array}{c} v^4 \\ v^{5/2} \end{array} \right\} \text{ for } \left\{ \begin{array}{c} \Omega_H \ll \Omega_\phi \\ \Omega_H \gg \Omega_\phi \end{array} \right\} . \tag{4.15}$$

This suppression of the downgoing field relative to the outgoing is due, mathematically, to a reflective effective potential in the wave equation that Ψ satisfies (Fig. 4.1). Physically, it is due to coupling of the field Ψ to the central body's spacetime curvature.

Now suppose the central body is not a black hole, but some other object so compact that its surface is well beneath the peak of the effective potential. This mathematical assumption is equivalent to our physical assumption that the ZAMOs see the downgoing field $\Psi_\downarrow$ so strongly blue-shifted by the central body's gravity that it looks like radiation. The only way, then, that the central body can influence the energy radiated to infinity is to reflect a portion of this downgoing radiation back upward. Mathematically, this corresponds to replacing the black hole's downgoing boundary condition by

$$\Psi_\uparrow = \mathcal{R}\psi_\downarrow \tag{4.16}$$

at some chosen radius just above the body's surface. Here $\Psi_\downarrow$ and $\Psi_\uparrow$ are the downgoing and upgoing components of Ψ; see Fig. 4.1. For simplicity, we shall assume that the amplitude reflection coefficient $\mathcal{R}$ is small, $|\mathcal{R}| \ll 1$. Otherwise we would have to deal with a possible resonant buildup of energy between the reflective central body and the reflective effective potential—though that would not change our final answer (see, e.g., the more detailed analysis in the Appendix).

The upgoing waves $\Psi_\uparrow$ have great difficulty getting through the effective potential. The fraction of the upgoing power that gets transmitted through, successfully, is $\sim (M\omega)^6$ if the hole rotates slowly, and $\sim (M\omega)^5$ if rapidly [Eq. (8.83) of [23] with $\ell = 2$ and $\sigma_\infty = \omega$]. Since the fields Ψ are the square roots of the powers (aside from complex phase) and since $M\omega = 2M\Omega_\phi = 2v^3$, this power transmissivity corresponds to

$$\frac{\Psi_{\infty \rm BI}}{\Psi_\uparrow} \sim \left\{ \begin{array}{c} v^9 \\ v^{15/2} \end{array} \right\} \text{ for } \left\{ \begin{array}{c} \Omega_H \ll \Omega_\phi \\ \Omega_H \gg \Omega_\phi \end{array} \right\} . \tag{4.17}$$

Combining Eqs. (4.17), (4.16), and (4.15), we see that

$$\frac{\Psi_{\infty \rm BI}}{\Psi_{\infty \rm NBI}} \sim \left\{ \begin{array}{c} v^{13} \\ v^{10} \end{array} \right\} \text{ for } \left\{ \begin{array}{c} \Omega_H \ll \Omega_\phi \\ \Omega_H \gg \Omega_\phi \end{array} \right\} . \tag{4.18}$$

If these two complex outgoing fields are not precisely out of phase with each other (phase difference $\pm\pi/2$), then the outgoing power is $|\Psi_{\infty \rm NBI} + \Psi_{\infty \rm BI}|^2 \simeq |\Psi_{\infty \rm NBI}|^2 + 2\Re\left(\Psi_{\infty \rm NBI}\Psi^*_{\infty \rm BI}\right)$, which means that the ratio of the radiated body-influenced power to radiated no-body-influence power is

$$\frac{\dot{E}_{\infty \rm BI}}{\dot{E}_{\infty \rm NBI}} \sim \left\{ \begin{array}{c} v^{13} \\ v^{10} \end{array} \right\} \text{ for } \left\{ \begin{array}{c} \Omega_H \ll \Omega_\phi \\ \Omega_H \gg \Omega_\phi \end{array} \right\} . \tag{4.19}$$

In the unlikely case (which we shall ignore) that the two fields are precisely out of phase, the ratio will be the square of this.

By combining Eq. (4.19) with the square of Eq. (4.15), we obtain the ratio of the body-influence power radiated to infinity over the tidal coupling power into the central body:

$$\dot{E}_{\infty \mathrm{BI}}/\dot{E}_{\mathrm{body}} \sim v^5 \tag{4.20}$$

independent of whether the body rotates slowly or rapidly. This is the claimed result.

If the central body's external metric is not Kerr, then the first-order perturbation equations for the orbiting body's spacetime curvature will probably not be separable in $\{r, \theta\}$, so the analysis will be much more complex. Nevertheless the physical situation presumably is unchanged in this sense: The body's spacetime curvature will couple to the perturbation field in such a way as to resist energy flow through the region between the body's surface and the object's orbit. Correspondingly, the perturbation fields and power flows are very likely to behave in the same manner as for the Kerr metric, with the same final result, $\dot{E}_{\mathrm{body}}/\dot{E}_{\infty \mathrm{BI}} \sim v^n$ with n very likely still 5 but possibly some other number significantly larger than one.

If this is, indeed, the case, then for any sufficiently compact central body the power tidally deposited into the body $\dot{E}_{\mathrm{body}}$ will be very nearly equal to $\dot{E}_{\mathrm{total},BI}$, which is measurable; and therefore the tidal power will be measurable.

4.4 Conclusion

In this paper, we have extended Ryan's analysis to show that in principle it is possible to recover not only the spacetime geometry of the central body, but also the evolving orbital parameters of the inspiraling object and the evolving tidal coupling between the small object and the central body. Therefore, in principle we can obtain a full description of the SARSAF spacetime, the tidal coupling, and the inspiral orbit from EMRI or IMRI waveforms. In practice, the method of extracting the information is likely to be quite different from the algorithm we have presented here.

Further generalizations of Ryan's theorem and development of practical methods to implement it are topics of our ongoing research.

4.5 Appendix A: An explicit derivation of results in Section 4.3.3

4.5.1 Teukolsky perturbation formalism

In this subsection, we use the Teukolsky perturbation theory to justify our results in Sec. 4.3.3. We first briefly review the standard Teukolsky perturbation formalism. Details can be found, e.g., in [26]. To shorten our expressions, in this appendix we restrict ourselves to a nonrotating central body with external metric the same as a Schwarzschild black hole but with a finite reflectivity. The generalization to the Kerr metric is straightforward but with more cumbersome algebra. We have carried it out, obtaining the same result as is found by the physical argument in the text.

In the Teukolsky formalism, people usually calculate the perturbation to a Newman-Penrose quantity ψ_4 that is related to the ZAMO-measured tidal field $\mathscr{E}$ by a linear transformation of the basis vectors. This ψ_4 can be decomposed into Fourier-Harmonic components according to

$$\psi_4 = \frac{1}{r^4}\int_{-\infty}^{\infty} d\omega \sum_{lm} R_{\omega lm}(r)\, {}_{-2}Y_{lm}(\theta,\phi) e^{-i\omega t}, \tag{4.21}$$

where ${}_{-2}Y_{lm}(\theta,\phi)$ are the spin-weighted spherical harmonics. The radial function $R_{\omega lm(r)}$ satisfies the inhomogeneous Teukolsky equation

$$\left[r^2\alpha^2\frac{d^2}{dr^2} - 2(r-M)\frac{d}{dr} + U(r)\right] R_{\omega lm}(r) = T_{\omega lm}, \tag{4.22}$$

where $\alpha^2 = 1 - 2M/r$ is the lapse function for the Schwarzschild metric. The expressions for the potential $U(r)$ and the source $T_{\omega lm}$ can be found, e.g., in [24], Eqs. (2.3), (A1).

In order to solve this equation, we construct two linearly independent solutions to the homogeneous Teukolsky equation, which satisfy the following boundary conditions,

$$\begin{aligned}
R^{\rm IN}_{\omega lm} &\rightarrow \begin{cases} (\omega r)^4\alpha^4 e^{-i\omega r^*}, & r \rightarrow 2M \\ (\omega r)^{-1} Q^{\rm in}_{\omega lm} e^{-i\omega r^*} + (\omega r)^3 Q^{\rm out}_{\omega lm} e^{i\omega r^*}, & r \rightarrow +\infty \end{cases} \\
R^{\rm UP}_{\omega lm} &\rightarrow \begin{cases} (\omega r)^4\alpha^4 P^{\rm out}_{\omega lm} e^{-i\omega r^*} + P^{\rm in}_{\omega lm} e^{i\omega r^*}, & r \rightarrow 2M \\ (\omega r)^3 e^{i\omega r^*}, & r \rightarrow +\infty \end{cases}
\end{aligned} \tag{4.23}$$

where $d/dr^* = \alpha^2 d/dr$. From these two homogeneous solutions, we can construct the inhomogeneous solution according to

$$\begin{aligned}
R_{\omega lm}(r) = \frac{1}{\text{Wronskian}[R^{\rm UP}_{\omega lm}, R^{\rm IN}_{\omega lm}]} &\left(R^{\rm UP}_{\omega lm}(r) \int_{2M}^{r} dr' R^{\rm IN}_{\omega lm}(r') \mathcal{T}_{\omega lm}(r') \right. \\
&\left. + R^{\rm IN}_{\omega lm}(r) \int_{r}^{\infty} dr' R^{\rm UP}_{\omega lm}(r') \mathcal{T}_{\omega lm}(r') \right),
\end{aligned} \tag{4.24}$$

where $\mathcal{T}_{\omega lm}(r) \equiv T_{\omega lm}(r)(r^2 - 2Mr)^{-2}$. This solution has only outgoing waves at infinity and satisfies the purely ingoing boundary condition: ([24], Eqs. (2.8) and (2.9))

$$\begin{aligned}
R_{\omega lm}(r\rightarrow\infty) &\sim \mu\omega^2 Z^{\rm IN}_{\omega lm} r^3 e^{i\omega r^*}, \\
R_{\omega lm}(r\rightarrow 2M) &\sim \mu\omega^3 Z^{\rm UP}_{\omega lm} r^4 \alpha^4 e^{-i\omega r^*},
\end{aligned} \tag{4.25}$$

where

$$Z^{\mathrm{IN,UP}}_{\omega lm} = \frac{1}{2i\mu\omega^2 Q^{\mathrm{in}}_{\omega lm}} \times \int_{2M}^{\infty} dr \left[(r^2 - 2Mr)^{-2} R^{\mathrm{IN,UP}}_{\omega lm}(r) T_{\omega lm}(r) \right]. \tag{4.26}$$

At infinity, where the spacetime is almost flat, ψ_4 is directly related to the outgoing gravitational wave strains according to

$$\psi_4 = \frac{1}{2}\left(\ddot{h}_+ - i\ddot{h}_\times\right), \tag{4.27}$$

and we can obtain the luminosity formula ([24], Eq. (2.21))

$$\dot{E}_\infty = \frac{1}{4\pi}\left(\frac{\mu}{M}\right)^2 \sum_{lm} (M\omega)^2 |Z^{\mathrm{IN}}_{\omega lm}|^2. \tag{4.28}$$

4.5.2 Inner boundary condition

The above purely ingoing boundary condition makes sense when the central body is a black hole because we know everything is absorbed at the horizon of the black hole. If the central body is some other kind of object, the only way it can influence the perturbation field $R_{\omega lm}$ just above its surface is by producing an outgoing-wave component via some effective reflectivity $\mathcal{R}$. The result will be a modified field

$$R_{\omega lm}(r \to 2M) \sim e^{-i\omega r^*} + (\text{something}) e^{i\omega r^*}. \tag{4.29}$$

The "something" will be proportional to $\mathcal{R}$, and it will also have a peculiar radial dependence, because ψ_4 relies for its definition on an ingoing null tetrad and thereby treats ingoing and outgoing waves in very different manners.

4.5.3 Chandrasekhar transform

To learn what the "something" should be, we can transform to a new radial wave function that treats ingoing and outgoing waves on the same footing. Two such functions were introduced and used in Sec. 4.3.3: the ZAMO-measured tidal field $\mathcal{E}$ and a field Ψ whose modulus squared is the power flow, for both outgoing and ingoing waves. Those choices are good for Sec.4.3.3's physical, order-of-magnitude arguments, but at general radii r they not related in any simple way to ψ_4. A choice that *is* simply related to ψ_4 is the Regge-Wheeler function X, and we shall use it here.

The radial wave function R for the Newman-Penrose ψ_4 is related to the Regge-Wheeler function

X by the Chandrasekhar transform, Eq. (A6) of [24]. This Chandrasekhar transform takes the form

$$R^{\mathrm{IN,UP}}_{\omega lm} = \chi^{\mathrm{IN,UP}}_{\omega lm} C_\omega X^{\mathrm{IN,UP}}_{\omega lm}, \tag{4.30}$$

where

$$\begin{aligned} \chi^{\mathrm{IN}}_{\omega lm} &= \frac{16(1-2iM\omega)(1-4iM\omega)(1+4iM\omega)}{(l-1)l(l+1)(l+2)-12iM\omega}(M\omega)^3, \\ \chi^{\mathrm{UP}}_{\omega lm} &= -\frac{1}{4}. \end{aligned} \tag{4.31}$$

C_ω is a second-order differential operator, and $X^{\mathrm{IN,UP}}_{\omega lm}$ are two linearly independent solutions of the homogeneous Regge-Wheeler equation

$$\left[\frac{d^2}{dr^{*2}} + \omega^2 - V(r)\right] X_{\omega lm}(r) = 0, \tag{4.32}$$

where

$$V(r) = \alpha^2 \left[\frac{l(l-1)}{r^2} - \frac{6M}{r^3}\right]. \tag{4.33}$$

The asymptotic expressions for $X^{\mathrm{IN,UP}}_{\omega lm}$ are ([24], Eq. (2.7))

$$\begin{aligned} X^{\mathrm{IN}}_{\omega lm} &\to \begin{cases} e^{-i\omega r^*}, & r \to 2M \\ A^{\mathrm{in}}_{\omega lm} e^{-i\omega r^*} + A^{\mathrm{out}}_{\omega lm} e^{i\omega r^*}, & r \to +\infty \end{cases} \\ X^{\mathrm{UP}}_{\omega lm} &\to \begin{cases} -B^{\mathrm{out}}_{\omega lm} e^{-i\omega r^*} + B^{\mathrm{in}}_{\omega lm} e^{i\omega r^*}, & r \to 2M \\ e^{i\omega r^*}, & r \to +\infty. \end{cases} \end{aligned} \tag{4.34}$$

Here we note that by the conservation of the Wronskian, it is straightforward to show that $B^{\mathrm{in,out}} = A^{\mathrm{in,out}}$.

4.5.4 $\dot{E}_\infty$ with a reflective inner boundary condition

Because the Regge-Wheeler function treats outgoing and ingoing waves on the same footing, the desired, reflective inner boundary condition for it takes the simple form

$$\tilde{X}^{\mathrm{IN}}_{\omega lm}(r \to 2M) \quad \sim \quad e^{-i\omega r^*} + \mathcal{R} e^{i\omega r^*}. \tag{4.35}$$

Here $\tilde{X}^{\mathrm{IN}}_{\omega lm}$ is a new homogeneous solution of the Regge-Wheeler equation.

This new homogeneous solution is a superposition of both ingoing and outgoing waves at the horizon. It is shown in [27] that because the Regge-Wheeler function treats outgoing and ingoing waves in the same manner, $|\mathcal{R}|^2$ has the physical meaning of the energy flux reflectivity, i.e., the ratio between outgoing and ingoing energy flux at the horizon.

The homogeneous solution (4.35) which satisfies the new inner boundary condition can be constructed from the old homogeneous solutions:

$$\tilde{X}^{\rm IN}_{\omega lm} = \beta_1 X^{\rm IN}_{\omega lm} + \beta_2 X^{\rm UP}_{\omega lm}, \tag{4.36}$$

where

$$\beta_1 = 1 + \frac{\mathcal{R} A^{\rm out}_{\omega lm}}{A^{\rm in}_{\omega lm}}, \qquad \beta_2 = \frac{\mathcal{R}}{A^{\rm in}_{\omega lm}}. \tag{4.37}$$

After doing an inverse Chandrasekhar transform, we obtain the corresponding homogeneous solution of the homogeneous Teukolsky equation

$$\tilde{R}^{\rm IN}_{\omega lm} = R^{\rm IN}_{\omega lm} + \frac{\beta_2}{\beta_1}\frac{\chi^{\rm IN}_{\omega lm}}{\chi^{\rm UP}_{\omega lm}} R^{\rm UP}_{\omega lm}. \tag{4.38}$$

Now we can replace $R^{\rm IN}$ by $\tilde{R}^{\rm IN}$ in Eq. (4.24) to obtain the solution $\tilde{R}_{\omega lm}(r)$ which satisfies the inhomogeneous Teukolsky equation with upgoing and downgoing waves at the horizon and purely outgoing waves at infinity. From this $\tilde{R}_{\omega lm}(r)$ we identify the new amplitudes $\tilde{Z}^{\rm IN}_{\omega lm}$ as in Eq. (4.25):

$$\tilde{Z}^{\rm IN}_{\omega lm} = Z^{\rm IN}_{\omega lm} + \frac{\beta_2}{\beta_1}\frac{\chi^{\rm IN}_{\omega lm}}{\chi^{\rm UP}_{\omega lm}} Z^{\rm UP}_{\omega lm}. \tag{4.39}$$

From these new $\tilde{Z}^{\rm IN}_{\omega lm}$ the calculation of the luminosity at infinity is straightforward.

In [24] Poisson and Sasaki have already worked out all the relevant formulae, so we only give the results. For the original expressions in [24], please refer to Eq. (3.25) for $A^{\rm in}, A^{\rm out}$; Eq. (A7) for $\chi^{\rm IN}, \chi^{\rm UP}$; and Eqs. (5.4), (5.6), (5.11), (5.12) for $Z^{\rm IN}_{\omega lm}, Z^{\rm UP}_{\omega lm}$.

The leading luminosity correction comes from the $l = 2, m = \pm 2$ mode, and we have

$$\dot{E}_\infty = \dot{E}_\infty\Big|_{\rm Schwarzschild} \left|1 - \frac{128 i \mathcal{R} v^{13}}{15\beta_1}\right|^2, \tag{4.40}$$

where v is the same PN expansion parameter as that in Sec. 4.3.3. Unless the reflection coefficient $\mathcal{R}$ is precisely real, this gives

$$\dot{E}_\infty = \dot{E}_\infty\Big|_{\rm Schwarzschild} \left[1 + \frac{256}{15}\Im\left(\frac{\mathcal{R}}{\beta_1}\right) v^{13}\right] \tag{4.41}$$

in agreement with Eq. (4.19). The change in $\dot{E}_{\rm body}$ should be

$$\dot{E}_{\rm body} = \dot{E}_{\rm body}\Big|_{\rm Schwarzschild} \left(\frac{1-|\mathcal{R}|^2}{|\beta_1|^2}\right) \tag{4.42}$$

where β_1 is defined in Eq. (4.37).

4.6 Bibliography

[1] M. Colpi, S. L. Shapiro, and I. Wasserman, Phys. Rev. Lett. **57**, 2485 (1986).

[2] F. D. Ryan, Phys. Rev. D **55**, 6081 (1997).

[3] T. D. Lee, Phys. Rev. D **35**, 3637 (1987).

[4] D. Brown et al., Phys. Rev. Lett. (submitted) (2007), URL `http://www.arxiv.org/gr-qc/0612060`.

[5] A. Abramovici et al., Science **256**, 325 (1992).

[6] F. D. Ryan, Phys. Rev. D **52**, 5707 (1995).

[7] K. S. Thorne, in *The Future of Theoretical Physics and Cosmology: Celebrating Stephen Hawking's 60th Birthday*, G. W. Gibbons, S. J. Rankin, and E. P. S. Shellard, Eds., (Cambridge University Press, 2003), pp. 74–104.

[8] T. Prince and K. Danzmann, Tech. Rep., LISA International Science Team (2007), URL `http://www.rssd.esa.int/SYS/docs/ll_transfers/LISA_Science_Requirements.pdf`.

[9] C. Li, (in preparation).

[10] J. R. Gair et al., Class. Quantum Grav. **21**, S1595 (2004).

[11] J. Gair and L. Wen, Class. Quantum Grav. **22**, S1359 (2005).

[12] D. Brown, (in preparation).

[13] N. A. Collins and S. A. Hughes, Phys. Rev. D **69**, 124022 (2004).

[14] K. Glampedakis and S. Babak, Class. Quantum Grav. **23**, 4167 (2006).

[15] A. Stroeer, J. Gair, and A. Vecchio, in *LASER INTERFEROMETER SPACE ANTENNA: 6th International LISA Symposium*, S. Merkowitz and J. C. Livas, Eds., (2006), Vol. 873 of *AIP Conference Proceedings*, p. 444.

[16] T. P. Sotiriou and A. Apostolatos, Phys. Rev. D **71**, 044005 (2005).

[17] H. Fang and G. Lovelace, Phys. Rev. D **72**, 124016 (2005).

[18] R. M. Wald, *General Relativity* (University of Chicago Press, Chicago, 1984).

[19] R. Geroch, J. Math. Phys. **11**, 2580 (1970).

[20] R. Hansen, J. Math. Phys. **15**, 46 (1974).

[21] S. Drasco and S. A. Hughes, Phys. Rev. D **73**, 024027 (2006).

[22] S. A. Teukolsky, Astrophys. J. **185**, 635 (1973).

[23] K. S. Thorne, R. Price, and D. MacDonald, *Black Holes: The Membrane Paradigm* (Yale University Press, New Haven, 1986).

[24] E. Poisson and M. Sasaki, Phys. Rev. D **51**, 5753 (1995).

[25] H. Tagoshi, S. Mano, and E. Takasugi, Prog. Theor. Phys. **98**, 829 (1997).

[26] M. Sasaki and H. Tagoshi, analytical Black Hole Perturbation Approach to Gravitational Radiation, *Living Rev. Relativity* **6** (2003), URL `http://www.livingreviews.org/lrr-2003-6`.

[27] S. Chandrasekhar, *The Mathematical Theory of Black Holes* (Oxford University Press, Oxford, 1985), Ch. 4, 9.

Chapter 5

Reducing orbital eccentricity in binary-black-hole simulations

Binary black hole simulations starting from quasi-circular (i.e., zero radial velocity) initial data have orbits with small but non-zero orbital eccentricities. In this paper the quasi-equilibrium initial-data method is extended to allow non-zero radial velocities to be specified in binary black hole initial data. New low-eccentricity initial data are obtained by adjusting the orbital frequency and radial velocities to minimize the orbital eccentricity, and the resulting (~ 5 orbit) evolutions are compared with those of quasi-circular initial data. Evolutions of the quasi-circular data clearly show eccentric orbits, with eccentricity that decays over time. The precise decay rate depends on the definition of eccentricity; if defined in terms of variations in the orbital frequency, the decay rate agrees well with the prediction of Peters (1964). The gravitational waveforms, which contain ~ 8 cycles in the dominant $l = m = 2$ mode, are largely unaffected by the eccentricity of the quasi-circular initial data. The overlap between the dominant mode in the quasi-circular evolution and the same mode in the low-eccentricity evolution is about 0.99.

Originally accepted for publication as Harald P. Pfeiffer, Duncan A. Brown, Lawrence E. Kidder, Lee Lindblom, Geoffrey Lovelace, and Mark A. Scheel, as a special issue article in Class. Quantum Grav. (2007), preprint available online at `http://arxiv.org/abs/gr-qc/0702106`.

5.1 Introduction

The inspiral and merger of binary black holes is one of the most promising sources for current and future generations of interferometric gravitational wave detectors such as LIGO and VIRGO [1, 2]. The initial LIGO detectors, which are currently operating at design sensitivity, could detect binary black hole inspirals up to distances of several hundred megaparsecs. In order to take full advantage of the sensitivity of these detectors, detailed knowledge of the gravitational waveform is required.

Recent breakthroughs in numerical relativity have allowed several research groups to simulate binary black hole inspirals for multiple orbits [3, 4, 5, 6, 7]. Because of the large computational cost of these simulations, only a small number of orbits can be followed. Therefore it is important to begin these simulations with initial data that closely approximate a snapshot of a binary black hole system that is only a few orbits from merger. During the inspiral, the orbits of binary compact objects circularize via the emission of gravitational waves [8], so binaries formed from stellar evolution (rather than dynamical capture) are expected to have very small eccentricities by the time they enter the sensitive band of ground based detectors. Because of this, the assumption of a quasi-circular orbit (i.e., zero radial velocity) has been widely used in the construction of binary black hole initial data [9, 10, 11, 12, 13, 14, 15, 16, 17, 18, 19, 20, 21, 22, 23]. Specifically, quasi-equilibrium data [17] and the "QC-sequence" [24] of puncture data [25] seem to be the most popular, and both of these assume a quasi-circular orbit. However, inspiraling compact objects have a small inward radial velocity, and neglecting this velocity when constructing initial data will lead to eccentricity in the subsequent evolution, as discussed in the context of post-Newtonian theory in [26], and found numerically in [27].

The Caltech/Cornell collaboration has recently completed successful long-term simulations of inspiraling binary black holes [6] using a pseudo-spectral multi-domain method. This technique was used to evolve a particular quasi-circular quasi-equilibrium binary black hole initial data set (coordinate separation $d = 20$ from Table IV of [17]). Figure 5.1 shows the proper separation s between the horizons and the radial velocity ds/dt as functions of time for this evolution. The rapid convergence afforded by spectral methods is apparent; the medium and high resolutions are nearly indistinguishable on the plot. Eccentricity of the orbit in the form of oscillatory variations in s and ds/dt is, unfortunately, also clearly apparent.

This noticeable eccentricity suggests two questions: First, how can initial data with the appropriate black hole radial velocities be constructed for non-eccentric inspirals? Second, how do evolutions of quasi-circular initial data differ from those of non-eccentric initial data? This paper addresses both questions. In Sec. 5.2, we incorporate nonzero radial velocities into the quasi-equilibrium method to construct binary black hole initial data. This results in one additional parameter for equal mass initial data, the radial velocity v_r. Sec. 5.3 briefly discusses our numerical methods. Sec. 5.4 describes how we choose v_r and the the orbital frequency Ω_0 for equal mass co-rotating binary black holes, and presents numerical evolutions of the resulting low-eccentricity initial data. This section also presents convergence tests of these binary black hole evolutions; we examine both convergence with respect to spatial resolution and convergence with respect to the radius of the outer boundary of the computational domain. Sec. 5.5 examines the differences between evolutions of quasi-circular initial

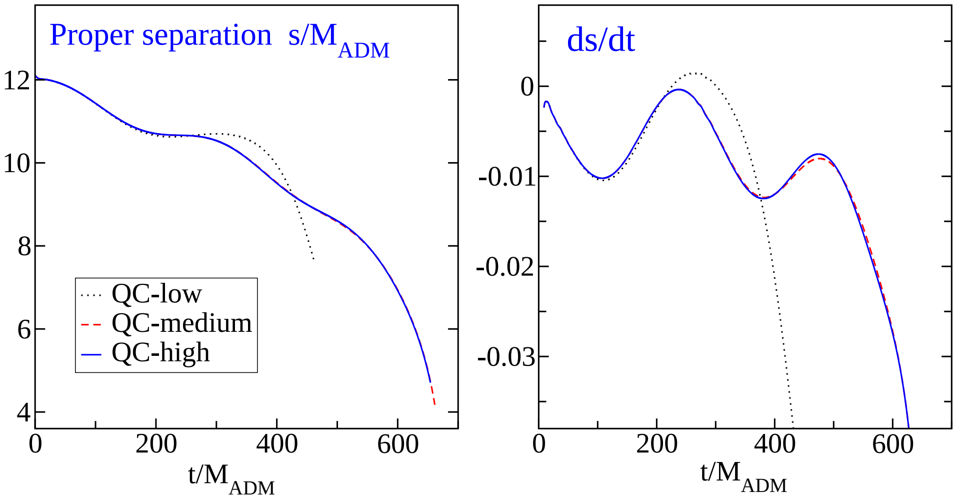

Figure 5.1: Evolution of quasi-circular initial data. The left panel shows the proper separation s between the apparent horizons, computed at constant coordinate time along the coordinate line connecting the centers of the horizons, and the right panel shows its time derivative ds/dt. This evolution was run at three different resolutions, with the medium and high resolution tracking each other very closely through the run.

data and low-eccentricity initial data. We close with a summary and discussion of these results in Sec. 5.6.

5.2 Quasi-equilibrium data with nonzero radial velocity

In this section we extend the quasi-equilibrium approach [14, 16, 17, 20] to allow specification of nonzero radial velocities of the black holes. We proceed in three steps: First, we summarize the construction of quasi-equilibrium data using co-rotating coordinates [17, 20]. Second, we show that the *identical* quasi-circular initial data can be obtained by solving essentially the same equations but in an asymptotically inertial coordinate system; the major difference is that one must require the black holes to *move* on circular trajectories, rather than remaining fixed in the coordinate system. Third, we generalize from black holes moving on circular trajectories to black holes moving on inspiral trajectories.

5.2.1 Overview

We use the nomenclature of [17]; the spacetime line element is written in the usual 3+1-form,

$$\mathrm{d}s^2 = -\alpha^2 \mathrm{d}t^2 + \gamma_{ij}(\mathrm{d}x^i + \beta^i \mathrm{d}t)(\mathrm{d}x^j + \beta^j \mathrm{d}t), \tag{5.1}$$

where γ_{ij} is the 3-metric induced on a t = constant spatial hypersurface, α is the lapse function and β^i is the shift vector. Latin indices label spatial coordinates, and Greek indices label spacetime coordinates. The extrinsic curvature of the hypersurface is defined by

$$K_{\mu\nu} \equiv -\gamma_\mu{}^\rho \gamma_\nu{}^\sigma \, {}^{(4)}\nabla_{(\rho} n_{\sigma)}, \tag{5.2}$$

where ${}^{(4)}\nabla$ is the spacetime derivative operator and n_μ is the future-pointing unit normal to the slice[1]. We use the extended conformal thin sandwich formalism [28, 29] to construct constraint-satisfying initial data. In this approach, the three-dimensional metric is spit into a conformal metric $\tilde{\gamma}_{ij}$ and a positive conformal factor ψ,

$$\gamma_{ij} = \psi^4 \tilde{\gamma}_{ij}, \tag{5.3}$$

and the extrinsic curvature is split into trace and trace-free parts,

$$K_{ij} = A_{ij} + \frac{1}{3}\gamma_{ij} K. \tag{5.4}$$

The freely specifiable data consist of the conformal metric $\tilde{\gamma}_{ij}$, its time derivative $\tilde{u}_{ij} \equiv \partial_t \tilde{\gamma}_{ij}$ (which is taken to be trace free), the mean curvature $K \equiv K_{ij}\gamma^{ij}$, and its time derivative $\partial_t K$. It follows that the trace-free part of the extrinsic curvature takes the form

$$A_{ij} = \frac{1}{2\alpha}\left[(\mathbb{L}\beta)_{ij} - \psi^4 \tilde{u}_{ij}\right] = \psi^{-2}\tilde{A}_{ij}, \quad \tilde{A}_{ij} = \frac{1}{2\tilde{\alpha}}\left[(\tilde{\mathbb{L}}\beta)_{ij} - \tilde{u}_{ij}\right], \tag{5.5}$$

where

$$(\mathbb{L}\beta)^{ij} \equiv 2\nabla^{(i}\beta^{j)} - \frac{2}{3}\gamma^{ij}\nabla_k\beta^k, \quad (\tilde{\mathbb{L}}\beta)^{ij} \equiv 2\tilde{\nabla}^{(i}\beta^{j)} - \frac{2}{3}\tilde{\gamma}^{ij}\tilde{\nabla}_k\beta^k. \tag{5.6}$$

The symbols $(\mathbb{L}\beta)^{ij}$ and $(\tilde{\mathbb{L}}\beta)^{ij}$ represent the conformal Killing operators in physical and conformal space, respectively, and are related by $(\mathbb{L}\beta)^{ij} = \psi^{-4}(\tilde{\mathbb{L}}\beta)^{ij}$. Indices on conformal tensors are raised and lowered with the conformal metric, for example, $(\tilde{\mathbb{L}}\beta)_{ij} \equiv \tilde{\gamma}_{ik}\tilde{\gamma}_{jl}(\tilde{\mathbb{L}}\beta)^{kl} = \psi^{-4}(\mathbb{L}\beta)_{ij}$. Furthermore, ∇ and $\tilde{\nabla}$ denote the physical and conformal spatial covariant derivative operators, and the conformal lapse is defined by $\alpha = \psi^6\tilde{\alpha}$. Inverting Eq. (5.5) yields

$$\tilde{u}_{ij} = \partial_t \tilde{\gamma}_{ij} = -2\tilde{\alpha}\tilde{A}_{ij} + (\tilde{\mathbb{L}}\beta)_{ij}. \tag{5.7}$$

Substituting these relations into the constraint equations and into the evolution equation for the extrinsic curvature, one arrives at a system of five elliptic equations, often referred to as the

---

[1] Since $K_{\mu\nu}$ is a spatial tensor, $K_{\mu\nu}n^\nu = 0$, its spatial components K_{ij} carry all its information. Almost all tensors in this paper are spatial, and we use spatial indices here whenever possible.

extended conformal thin sandwich (XCTS) equations:

$$\tilde{\nabla}^2\psi - \frac{1}{8}\tilde{R}\psi - \frac{1}{12}K^2\psi^5 + \frac{1}{8}\psi^{-7}\tilde{A}^{ij}\tilde{A}_{ij} = 0, \tag{5.8a}$$

$$\tilde{\nabla}_j\Big(\frac{1}{2\tilde{\alpha}}(\tilde{\mathbb{L}}\beta)^{ij}\Big) - \frac{2}{3}\psi^6\tilde{\nabla}^i K - \tilde{\nabla}_j\Big(\frac{1}{2\tilde{\alpha}}\tilde{u}^{ij}\Big) = 0, \tag{5.8b}$$

$$\tilde{\nabla}^2(\tilde{\alpha}\psi^7) - (\tilde{\alpha}\psi^7)\left[\frac{\tilde{R}}{8}+\frac{5}{12}K^4\psi^4+\frac{7}{8}\psi^{-8}\tilde{A}^{ij}\tilde{A}_{ij}\right] = -\psi^5(\partial_t K - \beta^k\partial_k K). \tag{5.8c}$$

Here $\tilde{R}$ denotes the trace of the Ricci tensor of $\tilde{\gamma}_{ij}$. These equations are to be solved for ψ, $\tilde{\alpha}$, and β^i; given a solution, the physical initial data (γ_{ij}, K_{ij}) are obtained from Eqs. (5.3)–(5.5).

Note that a solution of the XCTS equations includes a shift vector β^i and a lapse function $\alpha = \psi^6\tilde{\alpha}$. If these values of lapse and shift are used in an evolution of the constructed initial data, then the time derivative of the mean curvature will initially equal the freely specifiable quantity $\partial_t K$, and the trace-free part of the time derivative of the metric will initially equal $\psi^4\tilde{u}_{ij}$. Thus, the free data of the XCTS equations allow direct control of certain time derivatives in the evolution of the initial data.

The next step is to choose the free data that correspond to the desired physical configuration. The quasi-equilibrium quasi-circular orbit method of constructing binary black holes [17, 20] (see also [11, 12, 14]) provides a framework for many of these choices. This method is based on the fact that the inspiral time scale for a binary compact object is much larger than the orbital time scale, so that time derivatives should be very small in the co-rotating coordinate system. Furthermore, the black holes should be in equilibrium, which provides conditions on the expansion θ and shear σ_{ij} of the outgoing null geodesics passing through the horizon. The complete set of physically motivated choices for the free data within the quasi-equilibrium method are

$$\tilde{u}_{ij} = 0, \tag{5.9a}$$

$$\partial_t K = 0, \tag{5.9b}$$

$$\psi \to 1,\ \alpha \to 1, \quad \text{as } r \to \infty, \tag{5.9c}$$

$$\beta^i \to (\mathbf{\Omega_0} \times \mathbf{r})^i, \quad \text{as } r \to \infty, \tag{5.9d}$$

$$\partial_t \text{ is tangent to } \mathcal{S}_{\text{AH}}, \tag{5.9e}$$

$$\theta = 0 \quad \text{on } \mathcal{S}, \tag{5.9f}$$

$$\sigma_{ij} = 0 \quad \text{on } \mathcal{S}, \tag{5.9g}$$

where $\mathcal{S}$ denotes the location of the apparent horizons in the initial data surface, and $\mathcal{S}_{AH}$ is the world tube of the apparent horizon obtained by evolving the initial data with lapse α and shift β^i. The first two conditions are the assumptions that the time derivatives are small. The boundary conditions in Eqs. (5.9c) and (5.9d) enforce asymptotic flatness and co-rotation. The orbital frequency Ω_0 entering

Eq. (5.9d) can be chosen by the effective potential method [9] or the Komar-mass ansatz [11], with similar results [20].

To discuss the remaining conditions, we need to introduce a few additional geometrical quantities. Denote by s^i and $\tilde{s}^i$ the physical and conformal outward-pointing spatial unit normals to $\mathcal{S}$. They obey the relations

$$s^i s^j \gamma_{ij} = 1, \quad \tilde{s}^i \tilde{s}^j \tilde{\gamma}_{ij} = 1, \quad s^i = \psi^{-2} \tilde{s}^i. \tag{5.10}$$

Then introduce the induced metric on $\mathcal{S}$ in physical and conformal space by $h_{ij} = \gamma_{ij} - s_i s_j$, and $\tilde{h}_{ij} = \tilde{\gamma}_{ij} - \tilde{s}_i \tilde{s}_j$, respectively. Because $n_\mu s^\mu = 0$, the space-time components of the unit normal are given by $s^\mu = [0, s^i]$. The outward-pointing null normal to $\mathcal{S}$ can then be written as

$$k^\mu = \frac{1}{\sqrt{2}} \left(n^\mu + s^\mu \right). \tag{5.11}$$

Eq. (5.9e) simply means that the apparent horizon is initially at rest when the initial data is evolved in the co-rotating coordinate system. It implies that the shift must take the form

$$\beta^i = \alpha s^i + \beta^i_{||} \quad \text{on } \mathcal{S}, \tag{5.12}$$

where $\beta^i_{||}$ is tangent to $\mathcal{S}$. Eq. (5.9f) ensures that $\mathcal{S}$ is an apparent horizon, and implies a boundary condition on the conformal factor,

$$\tilde{s}^k \partial_k \psi = -\frac{\psi^{-3}}{8\tilde{\alpha}} \tilde{s}^i \tilde{s}^j \left[(\tilde{\mathbb{L}}\beta)_{ij} - \tilde{u}_{ij} \right] - \frac{\psi}{4} \tilde{h}^{ij} \tilde{\nabla}_i \tilde{s}_j + \frac{1}{6} K \psi^3. \tag{5.13}$$

Finally, Eq. (5.9g)—which forces the apparent horizon to be in equilibrium—restricts $\beta^i_{||}$ to be a conformal Killing vector within the surface $\mathcal{S}$,

$$(\tilde{\mathbb{L}}_{\mathcal{S}} \beta_{||})^{ij} \equiv 2\tilde{D}^{(i} \beta^{j)}_{||} - \tilde{h}^{ij} \tilde{D}_k \beta^k_{||} = 0, \tag{5.14}$$

where $\tilde{D}_i$ is the covariant derivative compatible with $\tilde{h}_{ij}$. As discussed in detail in [17, 20], $\beta^i_{||}$ controls the spin of the black holes *in addition* to the spin required for co-rotation.

Quasi-equilibrium considerations have now led us to choices for half of the free data ($\tilde{u}_{ij}$ and $\partial_t K$) for the XCTS equations, and for all boundary conditions except a lapse boundary condition on the horizon $\mathcal{S}$. As argued in [17], Eqs. (5.9a)–(5.9e) are compatible with any spin of the black holes, with any choice of boundary conditions for the lapse on $\mathcal{S}$, and with any choice of $\tilde{\gamma}_{ij}$ and K.

For concreteness, we choose

$$\tilde{\gamma}_{ij} = f_{ij}, \tag{5.15a}$$

$$K = 0, \tag{5.15b}$$

$$\partial_r(\alpha\psi) = 0 \quad \text{on } \mathcal{S}, \tag{5.15c}$$

where f_{ij} is the Euclidean metric. The last two conditions, Eqs. (5.15b) and (5.15c), are gauge choices [17]. The choice of the conformal metric, however, does influence the physical gravitational radiation degrees of freedom of the system. Since a black hole binary is not conformally flat at second post-Newtonian order [30], our simple choice of conformal flatness, Eq. (5.15a), is probably responsible for the initial burst of unphysical gravitational radiation found in the evolution of these initial data.

5.2.2 Initial data in an asymptotically inertial frame

It is possible to re-formulate the quasi-equilibrium method in asymptotically inertial coordinates in such a way that identical physical initial data are obtained. To do so, we solve the XCTS Eqs. (5.8a)–(5.8c) with the same choices for the free data and boundary conditions, except that Eqs. (5.9d) and (5.9e) are replaced by

$$\beta^i \to 0 \;\text{ as } r \to \infty, \tag{5.16a}$$

$$\partial_t + \xi^i_{\text{rot}}\partial_i \quad \text{is tangent to } \mathcal{S}_{\text{AH}}, \text{ where } \xi^i_{\text{rot}} = (\mathbf{\Omega_0} \times \mathbf{r})^i. \tag{5.16b}$$

The second condition implies that the apparent horizons move initially with velocity ξ^i_{rot}, i.e., tangent to circular orbit trajectories.

Let $(\psi_{\text{co}}, \beta^i_{\text{co}}, \alpha_{\text{co}})$ be the solution to the XCTS equations in the co-rotating coordinates. We show in 5.7 that the solution in the asymptotically inertial coordinates is $(\psi, \beta^i, \alpha) = (\psi_{\text{co}}, \beta^i_{\text{co}} - \xi^i_{\text{rot}}, \alpha_{\text{co}})$, and that this solution leads to the same physical metric γ_{ij} and extrinsic curvature K_{ij} as the original solution in co-rotating coordinates. The proof of this relies on two observations: First, the shift enters the XCTS equations and the boundary conditions (almost) solely through the conformal Killing operator, $(\tilde{\mathbb{L}}\beta)^{ij}$; and second, ξ^i_{rot} is a conformal Killing vector, $(\tilde{\mathbb{L}}\xi_{\text{rot}})^{ij} = 0$, for the conformally flat case considered here. Hence the term $-\xi^i_{\text{rot}}$ that is added to β^i_{co} drops out of the equations.

In 5.7, we also show that Eq. (5.16b) and the shear condition Eq. (5.9g) require the shift on the inner boundary $\mathcal{S}$ to take the form

$$\beta^i = \alpha s^i - \xi^i_{\text{rot}} + \zeta^i \quad \text{on } \mathcal{S}, \tag{5.17}$$

where ζ^i is a vector that must be tangent to $\mathcal{S}$ ($\zeta^i s_i = 0$) and must be a conformal Killing vector within the surface $\mathcal{S}$:

$$\sigma_{ij} = 0 \quad \Leftrightarrow \quad 0 = (\tilde{\mathbb{L}}_{\mathcal{S}}\zeta)^{ij}. \tag{5.18}$$

Comparing Eq. (5.17) with Eq. (5.12), we see that the vector ζ^i plays the role of $\beta^i_{||}$ in the earlier treatment; choosing it as a rotation within $\mathcal{S}$ will impart additional spin to the black holes in addition to co-rotation, as described in detail in [20]. Note that at large radii the comoving shift β^i_{co} is a pure rotation, since $\beta^i_{\mathrm{co}} \to \xi^i_{\mathrm{rot}}$ [Eq. (5.16a)] and $\nabla^j \xi^i_{\mathrm{rot}}$ is antisymmetric [Eq. (5.16b)].

5.2.3 Initial data with nonzero radial velocity

After rewriting the standard quasi-equilibrium method in an asymptotically inertial frame, it is straightforward to incorporate nonzero initial radial velocities for the black holes. As discussed in Sec. 5.2.2, quasi-circular initial data can be generated by specifying that the horizons move initially on circles in an asymptotically inertial coordinate system. This is accomplished by the shift boundary conditions in Eqs. (5.16a) and (5.16b). We include initial radial velocities simply by requiring the black holes to move initially on inspiral rather than circular trajectories.

Consider the problem of giving a black hole located a distance r_0 from the origin an initial radial velocity v_r. This can easily be accomplished by replacing the boundary conditions in Eqs. (5.16a) and (5.16b) with

$$\beta^i \to 0 \ \text{ as } r \to \infty, \tag{5.19a}$$

$$\partial_t + \xi^i_{\mathrm{insp}}\partial_i \ \text{ is tangent to } \mathcal{S}_{\mathrm{AH}}, \text{ where } \xi^i_{\mathrm{insp}} \equiv (\mathbf{\Omega_0} \times \mathbf{r})^i + v_r \frac{r^i}{r_0}. \tag{5.19b}$$

As before, we place the center of rotation at the origin of the coordinate system. Note that ξ^i_{insp} is still a conformal Killing vector, $(\tilde{\mathbb{L}}\xi_{\mathrm{insp}})^{ij} = 0$, for the conformally flat case considered here. Therefore the analysis in 5.7 of the boundary conditions in Eqs. (5.16b) and (5.9g) also applies to Eqs. (5.19b) and (5.9g), and so we find that the inner shift boundary condition must be of the form

$$\beta^i = \alpha s^i - \xi^i_{\mathrm{insp}} + \zeta^i, \quad \text{on } \mathcal{S}, \tag{5.20}$$

where ζ^i is a conformal Killing vector within $\mathcal{S}$.

The boundary conditions in Eqs. (5.19a) and (5.19b) depend on two parameters, the orbital frequency Ω_0 and a radial velocity v_r (or, more precisely, an overall expansion factor v_r/r_0, reminiscent of the Hubble constant). For unequal mass binary systems the needed radial velocities for each hole would be different, but the needed expansion factors, v_r/r_0, are expected to be the same for the two holes.

The changes discussed in Sec. 5.2.2 are superficially similar to the changes discussed in Sec. 5.2.3, yet the former amounts to a mere coordinate transformation while the latter produces different physical initial data. This can be understood by noting that the change from co-rotating coordinates [Eqs. (5.9d) and (5.9e)] to inertial coordinates [Eqs. (5.16a) and (5.16b)] is accomplished by adding the *same* conformal Killing vector field $\xi^i_{\rm rot}$ to the shift at both inner and outer boundaries, but the change from Eqs. (5.9d) and (5.9e) to initial data with nonzero radial velocity [Eqs. (5.19a) and (5.19b)] is accomplished by adding *different* conformal Killing fields to the shift on different boundaries: $\xi^i_{\rm rot}$ at the outer boundary and $\xi^i_{\rm insp}$ at the inner boundaries. Only in the former case can the change be expressed as a global transformation of the shift of the form $\beta^i \to \beta^i + \xi^i_{\rm rot}$.

5.3 Numerical methods

The initial value equations are solved with the pseudo-spectral elliptic solver described in [31]. This elliptic solver has been updated to share the more advanced infrastructure of our evolution code and is now capable of handling cylindrical subdomains. This increases its efficiency by about a factor of three over the results described in [31] for binary black hole initial data.

The Einstein evolution equations are solved with the pseudo-spectral evolution code described in [6]. This code evolves a first-order representation [32] of the generalized harmonic system [33, 34]. We use boundary conditions [32] designed to prevent the influx of unphysical constraint violations and undesired incoming gravitational radiation, while allowing the outgoing gravitational radiation to pass freely through the boundary. The code uses a fairly complicated domain decomposition. Each black hole is surrounded by three concentric spherical shells, with the inner boundary of the inner shell just inside the horizon. The inner shells overlap a structure of 24 touching cylinders, which in turn overlap a set of outer spherical shells—centered at the origin—which extend to a large outer radius. Outer boundary conditions are imposed only on the outer surface of the largest outer spherical shell. We vary the location of the outer boundary by adding more shells at the outer edge. Since all outer shells have the same angular resolution, the cost of placing the outer boundary farther away (at full resolution) increases only linearly with the radius of the boundary. Some of the details of the domain decompositions used for the simulations presented here are given in Table 5.1.

5.4 Choice of orbital frequency and radial velocity

We now describe how to construct binary black hole initial data sets with low orbital eccentricity. This is done by tuning the freely adjustable orbital parameters Ω_0 and v_r iteratively to reduce the eccentricity of the inspiral trajectories. For each iteration we choose trial orbital parameters Ω_o and v_r, evolve the corresponding initial data, analyze the resulting trajectories of the black holes, and update the orbital parameters to reduce any oscillatory behavior in quantities like the coordinate separation of the black holes $d(t)$, the proper separation between the horizons $s(t)$, or the orbital frequency $\omega(t)$. All of these quantities (and many others) exhibit similar oscillatory behavior; we choose $d(t)$ as our primary diagnostic during the tuning process because it is most easily accessible during the evolutions.

To make this procedure quite explicit, we begin by evolving quasi-circular initial data for about two orbits. Then we measure the time derivative of the measured coordinate separation of the holes $\dot{d}(t)$ (in the asymptotic inertial coordinates used in our code [6]) as illustrated, for example, in Fig. 5.3. We fit this measured $\dot{d}(t)$ to a function of the form:

$$\dot{d}(t) = A_0 + A_1 t + B\sin(\omega t + \varphi), \tag{5.21}$$

where A_0, A_1, B, ω, and φ are constants determined by the fit. The $A_0 + A_1 t$ part of the solution represents the smooth inspiral, while the $B\sin(\omega t+\varphi)$ part represents the unwanted oscillations due to the eccentricity of the orbit. For a nearly circular Newtonian orbit, B is related to the eccentricity e of the orbit by $e = B/\omega d$. So reducing the orbital eccentricity is equivalent to reducing B. The values of the orbital parameters Ω_0 and v_r are now adjusted iteratively to make the coefficient B in this fit as small as desired. After each adjustment of Ω_0 and v_r, the initial value equations described in Sec. 5.2 [in particular, using the boundary condition (5.19b) which depends on Ω_0 and v_r] are solved completely (to the level of numerical truncation error).

For this paper, our goal is to reduce B, and hence the orbital eccentricity, by about a factor of ten compared to quasi-circular initial data. This level of reduction is sufficient to allow us to evaluate the significance of the orbital eccentricity inherent in quasi-circular initial data. A variety of methods could be used to find orbital paramters that make B small. One possibility is simply to evaluate $B(\Omega_0, v_r)$ numerically as described above, and then to use standard numerical methods to solve the equation $B(\Omega_0, v_r) = 0$. Since our goal in this paper is to reduce B by about a factor of ten, simple bisection root finding methods are sufficient.

A more efficient method is to use our knowledge of the behavior of nearly circular orbits to make informed estimates of the needed adjustments in the orbital parameters. Evaluating the fit Eq. (5.21) at the initial time $t = 0$, we see that the ellipticity-related component $B\sin(\omega t + \varphi)$ contributes $B\sin(\varphi)/2$ to the radial velocity of each hole and $B\omega\cos(\varphi)/2$ to its radial acceleration. (The factor 1/2 arises because d measures the distance between the holes.) For a Newtonian binary, this eccentricity-induced radial velocity can be completely removed by changing the initial radial velocity by

$$\delta v_r = -\frac{B\sin(\varphi)}{2}. \tag{5.22}$$

Furthermore, changing the orbital frequency Ω_0 by a small amount $\delta\Omega_0$ changes the radial acceleration of each black hole by the amount $\Omega_0 \delta\Omega_0 d_0$, where $d_0 = d(0)$ is the initial separation of the

Table 5.1: Summary of evolutions presented in this paper. The labels 'QC,' 'E,' and 'F' refer to the different initial data sets, with numerical suffix ('E1,' 'E2,' etc.) denoting different values of the initial outer boundary radius of the evolutions, $R_{\rm outer}$.

Label	Initial data	$\frac{R_{\rm outer}}{M_{\rm ADM}}$	# outer shells	approx # of points		
				low	med.	high
QC	$M_{\rm ADM}\Omega_0 = 0.029792,\ v_r = 0.0$	133	8	52^3	64^3	76^3
	$J_{\rm ADM}/M_{\rm ADM}^2 = 0.98549$					
	$M_{\rm irr}/M_{\rm ADM} = 0.50535$					
E1	$M_{\rm ADM}\Omega_0 = 0.029961,\ v_r = -0.0017$	171	10	59^3	66^3	74^3
E2	$J_{\rm ADM}/M_{\rm ADM}^2 = 0.99172$	293	18	64^3	72^3	81^3
	$M_{\rm irr}/M_{\rm ADM} = 0.50524$					
F1	$M_{\rm ADM}\Omega_0 = 0.029963,\ v_r = -0.0015$	133	8	52^3	64^3	76^3
F2	$J_{\rm ADM}/M_{\rm ADM}^2 = 0.99164$	190	12	55^3	66^3	78^3
F3	$M_{\rm irr}/M_{\rm ADM} = 0.50525$	419	28	62^3	74^3	87^3

holes. Thus the change $\delta\Omega_0$ needed to remove the eccentricity-induced initial radial acceleration, $B\omega\cos(\varphi)/2$, is

$$\delta\Omega_0 = -\frac{B\omega\cos(\varphi)}{2d_0\Omega_0} \approx -\frac{B\cos(\varphi)}{2d_0}. \tag{5.23}$$

Eqs. (5.22) and (5.23) still hold approximately for relativistic binaries. We have found that simultanously adjusting v_r and Ω_0 by Eqs. (5.22) and (5.23) typically reduces B by about a factor of ten.

The smallest eccentricity data set produced here (by the simple bisection method described above) is labeled 'F,' and the data from the next to last iteration of this method is labeled 'E.' These initial data sets, together with the quasi-circular data labeled 'QC' were evolved with multiple numerical resolutions and with multiple outer boundary locations; Table 5.1 summarizes these evolutions. The orbital frequency used in the final evolution is only 0.6 per cent larger than the value of Ω_0 used in the quasi-circular case. As expected, this change is comparible to the magnitude of the radial velocity v_r in the low eccentricity case. The smallness of these quantities shows that the quasi-circular approximation is quite good.

Fig. 5.2 shows the orbital phase (as measured by the coordinate locations of the centers of the apparent horizons) for the evolutions of quasi-circular initial data, QC, and the least-eccentric initial data, F1, F2, and F3. (The numerical suffix, F1, F2, etc., denotes simulations with different values of the outer boundary radius as defined in Table 5.1.) These evolutions proceed for about five orbits and then crash shortly before the black holes merge. The upper left inset shows differences between the orbital phase computed with different resolutions for the QC and the F2 runs. The phase difference between the high- and low-resolution runs is $\lesssim 0.35$ radians, which is a good estimate of the error in the low-resolution run. The phase difference between the medium- and high-resolution runs drops to ≈ 0.02 radians, which can be taken as the error in the medium-resolution run. Between low and medium resolutions, the error drops by about a factor of 20. Assuming exponential convergence,

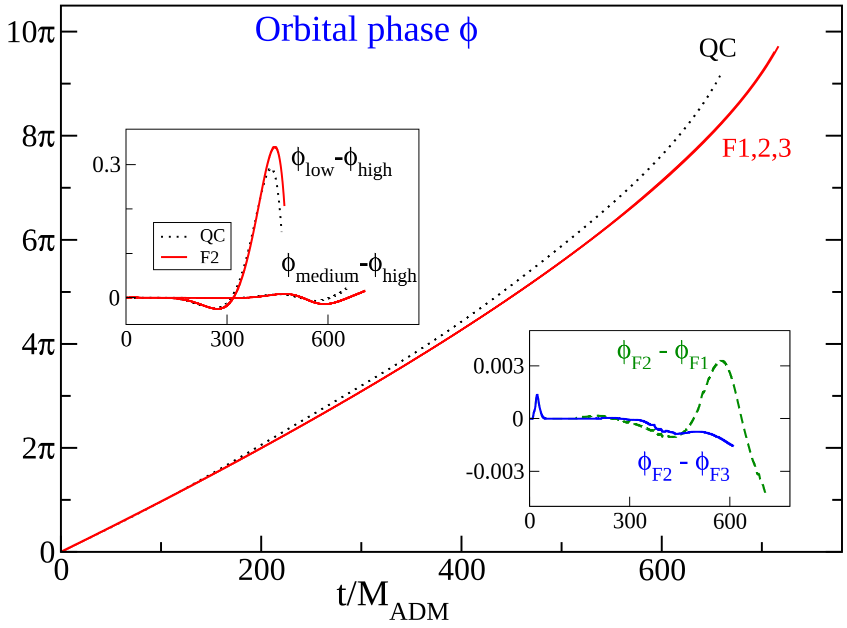

Figure 5.2: Evolution of the orbital phase. The main panel shows the phase of the trajectories of the centers of the apparent horizons as a function of time for the quasi-circular (dotted curves) and low-eccentricity (solid curves) initial data. The top left inset shows the phase differences between different resolution runs, which decreases at higher resolutions. The lower right inset shows the difference in the orbital phase between evolutions with different outer boundary locations.

the error of the high-resolution run should be smaller by yet another factor of ~ 20, i.e., $\lesssim 0.001$ radians. The lower right inset in Fig. 5.2 shows phase differences between evolutions of the same initial data, but run with different outer boundary radii. These differences are small, so we do not expect the influence of the outer boundary on our results to be significant. Our analysis in Sec. 5.5 is based mostly on comparisons between the high resolution QC and F2 runs.

Fig. 5.3 illustrates the radial velocities (determined from the time derivatives of both the coordinate and the intra-horizon proper separations) for the quasi-circular run QC and for the two low-eccentricity runs E and F. Orbital eccentricity causes periodic oscillations in these curves; the amplitudes of these oscillations are clearly much smaller in runs E and F than in run QC. By fitting the proper separation speed ds/dt to a linear function plus sinusoid, $ds/dt = A_0 + A_1 t + B\sin(\omega t + \varphi)$, the approximate amplitude of the oscillations can be estimated. We find $B_{\rm QC} \approx 5.5 \cdot 10^{-3}$, $B_{\rm E} \approx 5.8 \cdot 10^{-4}$, and $B_{\rm F} \approx 4.1 \cdot 10^{-4}$. This confirms that we have succeeded in our goal of reducing the oscillations by an order of magnitude. These fits are not very accurate because the fit must cover at least one period of the oscillations, and significant orbital evolution occurs during this time. If we vary the fit interval $40 < t/M_{\rm ADM} < T$ by choosing T between 300 and 450, the quoted amplitudes $A_{\rm QC,E,F}$ change at about the 10% level.

The coordinate separation $d(d)/dt$ shows some noise at early times as the binary system equilibrates and an initial burst of 'junk' gravitational radiation travels outward. There are also short-

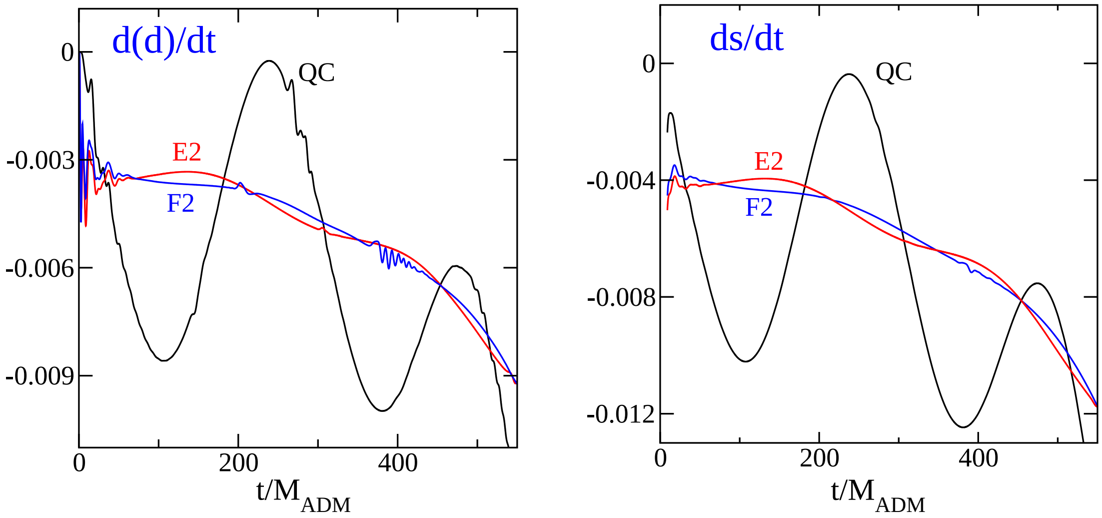

Figure 5.3: Radial velocity during evolutions of quasi-circular and low-eccentricity initial data. The left panel shows the coordinate velocity $\dot{d}(t)$, the right panel the velocity determined from the intra-horizon proper separation $\dot{s}(t)$.

lived, high-frequency features apparent in Fig. 5.3 at intermediate times. The earlier feature occurs at $t/M_{\mathrm{ADM}} \sim 140$ for the QC run, $t/M_{\mathrm{ADM}} \sim 200$ for F2, and $t/M_{\mathrm{ADM}} \sim 300$ for E2; these times coincide with the light-crossing time to the outer boundary. We believe that this early feature is caused by a small mismatch between the initial data and the outer boundary conditions used by the evolution code; this mismatch produces a pulse that propagates inward from the outer boundary starting at $t = 0$. A later (and larger) feature occurs at $t/M_{\mathrm{ADM}} \sim 280$ for the QC run, $t/M_{\mathrm{ADM}} \sim 400$ for F2, and at $t/M_{\mathrm{ADM}} \sim 600$ (off the scale of Fig. 5.3) for E2. This later feature occurs at twice the light-crossing time, and is caused by reflection of the initial 'junk' gravitational radiation burst off of the outer boundary. The outer boundary conditions used in this paper perform well for the physical gravitational-wave degrees of freedom [32], but comparatively poorly for the gauge degrees of freedom (as demonstrated in recent tests [35]). These results plus the observation that the high-frequency features in Fig. 5.3 are greatly diminished in less gauge-dependent quantities like ds/dt suggest that these features may be caused by perturbations in the gauge or coordinate degrees of freedom of the system.

Fig. 5.4 shows the orbital trajectories of the centers of the black holes during evolutions of the low-eccentricity initial data E [2], and the quasi-circular initial data QC. The low-eccentricity run forms a smooth spiral with no apparent distortion. In contrast, the evolution starting from quasi-circular initial data has clearly visible irregularities.

---

[2] We plot the evolution E1 because it was pushed somewhat closer to merger than the F runs; the trajectories of the E runs are indistinguishable from those of the F runs on the scale of this figure.

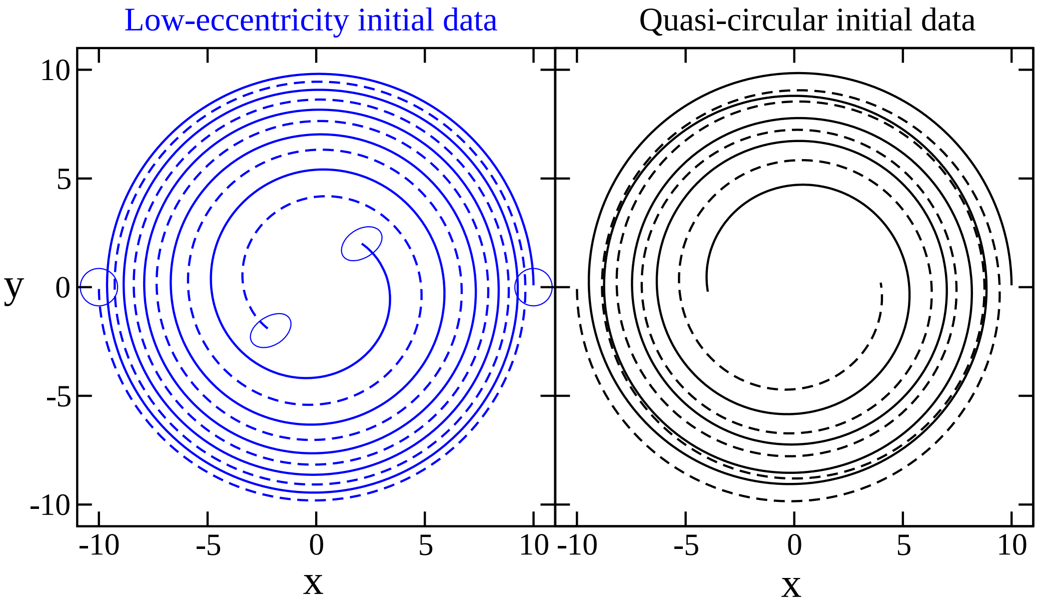

Figure 5.4: Trajectories of the center of the apparent horizons in asymptotically inertial coordinates for the runs E1 (left plot) and QC (right plot). The solid/dashed line distinguish the two black holes; the circles and ellipsoids in the left figure denote the location of the apparent horizon at the beginning and end of the evolution.

5.5 Comparing quasi-circular and low-eccentricity initial data

Figs. 5.3 and 5.4 show clearly that evolutions of the quasi-circular initial data, QC, are not the same as those of the low-eccentricity initial data, F. In this section, we characterize and quantify these differences in more detail.

5.5.1 Time shift

The black holes approach each other more quickly in the QC run, with the time of coalescence appearing to be about $60M_{\rm ADM}$ earlier than in the F2 run. Fig. 5.2, for example, shows that the orbital phase increases more quickly during the QC run, with a late time phase difference of about π (almost a full gravitational wave cycle) compared to the F2 run. Similar differences are also seen in the graphs of the proper separation and orbital frequency shown in the upper panels of Fig. 5.5.

We find that most of the difference between the QC and F runs is just a simple coordinate time shift. The dashed lines in the upper panels of Fig. 5.5 represent the QC evolution shifted by $\Delta T = 59M_{\rm ADM}$. With this time shift, the QC evolution oscillates around the low-eccentricity F2 run. Therefore, the apparent earlier merger time of the QC run is just a consequence of the fact that coordinate time $t = 0$ in the QC run represents a later stage in the inspiral than it does in the F2 evolution. The QC and F2 runs were started with the same spatial coordinate separation at $t = 0$; however, this point is the apocenter of the slightly eccentric QC orbit, so the point in the F2

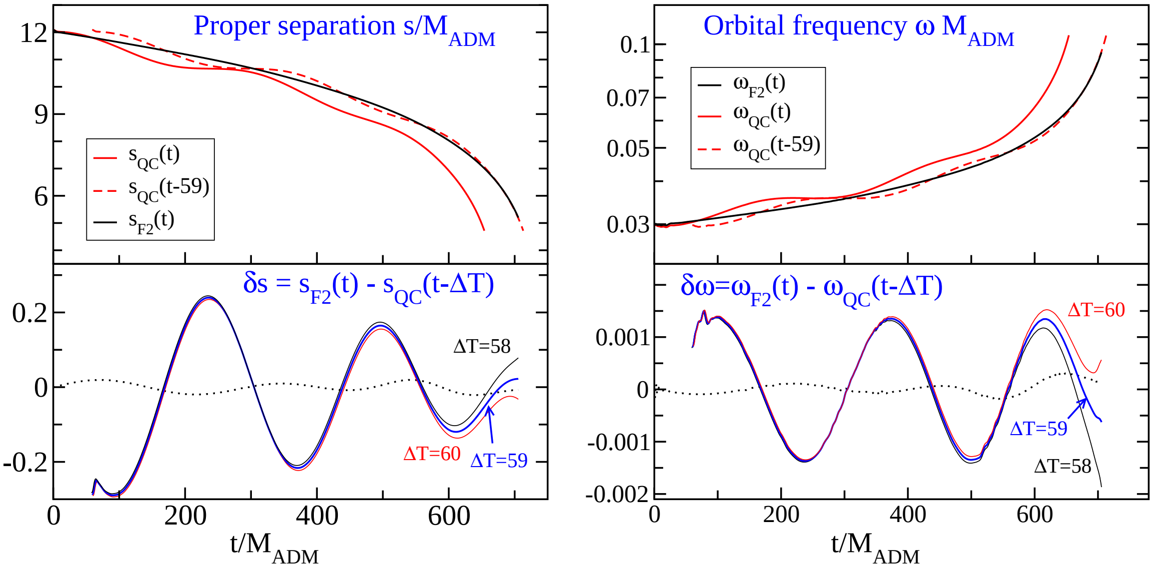

Figure 5.5: Proper separation (left) and orbital frequency (right) for evolutions of the QC and F initial data. The lower panels show the differences between the time-shifted QC and the F2 runs. The dotted lines in the lower panels show the differences between the E1 and F2 runs, providing an estimate of the remaining eccentricity in the F2 run.

run with the same phase (measured from merger) has smaller separation.

The lower left panel of Fig. 5.5 shows the proper separation difference, $\delta s = s_F(t) - s_{QC}(t - \Delta T)$, which emphasizes the oscillations of the QC evolution around the F2 orbit. These differences are plotted for three different time shifts ΔT. The right panels of Fig. 5.5 present information about the orbital angular frequency ω as determined from the coordinate locations of the centers of the apparent horizons. The upper right panel shows ω for evolutions of QC and F2 initial data. Time-shifting the QC run by the same $\Delta T = 59 M_{\rm ADM}$ also lines up the frequency curves very well. The lower right plot shows the difference in orbital frequency between the F2 run and the time-shifted QC run, $\delta\omega = \omega_{\rm F}(t) - \omega_{\rm QC}(t - \Delta T)$. The differences δs and $\delta\omega$ are very sensitive to the time offset ΔT applied to the QC run. In particular, at late times, when s and ω vary rapidly, even a small change in ΔT causes the differences to deviate significantly from their expected oscillatory behavior around zero. Looking at both δs and $\delta\omega$, we estimate a time offset $\Delta T / M_{\rm ADM} = 59 \pm 1$ between the QC run and the F runs.

5.5.2 Measuring eccentricity

The evolution of the F initial data appears to have very low orbital eccentricity, so it can be used as a reference from which the eccentricity of the QC run can be estimated. We can define an eccentricity

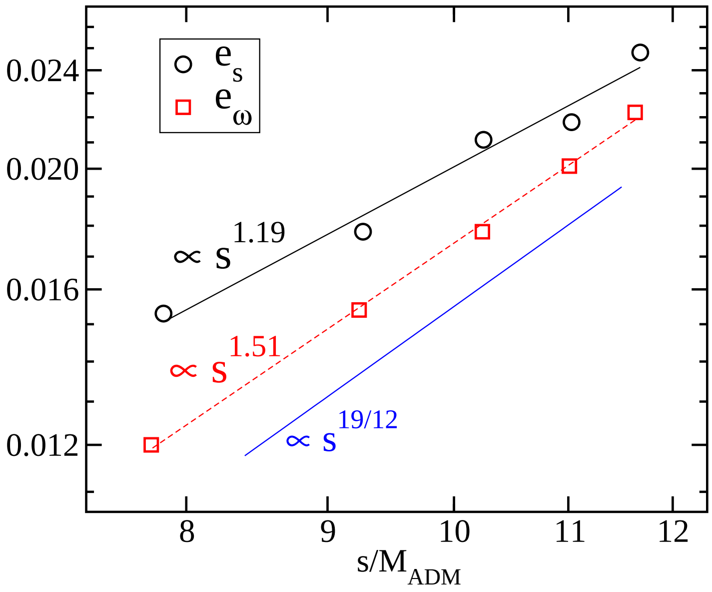

Figure 5.6: Orbital eccentricity of the QC evolution estimated from variations in proper separation, e_s, and from variations in orbital frequency, e_ω. Also shown in this log-log plot are best-fit power laws to each set of data, as well as the scaling predicted by Peters (1964) with power $19/12 \approx 1.58$.

for the QC evolution, for example, from the relative proper separation,

$$e_s = \frac{|\delta s|}{s}, \tag{5.24}$$

where this equation is to be evaluated at the extrema of δs. Similarly, we can define a different measure of eccentricity from the variations in ω_{orbit} by evaluating

$$e_\omega = \frac{|\delta\omega|}{2\omega} \tag{5.25}$$

at the extrema of $\delta\omega$. The factor of two in the definition of e_ω arises from angular momentum conservation, which makes the orbital frequency proportional to the square of the radius of the orbit. In Newtonian gravity, $e_s = e_\omega$ to first order in eccentricity. Since the F initial data results in a factor of ten smaller oscillations in ds/dt than the QC data, we expect these eccentricity estimates to be affected by the residual eccentricity of the F run at only the 10% level.

The orbital eccentricity of the QC run, estimated using Eqs. (5.24) and (5.25), is plotted as a function of proper separation between the black holes in Fig. 5.6. We see that these eccentricities decay during the inspiral, as expected. Within our estimated 10% errors, these eccentricities are consistent with a power law dependence on the proper separation, $e \propto s^p$. The eccentricity e_s based on the proper separation is consistently somewhat larger than e_ω, and it decays somewhat more slowly. Peters [8] derived the evolution of the orbital eccentricity during an inspiral due to the emission of gravitational waves using the quadrupole approximation. His result in the $e \ll 1$ limit predicts that $e \propto a^{19/12}$, where a is the semi-major axis of the orbit and where the constant of proportionality depends on the initial conditions. Using $a \approx s/2$, his formula predicts that the eccentricity should decay as

$$e \propto s^{19/12}. \tag{5.26}$$

Fig. 5.6 confirms that e_ω follows this prediction quite closely, while e_s has a somewhat smaller power law exponent.

The eccentricities measured here are actually the relative eccentricities of the QC and the F orbits. The eccentricity of the QC run that we infer depends therefore on the residual eccentricity of the F run. A more intrinsic approach, used recently by Buonanno et al. [27], is to fit some eccentricity-dependent quantity to a full cycle (or more) of the orbital data. This approach yields similar, but somewhat smaller, eccentricities than those found here (despite our use of a QC orbit having larger initial separation and so presumably smaller initial eccentricity).

5.5.3 Waveform extraction

We now turn our attention to the problem of extracting the gravitational wave signals from our numerical simulations using the Newman-Penrose quantity Ψ_4. Given a spatial hypersurface with timelike unit normal n^μ, and given a spatial unit vector r^μ in the direction of wave propagation, the standard definition of Ψ_4 is the following component of the Weyl curvature tensor,

$$\Psi_4 = -C_{\alpha\mu\beta\nu}\ell^\mu\ell^\nu\bar{m}^\alpha\bar{m}^\beta, \tag{5.27}$$

where $\ell^\mu \equiv \frac{1}{\sqrt{2}}(n^\mu - r^\mu)$, and m^μ is a complex null vector (satisfying $m^\mu\bar{m}_\mu = 1$) that is orthogonal to r^μ and n^μ. Here an overbar denotes complex conjugation.

For (perturbations of) flat spacetime, Ψ_4 is typically evaluated on coordinate spheres, and in this case the usual choices for r^μ and m^μ are

$$r^\mu = \left(\frac{\partial}{\partial r}\right)^\mu, \tag{5.28a}$$

$$m^\mu = \frac{1}{\sqrt{2}r}\left(\frac{\partial}{\partial\theta} + i\frac{1}{\sin\theta}\frac{\partial}{\partial\phi}\right)^\mu, \tag{5.28b}$$

where (r, θ, ϕ) denote the standard spherical coordinates. With this choice, Ψ_4 can be expanded in terms of spin-weighted spherical harmonics of weight -2:

$$\Psi_4(t, r, \theta, \phi) = \sum_{lm} \Psi_4^{lm}(t, r)\, {}_{-2}Y_{lm}(\theta, \phi), \tag{5.29}$$

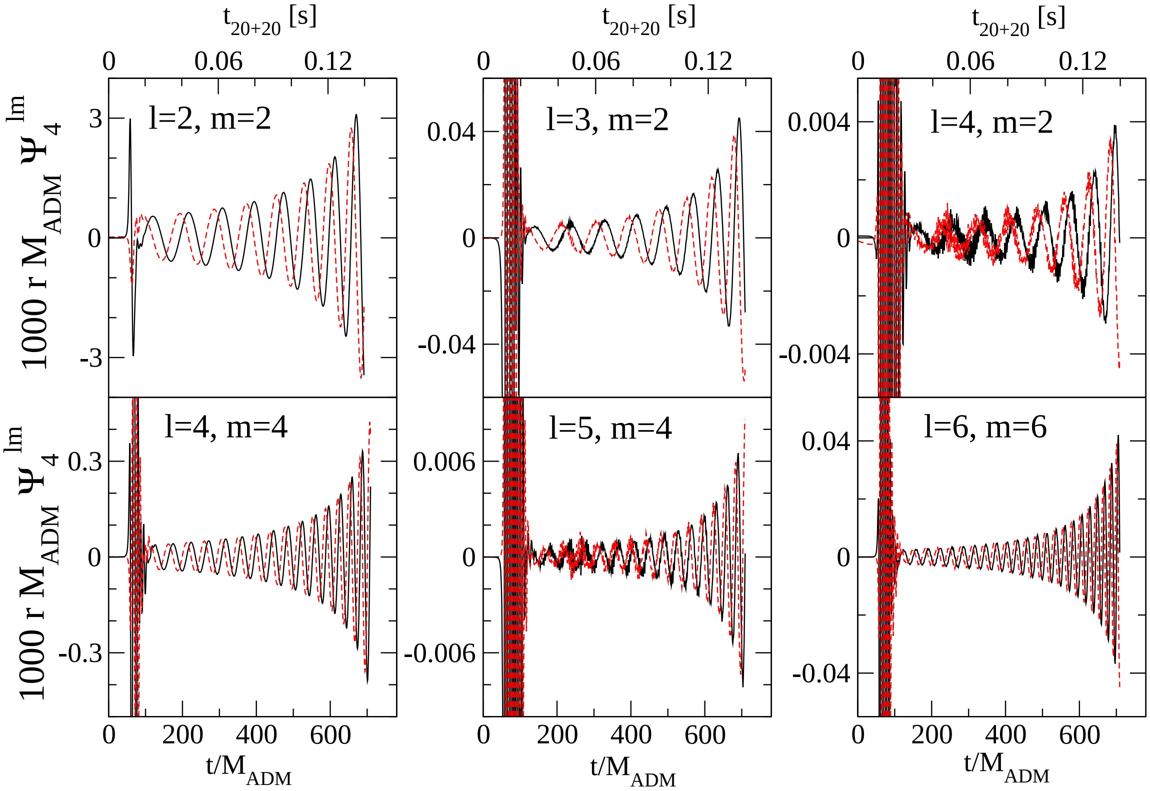

Figure 5.7: Waveforms for the F2 run. Plotted are the six dominant Ψ_4^{lm} coefficients, scaled by the factor $1000\, rM_{\mathrm{ADM}}$. Solid lines represent the real parts and dashed lines the imaginary parts of Ψ_4^{lm}. The time axes are labeled in geometric units at the bottom, and in SI units for a 20+20 $M_\odot$ binary at the top.

where the Ψ_4^{lm} are expansion coefficients defined by this equation.

For curved spacetime, there is considerable freedom in the choice of the vectors r^μ and m^μ, and different researchers have made different choices [27, 36, 37, 38, 39, 40, 7] that are all equivalent in the $r \to \infty$ limit. We choose these vectors by first picking an extraction two-surface $\mathcal{E}$ that is a coordinate sphere ($r^2 = x^2 + y^2 + z^2$) centered on the center of mass of the binary system (using the global asymptotically Cartesian coordinates employed in our code). We choose r^μ to be the outward-pointing spatial unit normal to $\mathcal{E}$ (that is, we choose r_i proportional to $\nabla_i r$). Then we choose m^μ according to Eq. (5.28b), using the standard spherical coordinates θ and ϕ defined on these coordinate spheres. Finally we use Eqs. (5.27) and (5.29) to define the Ψ_4^{lm} coefficients. Note that our m^μ is not exactly null nor exactly of unit magnitude at finite r, so our definition of Ψ_4^{lm} will disagree with the waveforms observed at infinity (and with those computed by other groups). Our definition does, however, agree with the standard definition given in Eqs. (5.27)–(5.29) as $r \to \infty$, so our definition only disagrees with the standard one by a factor of order $1 + \mathcal{O}(1/r)$. In this paper we compute Ψ_4^{lm} in the same way and at the same extraction radius for all runs, so the $\mathcal{O}(1/r)$ effects should not significantly affect our comparisons of these waveforms.

Since our simulations use high spatial resolution all the way to the outer boundary, the outgoing radiation is fully resolved everywhere. Therefore, we could extract waveforms at very large radii. The extracted wave signal lags the dynamics of the binary by the light-travel time to the extraction radius, and our evolutions currently fail shortly before merger. So extracting the wave signal at a very large radius would miss the most interesting part of the waveform close to merger. In order to retain most of the signal, we compromise by extracting the radiation at an intermediate distance: $R/M_{\text{ADM}} = 57$. Fig. 5.7 presents the dominant waveform coefficients Ψ_4^{lm}. The Ψ_4^{44} coefficient is about a factor of ten smaller than the largest coefficient, Ψ_4^{22}. The Ψ_4^{32} and Ψ_4^{66} coefficients are smaller by about another order of magnitude; and the Ψ_4^{42} and Ψ_4^{54} coefficients have amplitudes that are only about $\sim 1/1000$ that of Ψ_4^{22}.

5.5.4 Waveform comparisons

In this section we make a number of quantitative comparisons between the waveforms produced by the evolution of quasi-circular, QC, initial data and those produced by the lower eccentricity, F, initial data.

We can define a gravitational wave frequency associated with Ψ_4^{lm} by writing

$$\Psi_4^{lm} = A_{lm}(t)e^{-i\phi_{lm}(t)}, \tag{5.30}$$

where $A_{lm}(t)$ is its (real) amplitude and $\phi_{lm}(t)$ its (real) phase. The frequency, Ω_{lm}, associated with Ψ_4^{lm} is then defined as

$$\Omega_{lm} = \frac{d\phi_{lm}}{dt}. \tag{5.31}$$

Fig. 5.8 shows comparisons of the frequency of the dominant mode, Ω_{22}, from the QC and the F runs. This figure confirms the basic picture that emerged from our discussion in Secs. 5.5.1 and 5.5.2: a time offset Δt must be used to compare the QC and F runs properly; the QC run has an orbital eccentricity which causes Ω_{22} to oscillate; and these oscillations are largely absent from the F run. Indeed, apart from the factor of 2 difference between orbital and the gravitational wave frequencies, the top panel of Fig. 5.8 looks very much like Fig. 5.2. This indicates that our coordinates are very well behaved—a feature that has also been observed in other numerical simulations, e.g., [41].

In order to make more detailed comparisons between the QC and the F waveforms, a phase offset $\Delta\phi$ in addition to the time offset ΔT must be taken into account. These offsets are used then to redefine the waveform of the QC run:

$$\tilde{\Psi}_{4\,\text{QC}}^{lm}(t) \equiv e^{-im\Delta\phi}\;\Psi_{4\,\text{QC}}^{lm}(t-\Delta T). \tag{5.32}$$

The same time and phase offsets are used for all values of l and m. Note that $\Delta\phi$ and ΔT represent

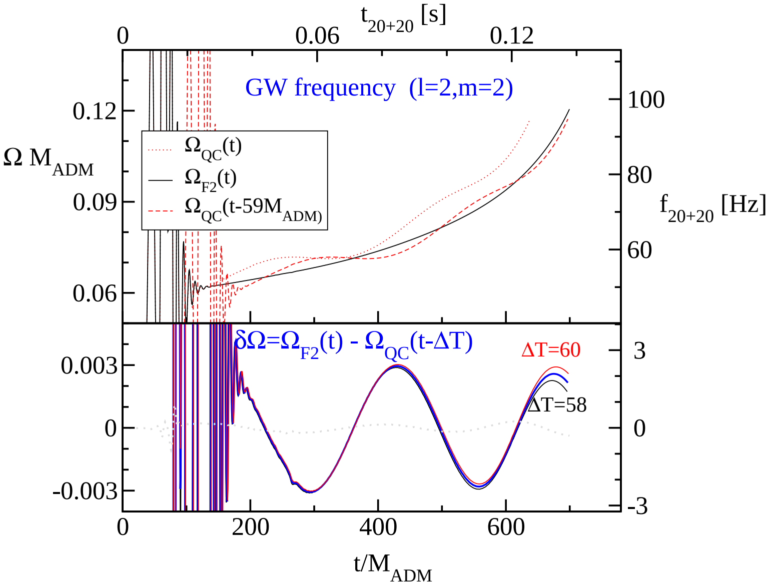

Figure 5.8: Frequency Ω_{22} of the gravitational waves extracted from the phase of Ψ_4^{22}. The left/bottom axes show geometric units, the right/top axes present SI-units for a 20+20 $M_\odot$ binary. The dotted line in the lower panel represents the difference between the E1 and F2 runs.

differences between the QC and F evolutions. These offsets differ therefore from those often used in LIGO data analysis, where offsets are used to set the time and orbital phase at which a binary signal enters the LIGO band at 40Hz.

We now estimate the phase offset $\Delta\phi$ needed in Eq. (5.32) to allow us to make direct comparisons between the QC and the F2 waveforms. We consider two effects: First, the orbital phase of the time-shifted QC run differs from that of the F2 run by the phase accumulated by the F2 run during the time $0 \leq t \leq \Delta T$. Second, the orbital frequencies of the QC and F2 runs differ, and this difference oscillates in time (cf. the right panel of Fig. 5.5), so the orbital phase difference between the two runs also oscillates in time. We take both of these effects into account: first, we evaluate the time-dependent phase difference, $\Delta\phi(t)$, between the waveforms of the time offset QC run, $\Psi_{4\,\mathrm{QC}}(t-\Delta t)$, and the F run, $\Psi_{4\,\mathrm{F}}(t)$; second, we evaluate the time average of this $\Delta\phi(t)$ to obtain $\Delta\phi \approx 1.83$. Using this value of $\Delta\phi$ leads to waveforms for the QC and F2 evolutions that agree as well as can be expected in the presence of the other systematic errors, described below.

The two gravitational wave polarizations, $h_+(t)$ and $h_\times(t)$, are the real functions related to Ψ_4 by

$$\Psi_4 = \ddot{h}_+ - i\ddot{h}_\times. \tag{5.33}$$

Consequently, the ${}_{-2}Y_{lm}$ components of $h_+(t)$ and $h_\times(t)$ can be obtained by the double time integral,

$$h_+^{lm}(t) - ih_\times^{lm}(t) = \int_{t_i}^{t} d\tau \int_{t_i}^{\tau} d\tau' \Psi_4^{lm}(\tau') + C_{lm} + D_{lm}t. \tag{5.34}$$

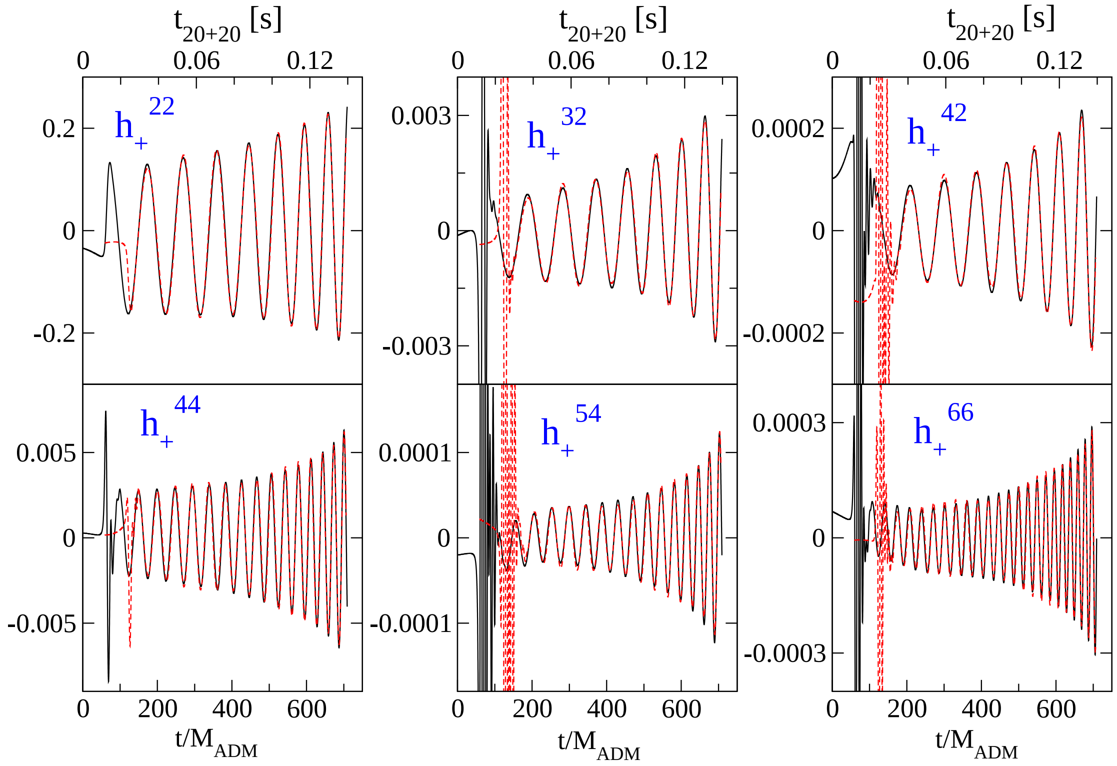

Figure 5.9: Waveforms h_+^{lm} (normalized by r/M_{ADM}) for the six dominant ${}_{-2}Y^{lm}$ modes. The solid lines represent evolution of the low-eccentricity initial data (run F2). The dashed lines represent evolution of QC initial data time-shifted by $\Delta T = 59M_{\mathrm{ADM}}$ and phase-rotated by $\Delta\phi = 1.83$. The time axes are labeled in geometric units at the bottom and in SI-units for a 20+20 $M_\odot$ inspiral at the top.

The constants C_{lm} and D_{lm} account for the (unknown) values of h and $\dot{h}$ at the initial time t_i. If the full waveform were known, they could be determined either at very early times or at very late times (i.e., after the merger and ringdown). Since we do not have complete waveforms for the present evolutions, we choose C_{lm} and D_{lm} that make the average and the first moment of $h_{+\times}^{lm}(t)$ vanish:

$$\int_{t_1}^{t_2} d\tau \, h_{+\times}^{lm}(\tau) = 0 = \int_{t_1}^{t_2} d\tau \, \tau \, h_{+\times}^{lm}(\tau). \tag{5.35}$$

The integration interval $[t_1, t_2] = [160M_{\mathrm{ADM}}, 706M_{\mathrm{ADM}}]$ is chosen to be the largest interval (excluding the initial transient radiation burst) on which data is available for both runs.

Fig. 5.9 shows the waveforms h_+^{lm} for the evolution F2 (solid lines) and QC (dashed lines). To the eye, the waveforms look essentially identical. To quantify how well the two waveforms match, we use simple overlap integrals in the time domain:

$$\mu = \frac{\langle h_1, h_2 \rangle}{||h_1|| \, ||h_2||}, \tag{5.36}$$

Table 5.2: Waveform overlaps between the low-eccentricity run F2 and quasi-circular run QC (computed from runs with medium and high resolution). Each mode of QC has been time shifted and rotated by $\Delta T = 59 M_{\rm ADM}$ and $\Delta\phi = 1.83$. These numbers are subject to additional systematic effects as discussed in the text.

	high resolution		medium resolution	
mode	$\mu(h^{lm}_{+F}, \bar{h}^{lm}_{QC+})$	$\mu(h^{lm}_{F\times}, \bar{h}^{lm}_{QC\times})$	$\mu(h^{lm}_{+F}, \bar{h}^{lm}_{QC+})$	$\mu(h^{lm}_{F\times}, \bar{h}^{lm}_{QC\times})$
l=2, m=2	0.998	0.998	0.998	0.998
l=3, m=2	0.997	0.997	0.997	0.998
l=4, m=2	0.996	0.997	0.996	0.998
l=4, m=4	0.991	0.991	0.993	0.993
l=5, m=4	0.987	0.979	0.983	0.982
l=6, m=6	0.981	0.980	0.986	0.982

where $\langle h_1, h_2\rangle \equiv \int_{t_1}^{t_2} dt\, h_1(t) h_2(t)$, and $||h||^2 \equiv \langle h, h\rangle$. The quantity μ gives the loss of signal to noise ratio obtained by filtering waveform h_1 with waveform h_2. We evaluate the overlap integral in the time domain, rather than the frequency domain, to allow us to truncate the waveforms easily to the interval $[t_1, t_2]$ during which both waveforms are available. During the evolutions presented here the gravitational-wave frequency changes by only a factor of two, so our decision not to weight by the LIGO noise spectrum should not change our results significantly for frequencies near the minimum of the noise curve. Furthermore, we evaluate μ directly for the different modes $h^{lm}_{+,\times}$, rather than for specific observation directions. This allows us to compare differences in the higher-order modes with smaller amplitudes, which would otherwise be swamped by the dominant $l = m = 2$ mode.

The overlaps between the QC and the F2 waveforms, obtained at $\Delta T = 59 M_{\rm ADM}$ and $\Delta\phi = 1.83$, are summarized in Table 5.2. Both medium- and high-resolution overlaps are given in Table 5.2, confirming that the overlaps are not dominated by numerical errors. We note, however, that the medium resolution runs have more noise in the higher order modes at early times; so we shortened the integration interval to $[t_1, t_2] = [200 M_{\rm ADM}, 706 M_{\rm ADM}]$ to avoid contamination in those waveforms.

The dominant uncertainty in the computed overlap μ arises because of our uncertainties in the integration constants C_{lm} and D_{lm} in Eqs. (5.34) and (5.35). Because the waveform has finite length, these constants are known only to an accuracy of $\sim 1/N_{\rm cyc}$, where $N_{\rm cyc}$ is the number of cycles in the waveform. This error depends only on the length of the evolution, and can only be reduced by longer evolutions, not by higher resolution evolutions. We show in 5.8 (to lowest order in the uncertainties of C_{lm} and D_{lm}) that the overlaps quoted in Table 5.2 are *upper* bounds. We also derive lower bounds for these overlaps there, which are smaller than the values given in Table 5.2 by about $12/(\pi N_{\rm cyc})^2$. So these lower bounds are about 0.02 smaller than the Table 5.2 values for the $m = 2$ modes, and 0.002 smaller for the $m = 6$ modes. This systematic uncertainty is much larger than the mismatch of the waveforms for the $m = 2$ modes, so maximizing the overlaps by varying ΔT and $\Delta\phi$ as independent parameters is not justified.

5.6 Discussion

In this paper, we have extended the quasi-equilibrium initial-data formalism to binary black holes with nonzero radial velocities. We have also used this formalism to construct initial data whose evolution results in very low eccentricity orbits: about an order of magnitude smaller than the orbits of quasi-circular initial data.

The main differences between evolutions of the quasi circular, QC, and the low eccentricity, F, initial data sets are overall time and phase shifts: the QC initial data represents the binary at a point closer to merger. When we correct for these shifts, the orbital trajectories of the black holes and the gravitational waveforms they produce agree very well between the two runs. Various parameters measured in the QC run (e.g., orbital frequency or proper separation) oscillate around the corresponding values from the F run. The gravitational wave phase oscillates as well, but no significant coherent phase difference builds up during the five orbits studied here. We find waveform overlaps between the high-eccentricity and low-eccentricity runs of about 0.99. Therefore it appears that for the last five orbits before merger the differences between quasi-circular and low-eccentricity initial data are not important for event detection in gravitational wave detectors. Longer evolutions (e.g., equal mass binaries starting at larger separation, as well as unequal mass binaries with a longer radiation reaction time scale) have more cycles during which phase shifts could, in principle, accumulate. However, orbital eccentricity tends to decay during an inspiral and the orbital eccentricity in quasi-circular data should decrease as the initial separation increases, so longer evolutions are probably less sensitive to the eccentricity in the initial data. Thus we anticipate that the eccentricity of quasi-circular initial data will not play a significant role when longer evolutions are used for event detection, but further study would be needed to confirm this.

Finally, we note that construction of low-eccentricity inspiral initial data may be more difficult when the black holes carry generic spin. The process described in this paper merely adjusts the orbital parameters to obtain a trajectory without oscillations on the orbital timescale. For non-spinning equal-mass black holes sufficiently far from merger, a non-oscillatory inspiral trajectory seems to be a reasonable choice. But if non-negligible spins are present, this is not likely to be the case. For spins that are not aligned with the orbital angular momentum, the approximate helical Killing vector is lost, and there are likely to be a variety of oscillations on the orbital time scale. In these cases a more sophisticated model of the desired circularized orbit will be needed before a procedure for adjusting the orbital parameters to the appropriate values can be formulated.

5.7 Appendix A: Quasi-equilibrium initial data in inertial coordinates

In this appendix we show that $(\psi_{\rm co}, \beta^i_{\rm co} - \xi_{\rm rot}, \alpha_{\rm co})$, where $\xi^i_{\rm rot} = (\mathbf{\Omega_0} \times \mathbf{r})^i$, is a solution to the XCTS Eqs. (5.8a)–(5.8c) in asymptotically inertial coordinates (with appropriately modified boundary conditions) whenever $(\psi_{\rm co}, \beta^i_{\rm co}, \alpha_{\rm co})$ is a solution in co-rotating coordinates. We also show that this solution leads to the same physical metric γ_{ij} and extrinsic curvature K_{ij} as the original solution in co-rotating coordinates. The proof relies on three key observations: First, both solutions are assumed to make the same choice of free data Eqs. (5.9a), (5.9b), (5.15a), and (5.15b); second, the shift enters the XCTS equations and the boundary conditions (almost) solely through the conformal Killing operator, $(\tilde{\mathbb{L}}\beta)^{ij}$; and third, $\xi^i_{\rm rot}$ is a conformal Killing vector, so $(\tilde{\mathbb{L}}\xi_{\rm rot})^{ij} = 0$. Hence the term $-\xi^i_{\rm rot}$ that is added to $\beta^i_{\rm co}$ (mostly) drops out of the equations.

We first show that the XCTS equations remain satisfied: Since $(\tilde{\mathbb{L}}\xi_{\rm rot})^{ij} = 0$, it follows from Eq. (5.5) that $\tilde{A}_{ij}$ is unchanged by the addition of $\xi^i_{\rm rot}$. So Eqs. (5.8a) and (5.8b) remain satisfied. The only other shift containing term in Eq. (5.8c) is $\beta^i\partial_i K$, which vanishes because $\partial_i K = 0$ from the choice of free data ($K = 0$) in Eq. (5.15b); so Eq. (5.8c) also remains satisfied.

We turn next to the boundary conditions: The boundary conditions used for the co-rotating coordinate representation of the XCTS equations are Eqs. (5.9c)–(5.9g) and (5.15c), while those used for the inertial frame representation are the same, except Eqs. (5.9d) and (5.9e) are replaced by Eqs. (5.16a) and (5.16b). The boundary conditions, Eqs. (5.9c) and (5.15c), depend only on ψ and α and therefore remain satisfied. The apparent horizon boundary condition, Eq. (5.9f), implies the boundary condition on the conformal factor Eq. (5.13), which is unchanged since $(\tilde{\mathbb{L}}\xi_{\rm rot})^{ij} = 0$; and the new outer boundary condition, Eq. (5.16a), also holds because $\beta^i_{\rm co}$ satisfies Eq. (5.9d).

The only remaining boundary conditions then are Eqs. (5.16b) and (5.9g). Because $\theta = 0$ and $\sigma_{ij} = 0$, the null surface generated by k^μ coincides with the world tube of the apparent horizons, $\mathcal{S}_{\rm AH}$. The normal to this null surface is k^μ, because k^μ is normal to $\mathcal{S}$ by construction, and because $k^\mu k_\mu = 0$. Therefore, in order for $\partial_t + \xi^i_{\rm rot}\partial_i$ to be tangent to $\mathcal{S}_{\rm AH}$, as required by the boundary condition Eq. (5.16b), it must be orthogonal to k^μ. The vector $\partial_t + \xi^i_{\rm rot}\partial_i$ has components $\alpha n^\mu + \beta^\mu + \xi^\mu_{\rm rot}$, where $\beta^\mu = [0, \beta^i]$ and $\xi^\mu_{\rm rot} = [0, \xi^i_{\rm rot}]$. Using $k^\mu = (n^\mu + s^\mu)/\sqrt{2}$, it follows that

$$0 = (\partial_t + \xi^i_{\rm rot}\partial_i) \cdot k = \frac{1}{\sqrt{2}}\left[-\alpha + (\beta^i + \xi^i_{\rm rot})s_i\right]. \tag{5.37}$$

This condition implies

$$\beta^i = \alpha s^i - \xi^i_{\rm rot} + \zeta^i \quad \text{on } \mathcal{S}, \tag{5.38}$$

with $\zeta^i s_i = 0$, i.e., Eq. (5.17) in the main text. So the boundary condition Eq. (5.16b) is satisfied because $\beta^i_{\rm co} = \alpha s^i + \zeta^i$ satisfies Eq. (5.12).

The vector ζ^i that appears in Eq. (5.38) is further constrained by the shear boundary condition, Eq. (5.9g), which we consider next. The shear σ_{ij} is defined as

$$\sigma_{\mu\nu} = \perp_{\mu\nu}{}^{\rho\sigma}\ {}^{(4)}\nabla_\rho k_\sigma, \tag{5.39}$$

where $\perp_{\mu\nu}{}^{\rho\sigma} = h_\mu{}^{(\rho} h_\nu{}^{\sigma)} - \frac{1}{2} h_{\mu\nu} h^{\rho\sigma}$. Substituting Eq. (5.11) into this expression, and subsequently using Eqs. (5.2), (5.4), and (5.5) results in

$$\sqrt{2}\sigma_{ij} = -\frac{1}{2\alpha} \perp_{ij}{}^{kl} \left[(\mathbb{L}\beta)_{kl} - \psi^4 \tilde{u}_{kl}\right] + \perp_{ij}{}^{kl} \nabla_k s_l. \tag{5.40}$$

For any vector field v^i decomposed into normal and tangential parts, $v^i = v^m s_m\, s^i + v^i_{||}$, it follows that

$$\perp_{ij}{}^{kl} (\mathbb{L}v)_{kl} = (\mathbb{L}_{\mathcal{S}} v_{||})_{ij} + 2 v^m s_m \perp_{ij}{}^{kl} \nabla_k s_l. \tag{5.41}$$

Using this identity and Eq. (5.17), the shear can be rewritten as

$$\sqrt{2}\sigma_{ij} = \frac{1}{2\alpha} \perp_{ij}{}^{kl} \left[(\mathbb{L}\xi_{\rm rot})_{kl} + \psi^4 \tilde{u}_{kl}\right] - \frac{1}{2\alpha} (\mathbb{L}_{\mathcal{S}}\zeta)_{ij}. \tag{5.42}$$

Once more, $\xi^i_{\rm rot}$ drops out because it is a conformal Killing vector. Also, since $\tilde{u}_{ij} = 0$ by Eq. (5.9a), we find that the shear vanishes if and only if ζ^i is a conformal Killing vector within the 2-surface $\mathcal{S}$:

$$\sigma_{ij} = 0 \quad \Leftrightarrow \quad 0 = (\mathbb{L}_{\mathcal{S}}\zeta)^{ij}. \tag{5.43}$$

Eq. (5.18) now follows from the identity $(\mathbb{L}_{\mathcal{S}}\zeta)^{ij} = \psi^{-4}(\tilde{\mathbb{L}}_{\mathcal{S}}\zeta)^{ij}$. This implies then that the boundary condition Eq. (5.9g) is satisfied since it is assumed to be satisfied in the co-rotating case.

Finally, we note that the physical metric γ_{ij} and extrinsic curvature K_{ij} produced by the inertial frame version of the problem are identical to those of the original co-rotating frame version. The conformal metric and conformal factor are identical in the two versions, so the physical metrics are identical trivially from Eq. (5.3). Since $\xi^i_{\rm rot}$ is a conformal Killing vector, it follows that A_{ij} is identical from Eq. (5.5); so it follows from Eq. (5.4) (with $K = 0$) that the extrinsic curvatures are identical as well.

5.8 Appendix B: Errors caused by finite-length waveforms

The error in the waveform overlaps caused by the uncertainty in the integration constants can be determined as follows: Denote our numerically computed waveforms by $h_x + \varepsilon_x$, where h_x stands for the unknown "true" waveform obtained with the correct values of the integration constants, and ε_x represents the error introduced by computing these constants with a truncated waveform. The label x stands for either F or QC.

The quantity of interest is the overlap between the "true" waveforms,

$$\mu(h_F, h_{QC}) = \frac{\langle h_F, h_{QC}\rangle}{||h_F||\,||h_{QC}||}, \tag{5.44}$$

where $\langle h_1, h_2\rangle \equiv \int_{t_1}^{t_2} h_1(t)h_2(t)dt$, and $||h||^2 \equiv \langle h, h\rangle$. The errors ε_x are those caused by the uncertainty in the constants C_{lm} and D_{lm} in Eq. (5.34), and the ε_x are therefore *linear* functions of time. Furthermore, choosing the integration constants by Eq. (5.35) makes the numerical waveforms $h_x+\varepsilon_x$ *orthogonal* to functions linear in time, so that $\langle h_x+\varepsilon_x, \varepsilon_y\rangle = 0$, where $x, y \in \{F, QC\}$. Using this result, and neglecting terms of order $\mathcal{O}(\varepsilon^3)$, one finds

$$\begin{aligned} \mu(h_F+\varepsilon_F, h_{QC}+\varepsilon_{QC}) \;&=\; \mu(h_F, h_{QC}) \\ &+\mu(h_F, h_{QC})\left(\frac{||\varepsilon_F||^2}{2||h_F||^2} + \frac{||\varepsilon_{QC}||^2}{2||h_{QC}||^2} - \frac{\langle\varepsilon_F, \varepsilon_{QC}\rangle}{||h_F||\,||h_{QC}||}\right). \end{aligned} \tag{5.45}$$

It is straightforward to show that $\mu(h_f, h_{QC}) = 1 - \mathcal{O}(\delta h^2)$ where $\delta h = h_F - h_{QC}$. Therefore, replacing $\mu(h_F, h_{QC}) \to 1$ in the last term of Eq. (5.45) changes the result only by terms of order $\mathcal{O}(\delta h^2\, \varepsilon_x^2)$. Furthermore, replacing $||h_{QC}|| \to ||h_F||$ in the denominators of Eq. (5.45) affects the result only by terms of order $\mathcal{O}(\delta h\, \varepsilon^2)$. Neglecting both of these higher order contributions, we find

$$\mu(h_F+\varepsilon_F, h_{QC}+\varepsilon_{QC}) = \mu(h_F, h_{QC}) + \frac{||\varepsilon_F - \varepsilon_{QC}||^2}{2||h_F||^2}. \tag{5.46}$$

Because the last term is non-negative, the "true" overlap $\mu(h_F, h_{QC})$ is always smaller than the numerically computed overlap $\mu(h_F+\varepsilon_F, h_{QC}+\varepsilon_{QC})$. Using the triangle inequality, we can bound the last term in Eq. (5.46) by the error $||\varepsilon_x||^2/||h_x||^2$ in either the F or the QC waveform:

$$\frac{||\varepsilon_F - \varepsilon_Q||^2}{2||h_F||^2} \leq \frac{(||\varepsilon_F|| + ||\varepsilon_{QC}||)^2}{2||h_F||^2} \approx 2\frac{||\varepsilon_x||^2}{||h_x||}. \tag{5.47}$$

Finally, we estimate $||\varepsilon_x||^2/||h_x||^2$ by applying Eqs. (5.34) and (5.35) to a pure sine-wave: $h(t) = \sin(t)$. It is straightforward to evaluate the integrals in Eq. (5.35) for this simple case, giving the bound $||\varepsilon||^2/||h||^2 \leq 6/(\pi N_{\rm cyc})^2$, where $N_{\rm cyc} = (t_2-t_1)/(2\pi)$ is the number of cycles in the interval $[t_1, t_2]$. Therefore, we arrive at the bounds

$$\mu(h_F+\varepsilon_F, h_{QC}+\varepsilon_{QC}) \geq \mu(h_F, h_{QC}) \gtrsim \mu(h_F+\varepsilon_F, h_{QC}+\varepsilon_{QC}) - \frac{12}{\pi^2 N_{\rm cyc}^2}, \tag{5.48}$$

as mentioned in the main text.

5.9 Bibliography

[1] B. C. Barish and R. Weiss, Phys. Today **52 (Oct)**, 44 (1999).

[2] F. Acernese et al., Class. Quantum Grav. **19**, 1421 (2002).

[3] F. Pretorius, Phys. Rev. Lett. **95**, 121101 (2005), `gr-qc/0507014`.

[4] J. G. Baker, J. Centrella, D.-I. Choi, M. Koppitz, and J. van Meter, Phys. Rev. Lett. **96**, 111102 (2006).

[5] M. Campanelli, C. O. Lousto, P. Marronetti, and Y. Zlochower, Phys. Rev. Lett. **96**, 111101 (2006).

[6] M. A. Scheel, H. P. Pfeiffer, L. Lindblom, L. E. Kidder, O. Rinne, and S. A. Teukolsky, Phys. Rev. D **74**, 104006 (2006), `gr-qc/0607056`.

[7] B. Brügmann, J. A. Gonzalez, M. Hannam, S. Husa, U. Sperhake, and W. Tichy (2006), `gr-qc/0610128`.

[8] P. C. Peters, Phys. Rev. **136**, B1224 (1964).

[9] G. B. Cook, Phys. Rev. D **50**, 5025 (1994).

[10] T. W. Baumgarte, Phys. Rev. D **62**, 024018 (2000).

[11] E. Gourgoulhon, P. Grandclément, and S. Bonazzola, Phys. Rev. D **65**, 044020 (2002).

[12] P. Grandclément, E. Gourgoulhon, and S. Bonazzola, Phys. Rev. D **65**, 044021 (2002).

[13] B. D. Baker (2002), `gr-qc/0205082v1`.

[14] G. B. Cook, Phys. Rev. D **65**, 084003 (2002).

[15] W. Tichy, B. Brügmann, M. Campanelli, and P. Diener, Phys. Rev. D **68**, 064008 (2003).

[16] H. P. Pfeiffer, Ph.D. thesis, Cornell University (2003).

[17] G. B. Cook and H. P. Pfeiffer, Phys. Rev. D **70**, 104016 (2004).

[18] H.-J. Yo, J. N. Cook, S. L. Shapiro, and T. W. Baumgarte, Phys. Rev. D **70**, 084033 (2004), erratum-ibid. D70:089904 (2004).

[19] W. Tichy and B. Brügmann, Phys. Rev. D **69**, 024006 (2004), gr-qc/0307027.

[20] M. Caudill, G. B. Cook, J. D. Grigsby, and H. P. Pfeiffer, Phys. Rev. D **74**, 064011 (2006), `gr-qc/0605053`.

[21] K. A. Dennison, T. W. Baumgarte, and H. P. Pfeiffer, Phys. Rev. D **74**, 064016 (2006), `gr-qc/0606037`.

[22] N. Yunes, W. Tichy, B. J. Owen, and B. Bruegmann, Phys. Rev. D **74**, 104011 (2006).

[23] N. Yunes and W. Tichy, Phys. Rev. D **74**, 064013 (2006).

[24] J. Baker, M. Campanelli, C. O. Lousto, and R. Takahashi, Phys. Rev. D **65**, 124012 (2002).

[25] S. Brandt and B. Brügmann, Phys. Rev. Lett. **78**, 3606 (1997).

[26] M. Miller, Phys. Rev. D **69**, 124013 (2004).

[27] A. Buonanno, G. B. Cook, and F. Pretorius (2006), `gr-qc/0610122`.

[28] J. W. York, Jr., Phys. Rev. Lett. **82**, 1350 (1999).

[29] H. P. Pfeiffer and J. W. York, Phys. Rev. D **67**, 044022 (2003).

[30] R. Rieth, in *Mathematics of Gravitation. Part II. Gravitational Wave Detection*, A. Królak, Ed., (Polish Academy of Sciences, Institute of Mathematics, Warsaw, 1997), pp. 71–74.

[31] H. P. Pfeiffer, L. E. Kidder, M. A. Scheel, and S. A. Teukolsky, Comput. Phys. Commun. **152**, 253 (2003).

[32] L. Lindblom, M. A. Scheel, L. E. Kidder, R. Owen, and O. Rinne, Class. Quantum Grav. **23**, S447 (2006).

[33] H. Friedrich, Commun. Math. Phys. **100**, 525 (1985).

[34] F. Pretorius, Class. Quantum Grav. **22**, 425 (2005).

[35] O. Rinne, L. Lindblom, and M. A. Scheel (2007), arXiv:0704.0782.

[36] D. R. Fiske, J. G. Baker, J. R. van Meter, D.-I. Choi, and J. M. Centrella, Phys. Rev. D **71**, 104036 (2005).

[37] C. Beetle, M. Bruni, L. M. Burko, and A. Nerozzi, Phys. Rev. D **72**, 024013 (2005).

[38] A. Nerozzi, C. Beetle, M. Bruni, L. M. Burko, and D. Pollney, Phys. Rev. D **72**, 024014 (2005).

[39] L. M. Burko, T. W. Baumgarte, and C. Beetle, Phys. Rev. D **73**, 024002 (2006).

[40] M. Campanelli, B. J. Kelly, and C. O. Lousto, Phys. Rev. D **73**, 064005 (2006).

[41] F. Pretorius, Class. Quant. Grav. **23**, S529 (2006).

Chapter 6

Reducing junk radiation in binary-black-hole simulations

At early times in numerical evolutions of binary black holes, current simulations contain unphysical, spurious gravitational radiation (called "junk radiation"). The junk radiation is a consequence of how the binary-black-hole initial data are constructed: specifically, the initial data are typically assumed to be conformally flat. In this paper, I adopt a non-flat conformal metric that is a superposition of two boosted, non-spinning black holes that are approximately 15 orbits from merger. I extend the method of reducing the eccentricity of the holes' trajectories developed by Pfeiffer et al. (2007) to the non-conformally-flat case considered here. I compare junk radiation of the superposed-boosted-Schwarzschild (SBS) initial data with the junk of corresponding, conformally-flat (CF) initial data. The SBS junk is smaller in amplitude than the CF junk by a factor of order two.

6.1 Introduction

One of the most important sources of gravitational waves for LIGO [1] is the inspiral and merger of two black holes. LIGO is now taking data at design sensitivity and can detect stellar-mass binary-black-hole mergers as distant as about 100 megaparsecs [2]. The gravitational waveform of a binary-black-hole merger cannot be computed using analytic techniques but must be obtained by solving the Einstein equations numerically.

Recently, great progress in numerical relativity has been made, allowing several groups to evolve binary black holes, beginning at several orbits before merger [3, 4, 5, 6, 7]. These evolutions are based on splitting the four-dimensional spacetime into a series of three-dimensional spatial slices; to start an evolution, one must first construct initial data for the first slice. This initial data must i) represent the desired physical situation (i.e., two black holes about to merge), and ii) satisfy the vacuum Einstein constraint equations:

$$\begin{aligned} G_{00} &= 0, \\ G_{0j} &= 0. \end{aligned} \tag{6.1}$$

The time-time and time-space equations are called the Hamiltonian and momentum constraints, respectively. The vacuum Einstein evolution equations, $G_{ij} = 0$, are solved to step from the initial slice to subsequent slices.

There are several methods that generate constraint-satisfying initial data (for a review, see, e.g., [8] and [9]); however, these generally assume that the initial spatial metric g_{ij} is conformally flat:

$$g_{ij} = \psi^4 \delta_{ij}. \tag{6.2}$$

This simplifying assumption causes unphysical, spurious gravitational radiation (called *junk radiation*) to be present in the early phases of the simulation. Specifically, it is known that a stationary, isolated black hole with linear [10] or angular [11] momentum cannot be sliced so that the spatial metric is conformally flat. Attempting to construct constraint-satisfying, conformally flat initial data for boosted or spinning black holes yields holes that are not in equilibrium but are unphysically perturbed. As they relax to an equilibrium configuration, gravitational waves are emitted.

In general, the black holes in a binary have both linear and angular momentum; therefore, the binary black hole simulations will also contain junk radiation. Before one can extract the physically relevant gravitational wave signal, one must first evolve the unphysical system until the spurious waves have left the computational domain. Because these evolutions are computationally expensive, it is desirable to reduce the junk radiation as much as possible.

Hannam et al. [12] have constructed non conformally flat initial data to reduce the amount of junk radiation in head-on mergers of spinning holes; their non-flat metric is a superposition of two spinning black holes. Also, Kelly et al. [13] have constructed non-flat initial data that incorporates post-Newtonian waves into the initial data. In this chapter, I construct non conformally flat initial data for nonspinning black holes initially in a non-eccentric, inspiral orbit.

By using a metric that is a superposition of two *boosted* black holes, the spurious gravitational radiation is significantly reduced. Specifically, I will use a superposition of free data for analytic individual black-hole solutions to construct the free data for the binary. This is similar in spirit to the superposed-Kerr-Schild initial data proposed in [14]. However, I apply this superposition in the context of the conformal-thin-sandwich equations, and our analytic black-hole solutions are based on maximal slices of Schwarzschild rather than on Schwarzschild in Kerr-Schild coordinates.

I then combine these free data with quasiequilibrium boundary conditions developed by Cook [15], Cook and Pfeiffer [16], and Caudill et. al. [17]. I solve the constraint equations using the Caltech-Cornell pseudospectral code [18]. After reducing the eccentricity of the holes' orbits by extending the technique of Pfeiffer et. al. [19] to the non conformally flat case, I evolve the holes using the Caltech-Cornell code [20, 6].

The remainder of this paper is organized as follows. In Sec. 6.2, I summarize the formalism used in this paper to solve the initial value problem. In Sec. 6.3, I describe how to construct initial data whose conformal metric is a superposition of two boosted Schwarzschild black holes. In Sec. 6.4, I choose a conformally flat (CF) data set and a superposed-boosted-Schwarzschild (SBS) initial data set that is physically comparable. In particular, I use the eccentricity-reduction technique of [19] (originally developed under the assumption of conformal flatness) so that sets CF and SBS both have very little orbital eccentricity. In Sec. 6.4.1.2, the junk radiation of sets CF and SBS are compared. A brief conclusion is made in Sec. 6.5.

6.2 The initial value problem

6.2.1 The constraint equations

To construct constraint-satisfying initial data, I begin with the usual 3+1 split, in which the four-dimensional spacetime, with metric $g_{\mu\nu}$, is split into a series of three-dimensional spatial slices with spatial metric g_{ij}. The spacetime metric $g_{\mu\nu}$ is related to the spatial metric g_{ij}, the lapse α, and the shift β^i by

$$ds^2 = g_{\mu\nu} dx^\mu dx^\nu = -\alpha^2 dt^2 + g_{ij}(dx^i + \beta^i dt)(dx^j + \beta^j dt). \tag{6.3}$$

Here and throughout the rest of this paper, the Einstein summation convention is assumed. Greek indices refer to spacetime coordinates and are raised and lowered with the spacetime metric $g_{\mu\nu}$ and its inverse. Latin indices refer to spatial coordinates of a $t = const$ slice and are raised and lowered with the spatial metric g_{ij} and its inverse.

On the initial ($t = 0$) slice, the initial data must specify g_{ij} and the extrinsic curvature K_{ij}, which is essentially the rate of change of g_{ij} in the normal direction. The extrinsic curvature is related to the time derivative of the metric $\partial_t g_{ij}$ and to the lapse and shift by

$$\partial_t g_{ij} = -2\alpha K_{ij} + 2\nabla_{(i}\beta_{j)}. \tag{6.4}$$

The initial values of g_{ij} and K_{ij} must be chosen so that i) the solution contains the desired physical content, and ii) the constraint equations (6.1) are satisfied.

A systematic way to solve these equations is given by the extended conformal thin sandwich

(XCTS) formalism [21, 22]. In this formalism, one expands g_{ij} and K_{ij} as follows:

$$\begin{aligned} g_{ij} &= \psi^4 \tilde{g}_{ij}, \\ K_{ij} &= A_{ij} + \frac{1}{3} g_{ij} K. \end{aligned} \tag{6.5}$$

Then, one chooses the conformal metric $\tilde{g}_{ij}$, the trace of the extrinsic curvature K, and the time derivatives of both, $\tilde{u}_{ij} \equiv \partial_t \tilde{g}_{ij}$ and $\partial_t K$. The constraint equations (6.1) are then reduced to elliptic equations for the conformal factor ψ and the shift β^i. A fifth elliptic equation for $\alpha\psi$ determines the lapse; it is not a constraint, but appears because the free data include $\partial_t K$ instead of $\tilde{\alpha} \equiv \psi^{-6}\alpha$. (Alternatively, one could use the "standard" conformal thin sandwich equations [21, 22], in which the free data are $\tilde{g}_{ij}$, $\tilde{u}_{ij}$, K, and $\tilde{\alpha}$.)

Together, these equations form a second-order, nonlinear, coupled elliptic system called the extended conformal thin sandwich (XCTS) equations, which are (e.g., Eq. (8) of [19]):

$$\tilde{\nabla}^2 \psi - \frac{1}{8}\tilde{R}\psi - \frac{1}{12}K^2\psi^5 + \frac{1}{8}\psi^{-7}\tilde{A}^{ij}\tilde{A}_{ij} = 0, \tag{6.6a}$$

$$\tilde{\nabla}_j\Big(\frac{\psi^7}{2(\alpha\psi)}(\tilde{\mathbb{L}}\beta)^{ij}\Big) - \frac{2}{3}\psi^6\tilde{\nabla}^i K - \tilde{\nabla}_j\Big(\frac{\psi^7}{2(\alpha\psi)}\tilde{u}^{ij}\Big) = 0, \tag{6.6b}$$

$$\tilde{\nabla}^2(\alpha\psi) - (\alpha\psi)\left[\frac{\tilde{R}}{8} + \frac{5}{12}K^4\psi^4 + \frac{7}{8}\psi^{-8}\tilde{A}^{ij}\tilde{A}_{ij}\right] = -\psi^5(\partial_t K - \beta^k\partial_k K). \tag{6.6c}$$

Here $\tilde{\nabla}$ is the gradient with respect to $\tilde{g}_{ij}$, the "longitudinal operator" $\tilde{\mathbb{L}}$ is twice the symmetric, trace-free gradient (i.e., the "shear") with respect to $\tilde{g}_{ij}$, i.e.,

$$(\tilde{\mathbb{L}}V)_{ij} \equiv \tilde{\nabla}_i V_j + \tilde{\nabla}_j V_i - \frac{2}{3}\tilde{g}_{ij}\tilde{\nabla}_k V^k, \tag{6.7}$$

and

$$\tilde{A}^{ij} = \psi^{10}A^{ij} = \frac{\psi^7}{2(\alpha\psi)}\left[(\tilde{\mathbb{L}}\beta)^{ij} - \tilde{u}^{ij}\right]. \tag{6.8}$$

The initial value problem now amounts to i) choosing the free data ($\tilde{g}_{ij}$, $\tilde{u}_{ij}$, K, and $\partial_t K$), ii) choosing boundary conditions for ψ, $\alpha\psi$, and β^i, and iii) solving Eqs. (6.6a)–(6.6c) for ψ, $\alpha\psi$, and β^i. Most of these have preferred choices, motivated by the requirement that, in the comoving coordinates, the initial data contain two black holes at rest. These *quasiequilibrium* conditions will be discussed in the next subsection. The remaining quantities will be dealt with in Sec. 6.3.

6.2.2 Quasiequilibrium free data and boundary conditions

In the XCTS formalism described in the previous subsection, the physical content of the data is selected by the choice of both the free data ($\tilde{g}_{ij}$, K, and their time derivatives) and by the boundary conditions. We wish to make choices that represent the physical situation of two (otherwise isolated) black holes orbiting each other. In the quasiequilibrium method [23, 24, 15, 16, 17, 19] used in this paper, there are preferred choices for many of the free data and boundary conditions.

6.2.2.1 Free data

In quasiequilibrium initial data, the coordinates are required to (initially) be *comoving* with the black holes. If the holes are also in equilibrium, time derivatives in the comoving frame should initially be small. Quasiequilibrium initial data therefore choose

$$\tilde{u}_{ij} = 0, \tag{6.9}$$

$$\partial_t K = 0. \tag{6.10}$$

The remaining free data, $\tilde{g}_{ij}$ and K, can be chosen freely. In Sec. 6.3, I make particular choices for $\tilde{g}_{ij}$ and K.

6.2.2.2 Outer boundary conditions

The computational domain can be represented by only a finite number of gridpoints, so it necessarily will have an outer boundary $\mathcal{B}$, which here is taken to be a coordinate sphere whose radius R is so much larger than all other length scales that it is effectively "infinitely far away." (In practice, the outer boundary is roughly 10^9 times larger than the size of each black hole.) The physical requirement that the binary is isolated (i.e., that the spacetime is asymptotically flat) corresponds to the conditions

$$\psi = 1 \text{ on } \mathcal{B}, \tag{6.11}$$

$$\alpha = 1 \text{ on } \mathcal{B}, \tag{6.12}$$

provided that $\tilde{g}_{ij}$ is asymptotically flat.

The outer boundary condition on the shift is set by the requirement that the coordinates are initially comoving with the black holes. Therefore, in the asymptotically flat region—and in particular, on $\mathcal{B}$—the coordinates *will not be inertial*; instead, they will *rotate* (due to the orbital motion) and *contract* (due to the holes' inspiral). That is, if r is a coordinate radius measured from the system's center of energy, and if r^i is a radial position vector in the asymptotically flat region, then

$$\beta^i = (\mathbf{\Omega} \times r)^i + \frac{v_r}{r_o} r^i \text{ on } \mathcal{B}. \tag{6.13}$$

Here $r_o = d_o/2$, where d_o is the initial coordinate separation of the holes. The precise values of Ω and v_r will be set so that the holes' subsequent trajectories are not eccentric (Sec. 6.4.1.1).

6.2.2.3 Inner boundary conditions

The singularities of each black hole are excised from the computational domain. The excision surface $\mathcal{S}$ is the apparent horizons $\mathcal{H}$ of the two holes (labeled "A" and "B"), i.e., $\mathcal{S} = \mathcal{H}_A \bigcup \mathcal{H}_B$. This requirement leads to a boundary condition on the conformal factor (Eq. (13) of [19]):

$$\tilde{s}^k \partial_k \psi = -\frac{\psi^{-3}}{8\tilde{\alpha}} \tilde{s}^i \tilde{s}^j \left[(\tilde{\mathbb{L}}\beta)_{ij} - \tilde{u}_{ij} \right] - \frac{\psi}{4} \tilde{h}^{ij} \tilde{\nabla}_i \tilde{s}_j + \frac{1}{6} K \psi^3 \text{ on } \mathcal{S} \tag{6.14}$$

where s^i is an outward-pointing[1] unit normal vector on $\mathcal{S}$, and $h_{ij} = g_{ij} - s_i s_j = \psi^4 \left(\tilde{g}_{ij} - \tilde{s}_i \tilde{s}_j\right) = \psi^4 \tilde{h}_{ij}$ is the induced metric on $\mathcal{S}$.

When the initial data are evolved in the comoving system, the apparent horizon (itself in equilibrium) should remain at rest. This leads to the following boundary condition on the shift (Eq. (12) of [19]):

$$\beta^i = \alpha s^i + \Omega_r \xi^i \text{ on } \mathcal{S}. \tag{6.15}$$

Here Ω_r is a parameter that determines the amount of spin on the hole *in addition to corotation*, and ξ^i is a conformal Killing vector within $\mathcal{S}$. (If the holes are to have different spins, different values of Ω_r are used on $\mathcal{H}_A$ and $\mathcal{H}_B$.) The $(k)^{\text{th}}$ component of the quasilocal spin [25, 26, 27] of each hole can be written as (e.g., Eq. (37) of [17])

$$a_{\mathcal{H}}^{(k)} \equiv \frac{1}{8\pi} \oint_{\mathcal{H}} \left(K_{ij} - g_{ij} K\right) \xi^j_{(k)} d^2 S^i, \tag{6.16}$$

where $\mathcal{H}$ is either $\mathcal{H}_A$ or $\mathcal{H}_B$, and $\xi^i_{(k)}$ is a Killing vector on $\mathcal{H}$ that defines rotations about the k axis. In this paper, I consider only non-rotating binaries, in which Ω_r is selected so that $a_{\mathcal{H}}^{(k)}$ is very close to zero.

The inner condition on α is a gauge choice [16]; i.e., it does not affect the physical content of the initial data. The particular choices used in this paper are discussed in Sec. 6.3.

6.3 Nonspinning, non-eccentric binary-black-hole initial data

6.3.1 Conformally flat data

Initial data for binary-black-holes are typically assumed to be conformally flat:

$$\tilde{g}_{ij} = \delta_{ij}. \tag{6.17}$$

---

[1] Here "outward-pointing" points away from the black hole, toward infinity.

In Sec. 6.4, the conformally-flat data set CF is the same as that of [19], except that the black holes begin at a larger coordinate separation (in this paper, the holes begin about 15 orbits from merger). Specifically, in set CF,

$$K = 0, \tag{6.18}$$

$$\partial_r(\alpha\psi) = 0 \text{ on } \mathcal{S}. \tag{6.19}$$

6.3.2 Non conformally flat data

To reduce the amount of junk radiation, it is necessary to use a non-flat conformal metric. In this section, I build up a suitable conformal metric for two non-spinning black holes in an initially circular orbit.

6.3.2.1 Schwarzschild with maximal slicing

The Schwarzschild metric can be split into maximal slices (i.e., slices with $K = 0$.) With maximal slicing, the Schwarzschild spacetime is (e.g., Eq. (52) of [16]):

$$\begin{aligned} g^o_{ij}dx^i dx^j &= \alpha^{-2}dR^2 + R^2 d\Omega^2, \\ \alpha &= \sqrt{1 - \frac{2M}{R} + \frac{C^2}{R^4}}, \\ \beta^i &= \frac{C}{R^2}\alpha e^i_R, \end{aligned} \tag{6.20}$$

where R is the Schwarzschild areal radial coordinate and e^i_R is a unit vector normal to constant-R surfaces. The choice of C specifies which maximal slicing is used (and thence the coordinate radius of the horizon). To facilitate comparison with [19], in this paper I choose $C = 1.737M$, which implies the horizon radius is at $r_{exc} = 0.8595M$.

6.3.2.2 Metric of a boosted Schwarzschild hole

To construct the metric of a boosted, Schwarzschild hole, I begin with the Schwarzschild metric $g^o_{\mu\nu}$ [Eq. (6.20)]. Then, I apply the following two coordinate transformations:

1. First, I apply a radial coordinate transformation to make the spatial metric conformally flat. *Any* spherically-symmetric metric can be made conformally flat by i) writing it as

   $$g_{ij}dx^i dx^j = f(R)dR^2 + R^2 d\Omega^2, \tag{6.21}$$

   where R is an areal radial coordinate, and then ii) making a radial coordinate transformation

$r = r(R)$ so that the metric is conformally flat:

$$f(R)dR^2 + R^2 d\Omega^2 = \psi^4 \left(dr^2 + r^2 d\Omega^2\right) \tag{6.22}$$

$$\Rightarrow \psi^2 = R/r \text{ and } \frac{dr}{dR} = \frac{r}{R}\sqrt{f(R)}. \tag{6.23}$$

For a given $f(R)$, determining $r(R)$ amounts to solving a first-order ordinary differential equation. For the choice $f(R) = \alpha^{-2}$ [cf. Eq. (6.20)], the analytic solution to the ODE is unknown, so the ODE (6.23) is solved numerically.

2. Once the spatial metric is conformally flat, I give the Schwarzschild hole a velocity v in the y direction by performing a Lorentz boost. The resulting spacetime metric is $g_{\mu\nu}^{\text{Boost}}(v)$.

6.3.2.3 Superposing two boosted, non-spinning holes

Suppose two nonspinning black holes, "A" and "B," are initially separated by coordinate distance d_o. Suppose they are in a circular orbit with speed $v = \Omega d_o/2$.

I seek free data that accurately describes the boosted black holes. The simplest choice is to merely superpose two boosted-Schwarzschild black-holes:

$$\tilde{g}_{ij} = \tilde{g}_{ij}^{\text{NSBS}} \equiv \delta_{ij} + \left(g_{ij}^{A} - \delta_{ij}\right) + \left(g_{ij}^{B} - \delta_{ij}\right), \tag{6.24}$$

$$K = K^{\text{NSBS}} \equiv K^{A} + K^{B}. \tag{6.25}$$

Here "NSBS" stands for "naive superposed, boosted Schwarzschild." For hole A, g_{ij}^{A} and K^A are obtained by translating $g_{\mu\nu}^{\text{Boost}}(v)$ so that the hole is centered about $(x, y, z) = (d_o/2, 0, 0)$. Likewise, for hole B, g_{ij}^{B} and K^B are obtained by translating $g_{\mu\nu}^{\text{Boost}}(-v)$ so that the hole is centered about $(x, y, z) = (-d_o/2, 0, 0)$. Note that as $v \to 0$, $\tilde{g}_{ij}^{\text{NSBS}} \to \psi_o^4 \delta_{ij}$ and $K^{\text{NSBS}} \to 0$; after absorbing ψ_o into the conformal factor ψ, the $v = 0$ superposed-boosted-Schwarzschild data in fact reduces to the well-examined (conformally flat) quasiequilibrium data by Cook and Pfeiffer [16].

I used the Caltech-Cornell pseudospectral code [18] to solve the XCTS equations with the free data and boundary conditions described previously. When the conformal metric is $\tilde{g}_{ij}^{\text{NSBS}}$, I find that the elliptic solver does not converge [Fig. 6.1].

The source of the difficulty can be seen by inserting the outer boundary conditions (6.11), (6.12), and (6.13) into the Hamiltonian constraint [the first of Eq. (6.1)], which gives an equation of the form

$$-\tilde{\nabla}^2\psi - (\tilde{\mathbb{L}}\mathbf{\Omega} \times \mathbf{r})^{ij}(\tilde{\mathbb{L}}\mathbf{\Omega} \times \mathbf{r})_{ij} + \cdots = 0. \tag{6.26}$$

The source term shown here vanishes when the metric is conformally flat, because $(\mathbf{\Omega} \times \mathbf{r})^i$ is a

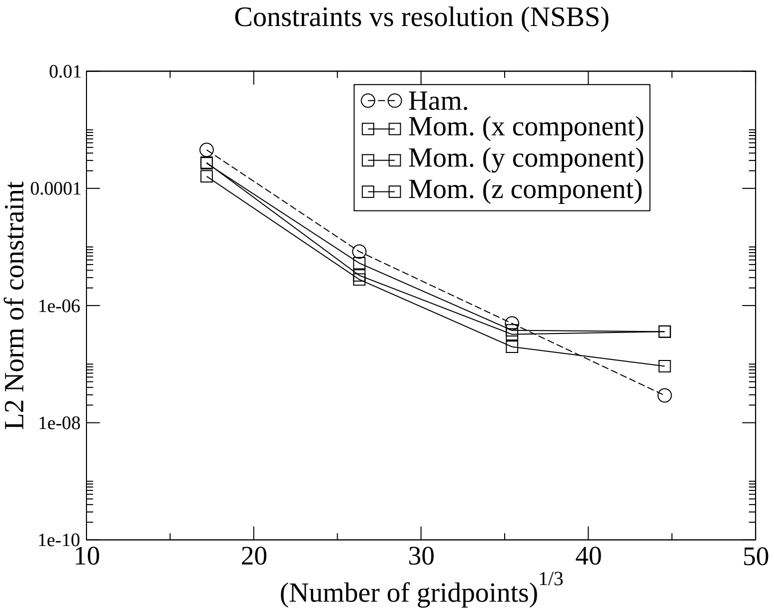

Figure 6.1: When the conformal metric is $\tilde{g}_{ij}^{\rm NSBS}$, the constraints do not decrease exponentially with increasing radial resolution.

conformal Killing vector of flat space. But when the conformal metric is the naive superposition (6.24), the term $(\tilde{\mathbb{L}}\mathbf{\Omega}\times\mathbf{r})_{xy}$ contains a spherically-symmetric part that decays only as $O(1/r)$ [Fig. 6.2]. It follows that $\psi\rightarrow \mathrm{const}\times\log r$ as $r\rightarrow\infty$, but this is incompatible with the requirement that $\psi\rightarrow 1$ as $r\rightarrow\infty$.

6.3.2.4 Scaling the non-flat terms by Gaussians

The inconsistency described in the previous subsection can be avoided by requiring that the non-flat terms fall off sufficiently quickly far from the holes. This can be accomplished by scaling the non-flat terms by Gaussians:

$$\tilde{g}_{ij} = \tilde{g}_{ij}^{\rm SBS} \equiv \delta_{ij} + e^{-r_A^2/w^2}\left(g_{ij}^A - \delta_{ij}\right) + e^{-r_B^2/w^2}\left(g_{ij}^B - \delta_{ij}\right), \tag{6.27}$$

$$K = K^{\rm SBS} \equiv e^{-r_A^2/w^2} K^A + e^{-r_B^2/w^2} K^B. \tag{6.28}$$

Here "SBS" stands for "superposed, boosted Schwarzschild," and r_A and r_B are the coordinate distances from the centers of holes A and B, respectively. The width w can be adjusted to minimize the junk radiation. Further investigation is needed to find an optimal choice for w. The Gaussians used here may seem similar to the attenuation functions of [28]; however, the attenuation functions here approach zero at large radii, whereas those of [28] approach unity. In Sec. 6.4, data set SBS uses $w = 20r_{exc}$. With this choice, the elliptic solver converges, and the constraints decay exponentially with resolution, as expected [Fig. 6.3].

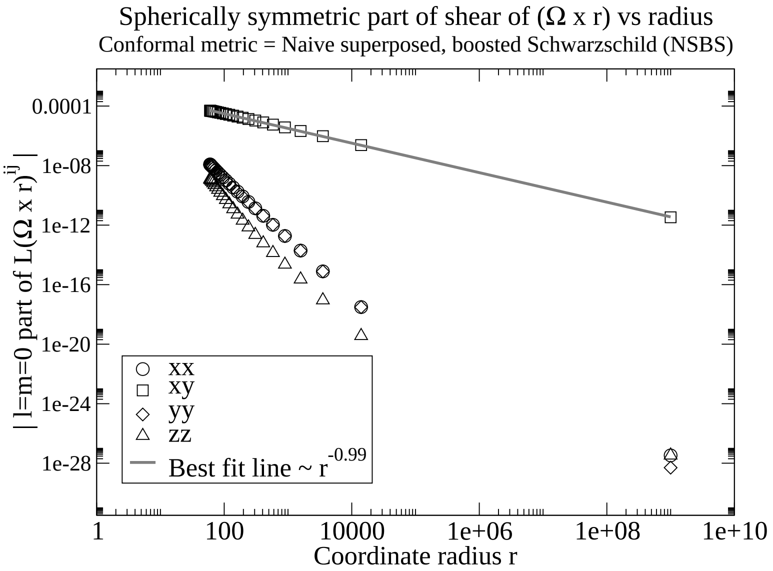

Figure 6.2: The xy component of $(\tilde{\mathbb{L}}\mathbf{\Omega} \times \mathbf{r})^{ij}$ includes a spherically-symmetric term that decays only as $1/r$ when the conformal metric is g_{ij}^{NSBS}; this term causes the conformal factor to diverge logarithmically as $r \to \infty$. The other nonzero components decay as $1/r^2$ or faster.

Finally, as noted in Sec. 6.2.2.3, the inner boundary condition on the lapse α is a gauge choice; in set SBS, the condition is

$$\alpha\psi = 1 + e^{-r_A^2/w^2}\left(\alpha^A - 1\right) + e^{-r_B^2/w^2}\left(\alpha^B - 1\right) \text{ on } \mathcal{S}. \tag{6.29}$$

Here α^A is obtained by translating $g_{\mu\nu}^{\mathrm{Boost}}(v)$ so that hole A is centered about $(x,y,z) = (d_o/2,0,0)$; likewise, α^B is obtained by translating $g_{\mu\nu}^{\mathrm{Boost}}(-v)$ so that hole B is centered about $(x,y,z) = (-d_o/2,0,0)$.

6.4 Comparing the junk radiation of conformally flat and superposed-boosted-Schwarzschild initial data

6.4.1 The conformally flat (CF) and superposed-boosted-Schwarzschild (SBS) initial data sets

To compare the size of the junk radiation, I have constructed and evolved two initial data sets: a conformally flat set (CF), and a superposed-boosted-Schwarzschild set (SBS). The method for constructing the initial data is described in Sec. 6.3.

Table 6.1 compares some physical properties of the two data sets. The irreducible mass M_{irr} is

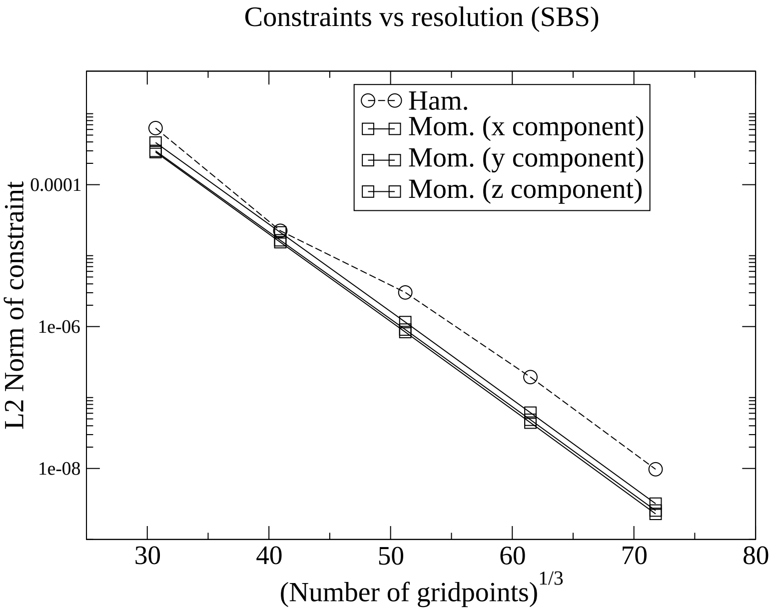

Figure 6.3: Constraints as a function of resolution when the conformal metric is g_{ij}^{SBS}, which is non-flat near the black holes but flat far away. The constraints decrease exponentially with increasing resolution, as expected.

defined in terms of the apparent-horizon area A_{AH} by

$$M_{\mathrm{irr}} = \sqrt{\frac{A_{\mathrm{AH}}}{16\pi}}. \tag{6.30}$$

The ADM Mass is a measure of the total energy in the system. It is defined by the following surface integral at ∞:

$$M_{\mathrm{ADM}} = \frac{1}{16\pi}\int_{\infty} \left(\partial_j g_{ij} - \partial_i g_{jj}\right) d^2S^i. \tag{6.31}$$

In practice, this integral is evaluated on the outer boundary of the initial-data grid (i.e., on $\mathcal{B}$, which is a sphere whose radius is approximately $10^9 M_{\mathrm{irr}}$).

The initial coordinate separation is d_o. The initial "proper separation" s_o is defined in terms of the following line integral along the x-axis of the comoving frame:

$$s_o = \int ds = \int_{-d/2+r_{exc}}^{d/2-r_{exc}} dx\sqrt{g_{xx}} \tag{6.32}$$

Here the limits of integration are the coordinate locations where the holes' apparent horizons intersect the x axis. The excision radius (given by $r_{exc} = 0.8595M$ at $t = 0$) is the coordinate radius of the apparent horizon. Note that the "proper separation" is coordinate-dependent (since the integral is taken along the x-axis, rather than along a geodesic of extremal length) and slicing-dependent (since

Quantity	CF	SBS
$M_{\rm irr}$	1.039	1.027
$M_{\rm ADM}$	2.062	2.039
$d_o/M_{\rm ADM}$	14.55	14.71
$s_o/M_{\rm ADM}$	17.51	17.65
$M_{\rm ADM}\Omega$	0.0165787	0.0162814
v_r	-4.3×10^{-4}	-3.5×10^{-4}
$\lvert a^x/M_{\rm irr}^2\rvert$ and $\lvert a^y/M_{\rm irr}^2\rvert$	$< 3\times10^{-13}$	$< 4\times10^{-10}$
$a^z/M_{\rm irr}^2$	-1.1×10^{-4}	-5.3×10^{-5}

Table 6.1: A comparison of the two initial data sets presented in this paper. Set CF is conformally flat, and set SBS uses a conformal metric that is a superposition of two boosted Schwarzschild black holes. The initial data sets describe physically comparable situations: the masses, separations, and frequencies agree to within about 1%. The radial velocities are comparable [and are chosen so that the eccentricity is small (Fig. 6.4)], and the spins of the holes are close to zero in both cases.

the distance is measured within the spatial slice).

The spins of the holes are computed [29] using the quasilocal Brown-York spin [[25]; Eq. (6.16)]. The spin on the holes is small in both the CF and SBS data sets.

6.4.1.1 Evolutions and reducing eccentricity

The CF and SBS data sets were evolved using the Caltech-Cornell spectral evolution code. The evolution grid's outer boundary is at approximately $1000M_{\rm irr}$. The excision boundaries are slightly inside the apparent horizons; this is accomplished by extrapolating the initial data from $\mathcal{S}$ to points slightly inside S. (For set CF, the evolution-grid excision spheres are at radius $r_{ev} = 0.97r_{exc}$; to accommodate nonspherical horizons, the evolution-grid excision spheres are at $r_{ev} = 0.93r_{exc}$ for set SBS.) Aside from differences in extrapolation, sets CF and SBS were evolved using identical computational domains and at identical resolutions[2].

The holes initially move at a coordinate angular velocity Ω and a coordinate radial velocity v_r; both are chosen to reduce the eccentricity of the orbit. The set CF has much less eccentricity than does the equivalent conformally flat, quasicircular initial data; it is comparable (aside from the greater initial separation of the holes) to the non-eccentric data sets in [19].

To make the SBS data set non-eccentric, I initially guess that Ω and v_r have the same coordinate values as in the non-eccentric, conformally flat case. Then, I tune them using the iterative scheme described in Sec. 4 of [19]. Each iteration would completely remove the eccentricity if the binary were Newtonian; in the relativistic case, successive iterations converge to non-eccentric orbits. Figure 6.4 shows the proper separation vs. time of the CF data and of the SBS data sets. "Reduction iter #2" is the SBS data set used in the remainder of this paper.

---

[2] The initial data were evolved on grids of several different resolutions. The waveforms appear to agree to "good" accuracy, and the constraints appear to converge exponentially. Rigorous convergence tests are a subject of future research.

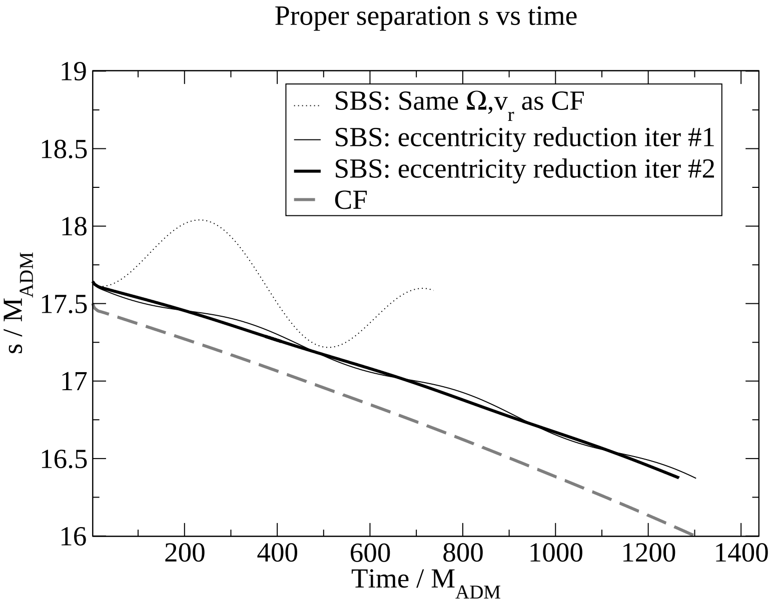

Figure 6.4: Reducing the eccentricity in the SBS initial data set. The proper separation vs. time is shown for the conformally flat (CF) data set (grey line). The corresponding SBS data set with the same choices for Ω and v_r is very eccentric (dotted line), but two iterations of the algorithm described in Sec. 4 of [19] greatly reduce the orbital eccentricity (dashed and solid lines).

6.4.1.2 Junk radiation comparison

The gravitational waves are extracted from the CF and SBS evolutions at the same coordinate radius $r_{extr} \approx 116 r_{exc}$. Specifically, the simulation computes the Newman-Penrose scalar Ψ_4, which at large radii is related to the outgoing +-polarized and ×-polarized gravitational-wave amplitudes by

$$\Psi_4 = \frac{d^2}{dt^2}h_+ - i\frac{d^2}{dt^2}h_\times . \tag{6.33}$$

The scalar Ψ_4 is evaluated on a sphere of radius r_{extr} and then expanded in spin-weighted-spherical-harmonic modes. (For further details on the wave-extraction method, see Sec. 5.5.3 in this thesis.)

At early times, the waveform consists of spurious gravitational waves; they are recognizable as such by their frequencies, which are much higher than the dominant frequencies $f \sim \Omega/\pi$ of the physical, quadrupolar gravitational waves. Figure 6.5 plots the dominant, quadrupolar components of the junk waves; they have a frequency $f \sim (15 M_{\rm ADM})^{-1}$, which is significantly higher than the physical frequency $f \sim \Omega/\pi \sim (200 M_{\rm ADM})^{-1}$. The SBS junk waves are smaller in amplitude by about a factor of 2 when compared with the CF waves.

Figure 6.6 compares all of the spherical harmonic modes from $\ell = 2$ through $\ell = 8$. The amplitudes of the higher modes are reduced by a significantly larger amount than were the $l = 2$ modes' amplitudes.

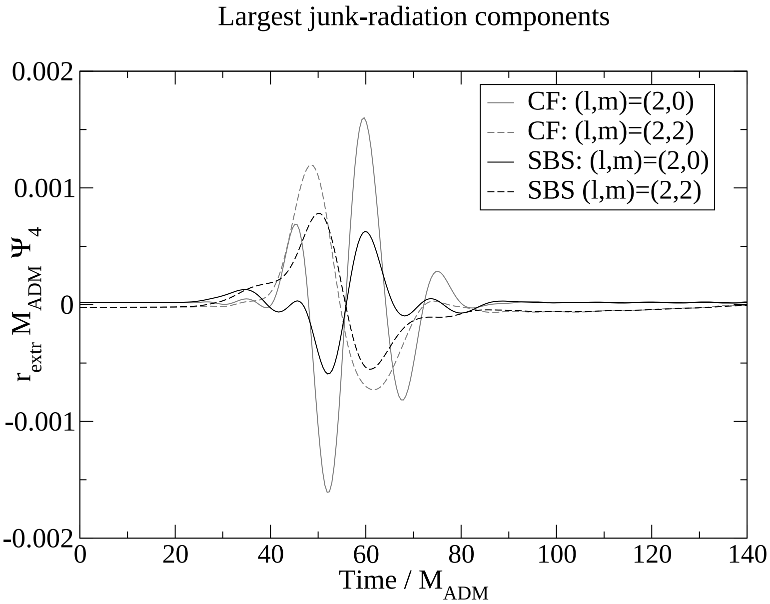

Figure 6.5: A comparison of the dominant (quadrupolar) modes of the junk radiation for conformally flat (CF) and superposed-boosted-Schwarzschild (SBS) initial data. The real parts of the $(\ell, m) = (2, 0)$ and $(\ell, m) = (2, 2)$ parts of Ψ_4 are shown.

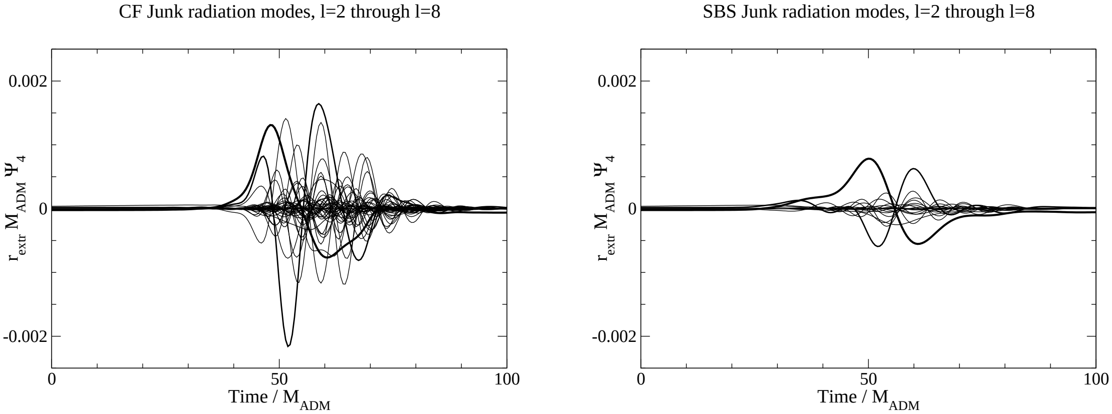

Figure 6.6: A comparison of the junk gravitational waves extracted at coordinate radius $r_{extr} = 100$ for the conformally flat (CF) and superposed-boosted-Schwarzschild (SBS) initial data. The $\ell = 2$ through $\ell = 8$ spherical-harmonic modes are shown, with the Re$(2, 0)$ modes shown as a very thick line, Re$(\ell = 2, m = 2)$ shown as a medium-thick line, and other modes shown as thin lines.

6.5 Conclusion

The junk radiation in binary-black-hole simulations can be significantly reduced by using initial data that is not conformally flat. For the case of two non-spinning black holes initially 15 orbits from merger, the amplitude of the junk gravitational waves decreases by a factor of order 2. As of this writing, sets CF and SBS have only been evolved at a "typical" resolution; future work will include convergence tests at a variety of evolutions. Also, future investigations will seek to generalize this work to black hole binaries in which the holes have spin.

6.6 Bibliography

[1] B. C. Barish and R. Weiss, Phys. Today **52 (Oct)**, 44 (1999).

[2] C. Cutler and K. S. Thorne, in *Proceedings of the GR16 Conference on General Relativity and Gravitation* (World Scientific, Hackensack, New Jersey, 2002).

[3] F. Pretorius, Phys. Rev. Lett. **95**, 121101 (2005), `gr-qc/0507014`.

[4] J. G. Baker, J. Centrella, D.-I. Choi, M. Koppitz, and J. van Meter, Phys. Rev. Lett. **96**, 111102 (2006).

[5] M. Campanelli, C. O. Lousto, P. Marronetti, and Y. Zlochower, Phys. Rev. Lett. **96**, 111101 (2006).

[6] M. A. Scheel, H. P. Pfeiffer, L. Lindblom, L. E. Kidder, O. Rinne, and S. A. Teukolsky, Phys. Rev. D **74**, 104006 (2006), `gr-qc/0607056`.

[7] B. Brügmann, J. A. Gonzalez, M. Hannam, S. Husa, U. Sperhake, and W. Tichy (2006), `gr-qc/0610128`.

[8] G. B. Cook, Living Rev. Rel. **5**, 1 (2000).

[9] H. P. Pfeiffer, J. Hyperbolic Differential Equations **2**, 497 (2005), `gr-qc/0412002`.

[10] J. W. York, Jr., in *Essays in general relativity*, F. Tipler, Ed., (Academic, New York, 1981), Ch. 4, p. 39.

[11] A. Garat and R. H. Price, Phys. Rev. D **61**, 124011 (2000).

[12] M. Hannam, S. Husa, B. Bruegmann, J. A. Gonzalez, and U. Sperhake, Special "New Frontiers in Numerical Relativity" issue of Class. Quantum Grav. (submitted) (2006), URL `http://arxiv.org/abs/gr-qc/0612001`.

[13] B. J. Kelly, W. Tichy, M. Campanelli, and B. F. Whiting, Phys. Rev. D (submitted) (2007), URL `http://arxiv.org/abs/0704.0628v1`.

[14] R. A. Matzner, M. F. Huq, and D. Shoemaker, Phys. Rev. D **59**, 024015 (1999).

[15] G. B. Cook, Phys. Rev. D **65**, 084003 (2002).

[16] G. B. Cook and H. P. Pfeiffer, Phys. Rev. D **70**, 104016 (2004).

[17] M. Caudill, G. B. Cook, J. D. Grigsby, and H. P. Pfeiffer, Phys. Rev. D **74**, 064011 (2006), `gr-qc/0605053`.

[18] H. P. Pfeiffer, L. E. Kidder, M. A. Scheel, and S. A. Teukolsky, Comput. Phys. Commun. **152**, 253 (2003).

[19] H. P. Pfeiffer, D. A. Brown, L. E. Kidder, L. Lindblom, G. Lovelace, and M. A. Scheel (2007), special issue of Class. Quantum Grav. (in press), Chapter 5 of this thesis, URL `http://arxiv.org/abs/gr-qc/0702106`.

[20] L. Lindblom, M. A. Scheel, L. E. Kidder, R. Owen, and O. Rinne, Class. Quantum Grav. **23**, S447 (2006).

[21] J. W. York, Jr., Phys. Rev. Lett. **82**, 1350 (1999).

[22] H. P. Pfeiffer and J. W. York, Jr., Phys. Rev. D **67**, 044022 (2003).

[23] E. Gourgoulhon, P. Grandclément, and S. Bonazzola, Phys. Rev. D **65**, 044020 (2002).

[24] P. Grandclément, E. Gourgoulhon, and S. Bonazzola, Phys. Rev. D **65**, 044021 (2002).

[25] J. D. Brown and J. W. York, Jr., Phys. Rev. D **47**, 1407 (1993).

[26] A. Ashtekar and B. Krishnan, Phys. Rev. D **68**, 104030 (2003).

[27] A. Ashtekar and B. Krishnan, Living Rev. Relativity **7** (2004), (online article cited 19 Apr 2005), URL http://www.livingreviews.org/lrr-2004-10.

[28] P. Marronetti, M. Huq, P. Laguna, L. Lehner, R. A. Matzner, and D. Shoemaker, Phys. Rev. D **62**, 024017 (2000).

[29] R. Owen et al., (in preparation).